



THE HONG KONG
POLYTECHNIC UNIVERSITY

香港理工大學

Pao Yue-kong Library

包玉剛圖書館

Copyright Undertaking

This thesis is protected by copyright, with all rights reserved.

By reading and using the thesis, the reader understands and agrees to the following terms:

1. The reader will abide by the rules and legal ordinances governing copyright regarding the use of the thesis.
2. The reader will use the thesis for the purpose of research or private study only and not for distribution or further reproduction or any other purpose.
3. The reader agrees to indemnify and hold the University harmless from and against any loss, damage, cost, liability or expenses arising from copyright infringement or unauthorized usage.

IMPORTANT

If you have reasons to believe that any materials in this thesis are deemed not suitable to be distributed in this form, or a copyright owner having difficulty with the material being included in our database, please contact lbsys@polyu.edu.hk providing details. The Library will look into your claim and consider taking remedial action upon receipt of the written requests.

**STUDY OF HIGH-FREQUENCY ULTRASOUND
TRANSDUCERS FOR ADVANCED BIOMEDICAL
IMAGING**

WONG CHI MAN

PhD

The Hong Kong Polytechnic University

2022

THE HONG KONG POLYTECHNIC UNIVERSITY
DEPARTMENT OF APPLIED PHYSICS

**STUDY OF HIGH-FREQUENCY ULTRASOUND
TRANSDUCERS FOR ADVANCED BIOMEDICAL
IMAGING**

WONG CHI MAN

A thesis submitted in partial fulfillment of the requirements for
the degree of Doctor of Philosophy

January 2021

CERTIFICATE OF ORIGINALITY

I hereby declare that this thesis is my own work and that, to the best of my knowledge and belief, it reproduces no material previously published or written, nor material that has been accepted for the award of any other degree or diploma, except where due acknowledgment has been made in the text.

_____ (Signed)

Wong Chi Man _____ (Name of student)

ABSTRACT

Ultrasound imaging is one of the main medical diagnostic tools for clinical use due to its non-radioactive and harmless nature. In recent decades, medical ultrasound technologies are being widely developed for not only improving the image quality in conventional clinical use but also applying on new aspects such as clinical therapeutic and preclinical pathology or physiology research applications. New designs of transducer are desired to accomplish those application, and the performance improvement of those assistance material is also required.

In this study, analysis is conducted on the synergistic effect of preclinical biomedical imaging through the usage of the high resolution clinical imaging technique. Therefore, high frequency ultrasound transducers accompanied by high performance, such as high spatial resolution and sensitivity, is investigated due to its finer detail with higher spatial frequency in the imaging targets, such as small mammalian and human tissues. Meanwhile, development of fabrication process and fabrication of advanced acoustic materials aiming at improving transducer's performance are also carried out.

Matching layer is a critical component that determines the performance of piezoelectric-based ultrasound transducers. For most piezoelectric materials, their acoustic impedances are significantly higher than human tissues and organs (around 1.6 MRayl), so a tunable matching layer with a high acoustic impedance is required for optimizing the acoustic wave transmission. In this thesis work, a high compression fabrication method is invented, with which the acoustic impedance of alumina-epoxy composite matching layer can be tuned from 6.50 to 9.47 MRayl by controlling the applied compression pressure and ratio of alumina to epoxy. This enhancement of acoustic impedance is attributed to the increased acoustic longitudinal velocity when alumina content reaches a critical value

causing coalitions and domination of the acoustic wave propagation in the matching layer. Furthermore, the attenuation of this newly developed matching layer is only -10 dB/mm at 40 MHz. The very high acoustic impedance value and very low attenuation make this matching material superior than all reported matching materials, and therefore, can enhance the performance of the ultrasound transducers, especially for medical imaging applications at high to ultra-high frequency regime.

In vivo ultrasound imaging with phase array transducers is of great importance for both clinical application and biomedical research. In this work, relaxor ferroelectric PMN-0.28PT single crystal with very high piezoelectric constant ($d_{33} \geq 2000$ pC/N) and a higher electromechanical coupling factor ($k_{33} \sim 0.92$), was used to develop high-frequency phase array transducers. A 128-element 20-MHz phased-array ultrasound transducer was successfully fabricated with optimized performance of an average $\sim 84\%$ bandwidth at -6 dB and insertion loss of -43 dB. The axial and lateral resolutions of this transducer were determined to be 40.5 μm and 121.5 μm , respectively. With this transducer and Verasonics image platform, in-situ images of a fisheye and in-vivo laboratory mice's cardiac images were acquired, demonstrating successful application of our developed high-frequency phase array transducer for biomedical research of small animals.

Cranial ultrasound is limited at infant and temple brain imaging because the rest parts of skull bone are too thick for penetrating. A new 2D annular array transducer idea based on the structure of Fresnel annular array is raised, designed and developed, aiming at transcranial brain imaging and stimulating through the pterion. The simulation result shows a pair of separated sectors in a modified structure produces an on-axis focal point at 34 mm with maximum 20 kPa pressure. The focal spot size is 12 mm length along axial direction and 0.045 mm width along lateral direction. The developed PZT 2D annular

array transducer contents total 48 elements distributed in 8 sectors is also measured. The represented elements along the sector show a 16.10 MHz average center frequency and a -6 dB bandwidth around 80%. By further using an electrical signal control, a 3D conical shape image may be obtained. More work needs to be done to include more elements and develop new imaging method.

LIST OF PUBLICATIONS

JOURNAL ARTICLES

- [1] M. Y. Tse, X. Wei, C.-M. Wong, L.-B. Huang, K. H. Lam, J. Dai, and J. Hao, “Enhanced Dielectric Properties of Colossal Permittivity Co-Doped TiO₂/Polymer Composite Films,” *RSC Adv*, vol. 8, no. 57, pp. 32972–32978, 2018.
- [2] Y. Chen, X. Bao, C.-M. Wong, J. Cheng, H. Wu, H. Song, X. Ji, and S. Wu, “PZT Ceramics Fabricated Based on Stereolithography for an Ultrasound Transducer Array Application,” *Ceramics International*, vol. 44, no. 18, pp. 22725–22730, Dec. 2018.
- [3] H. M. Yau, X. Chen, C. M. Wong, D. Chen, J. D. M. Characterization, 2021, “Orientation Control of Phase Transition and Ferroelectricity in Al-Doped HfO₂ Thin Films,” *Materials Characterization*, pp. 111–114, 2021.
- [4] N. Lyapunov, C. H. Suen, C. M. Wong, X. Tang, Z. L. Ho, K. Zhou, X. X. Chen, H. M. Liu, X. Zhou, and J. Y. Dai, “Ultralow Switching Voltage and Power Consumption of GeS₂ Thin Film Resistive Switching Memory,” *Journal of Advanced Dielectrics*, Feb. 2021.
- [5] C. M. Wong, S. F. Chan, W.C. Wu, C.H. Suen, H. M. Yau, J.Y. Dai, “Tunable High Acoustic Impedance Alumina Epoxy Composite Matching for High Frequency Ultrasound Transducer,” *Ultrasonics*, vol. 116, Sep 2021
- [6] C. M. Wong, S. F. Chan, R. Liu, W.C. Wu, Z. Liang, H. M. Yau, D.Y. Wang, S. Li, K. H. Lam, W.B. Qiu, H.S. Luo and J.Y. Dai, “20-MHz Phased-array Ultrasound Transducer for In-vivo Ultrasound Imaging of Small Animals,” (In process. Submitted to *Ultrasonics*)

PATENT

- [1] Yan Chen, Chi-Man Wong, Yongxin Lyu, Siu-Fan Chan, Cheuk-Ho Chan, Jiyan Dai, “A Device for New 3-Dimensional Ultrasound Imaging Method”, China CN 109381218 A, 2019
- [2] Jiyan Dai, Chi-Man Wong, Hei-Man Yau, Siu-Fan Chan, “Fiber Bragg grating (FBG) and intravascular ultrasound transducer (IVUS) hybrid catheterization diagnosing fractional flow reserve technique” China (In process)
- [3] Jiyan Dai, W.C. Wu, Chi-Man Wong, “A 2-Dimensional Ultrasound Array Transducer and its Fabrication Method” China (In process)

ACKNOWLEDGEMENTS

I would like to thank Prof. Jiyan Dai for his guidance and support. I was lucky to have him as my supervisor because I have learned not only how to conduct research, but also more importantly how we can contribute to the world with what we can do for the better future.

I am very grateful to all our current and former group members Ms. Siu-Fan Chan, Ms Hei-Man Yau, Mr. Chun-Hung Suen and Mr Weichang Wu for their support and sharing the wonderful moments for the past three years. Also, special thanks for the senior artisan Kai-Hong Ho who made the fabulous mechanical devices, assemblies and professional advices. I wish to thank Dr. Hardy Lui of the Materials Research Centre, and Dr. Terence Wong and Ms. Joyce Lau of the University Research Facility in Materials Characterization and Device Fabrication for their assistance in equipment operation.

I also would like to thank my dearest mother and father, for their love and support for all years. Finally, a most special thanks for my lovely girlfriend Ms Hei Man Yau who is a best listener that listens and joins my extremely useless and boring philosophical discussion. In all, I would like to thank my thesis's financial support: Hong Kong Innovation and Technology Fund (Project No. ITS/044/17, ITF/082/18), Research Impact Fund (R5029-19), PolyU internal grant (UAEZ, G-YBPN, G-YBLM), National Key Research and Development Program of China (2018YFC01163), National Natural Science Foundation Grants of China (11874382, 81927808), Shenzhen Research Grant (GJHZ20180420180920529, JCYJ20170817171836611, and ZDSYS201802061806314), Shenzhen Double Chain Project [2018]256, Youth Innovation Promotion Association CAS, CAS research projects (QYZDB-SSW-JSC018) and Guangdong Special Support Program. Thanks also give Department of Applied

Physics of the Hong Kong Polytechnic University

TABLE OF CONTENTS

CERTIFICATE OF ORIGINALITY	II
ABSTRACT	III
LIST OF PUBLICATIONS.....	VI
ACKNOWLEDGEMENTS	VII
TABLE OF CONTENTS.....	IX
TABLE OF FIGURE	XII
LIST OF TABLES.....	XVIII
CHAPTER 1 LITERATURE REVIEW AND MOTIVATION OF THESIS WORK	1
1.1 INTRODUCTION ABOUT MEDICAL ULTRASOUND TRANSDUCER.....	1
1.2 DEVELOPMENT OF ULTRASOUND TRANSDUCERS.....	5
1.3 MOTIVATION OF THIS THESIS WORK.....	9
1.4 SCOPE OF THE THESIS.....	10
CHAPTER 2 INTRODUCTION TO ULTRASOUND TRANSDUCER	13
2.1 ULTRASOUND IMAGING SYSTEM.....	13
2.1.1 MECHANISM OF ULTRASOUND TRANSDUCER	14
2.1.1.1 Capacitive based.....	14
2.1.1.2 Piezoelectric based	15
2.2 CHARACTERISTIC OF PIEZOELECTRIC ULTRASOUND TRANSDUCER.....	16
2.2.1 STRUCTURE OF PIEZOELECTRIC ULTRASOUND TRANSDUCER	16
2.2.1.1 Piezoelectric properties of active layer.....	18
Piezoelectric crystal structure	18
Piezoelectric constant	22
Electromechanical coupling coefficient.....	23
2.2.1.2 Matching layer.....	25
2.2.1.3 Backing layer	29
2.2.2 SENSITIVITY OF PIEZOELECTRIC ULTRASOUND TRANSDUCER	31
2.2.3 RESOLUTION OF PIEZOELECTRIC ULTRASOUND TRANSDUCER.....	32
2.2.3.1 Axial resolution	32
2.2.3.2 Lateral resolution.....	34

CHAPTER 3 TUNABLE HIGH ACOUSTIC IMPEDANCE ALUMINA-EPOXY COMPOSITE MATCHING FOR HIGH FREQUENCY ULTRASOUND TRANSDUCER	37
3.1 INTRODUCTION	37
3.2 FABRICATION AND CHARACTERIZATION	41
3.2.1 <i>MATCHING LAYER FABRICATION</i>	41
3.2.2 <i>ACOUSTIC IMPEDANCE CHARACTERIZATION</i>	42
3.2.2.1 <i>Acoustic Velocity</i>	43
3.2.2.2 <i>Density</i>	45
3.2.3 <i>ACOUSTIC ATTENUATION CHARACTERIZATION</i>	45
3.2.4 <i>ACOUSTIC RESPONSE OF TRANSDUCERS</i>	46
3.2.4.1 <i>Pulse echo response and frequency spectrum</i>	46
3.2.4.2 <i>Insertion loss</i>	48
3.3 RESULTS	48
3.3.1 <i>APPLIED PRESSURE VARIANT</i>	48
3.3.2 <i>POWDER CONCENTRATION VARIANT</i>	51
3.3.3 <i>MICROSCOPIC STRUCTURE</i>	53
3.4 DISCUSSIONS	58
3.4.1 <i>PRESSURE VARIANT</i>	58
3.4.2 <i>POWDER CONCENTRATION VARIANT</i>	60
3.4.3 <i>MICROSCOPIC STRUCTURE</i>	62
3.5 SUMMARY	63
CHAPTER 4 STUDY OF ADVANCED FABRICATION METHOD	65
4.1 ARRAY FABRICATION METHOD INVESTIGATION	65
4.1.1 <i>LASER CUTTING</i>	66
4.1.2 <i>MECHANICAL DICING</i>	74
4.2 SUMMARY	80
CHAPTER 5 20-MHZ PHASED-ARRAY ULTRASOUND TRANSDUCER FOR IN-VIVO ULTRASOUND IMAGING OF SMALL ANIMALS	82
5.1 INTRODUCTION	82
5.2 EXPERIMENTAL DETAILS OR EXPERIMENT	85
5.2.1 <i>PIEZOELECTRIC LAYER CHARACTERIZATIONS</i>	85
5.2.2 <i>TRANSDUCER DESIGN</i>	87
5.2.3 <i>MODELLING OF ULTRASOUND TRANSDUCER</i>	92

5.2.4	<i>FABRICATION PROCESS</i>	94
5.2.5	<i>CHARACTERIZATION OF ACOUSTIC AND ELECTRICAL RESPONSE OF THE TRANSDUCER</i>	98
5.2.6	<i>BIOMEDICAL IMAGING DEMONSTRATION</i>	99
5.3	RESULTS.....	102
5.3.1	<i>SIMULATION RESULTS</i>	102
5.3.2	<i>ACOUSTIC AND ELECTRICAL RESPONSE</i>	107
5.3.3	<i>MEDICAL IMAGING MEASUREMENT</i>	114
	5.3.3.1 <i>Wire phantom measurement</i>	114
	5.3.3.2 <i>Biomedical imaging acquisition</i>	116
5.4	DISCUSSION	119
5.5	SUMMARY	125
CHAPTER 6 DESIGN AND DEVELOPING AN ULTRASOUND TRANSDUCER FOR TRANSCRANIAL DIAGNOSIS AND THERAPY		127
6.1	BACKGROUND.....	127
6.2	EXPERIMENTAL DETAILS	132
	6.2.1 <i>DESIGN OF THE 2D ANNULAR ARRAY TRANSDUCER</i>	132
	6.2.2 <i>MODELLING OF 2D ANNULAR ARRAY</i>	134
	6.2.3 <i>FABRICATION OF THE 2D ANNULAR ARRAY TRANSDUCER</i>	134
6.3	RESULTS AND DISCUSSION.....	137
	6.3.1 <i>PZFLEX SIMULATION RESULT</i>	137
	6.3.2 <i>ACOUSTIC RESPONSE OF THE 2D ANNULAR ARRAY ULTRASOUND TRANSDUCER</i>	141
6.4	SUMMARY	145
CHAPTER 7 CONCLUSION AND FUTURE WORK		146
REFERENCE.....		150
APPENDIX.....		159

TABLE OF FIGURE

Figure 1.1	<i>U.S. device market size from 2014 to 2026(USD Million).....</i>	2
Figure 1.2	<i>Vscan Air, a pocket-sized ultrasound from GE Healthcare⁹.....</i>	3
Figure.1.3	<i>A right kidney ultrasound image by EPIQ 5 ultrasound system for radiology¹⁰.....</i>	4
Figure 1.4	<i>Photography of 50 MHz PVDF polymer (Left) and 60 MHz PZT ceramic (Right) spherically shaped single element transduce^{5,11}.....</i>	4
Figure 1.5	<i>(a) The normal anatomy of the eye and (b) a bugle forward of iris in pupillary glaucoma image captured by a 60 MHz single element transducer¹².....</i>	5
Figure 1.6	<i>UBM images tumour morphology. In this example, an interesting branching structure was detected and imaged (at approximately the same location) on 5 successive days. UBM images are shown on (a) day 6, (b) day 8 and (c) day 10 after the injection of B16 melanoma cells, at which point the two branched regions were completely abutted. (d) A 3D image of the melanoma tumou¹⁵.....</i>	6
Figure 1.7	<i>In vivo imaging of an adult mouse cardiovascular system using the duplex linear array imaging system with a 30 MHz linear array²².....</i>	7
Figure 1.8	<i>The structure of 2D array (Left) and acoustic response of the representative element (Right)²¹.....</i>	8
Figure 1.9	<i>Flowchart of thesis's content.</i>	11
Figure 2.1	<i>The block diagram of the imaging system⁴⁰.....</i>	13
Figure 2.2	<i>(a) The structure of a single cMUT. (b) and (c) The SEM image of a linear array of cMUT⁴¹.....</i>	15
Figure 2.3	<i>The indication diagram of (a) direct piezoelectric effect by applying an elongation on the material and (b) converse piezoelectric effect by applying an electrical potential on the surface of the material³.....</i>	16
Figure 2.4	<i>Basic structure of array transducer with double matching layer.....</i>	17
Figure 2.5	<i>The relationship between classification of piezoelectric and crystal classes⁴³.....</i>	19
Figure 2.6	<i>(a)The polarization hysteresis loop, and (b) the hysteresis loop change with tempearture.....</i>	20
Figure 2.7	<i>The PFM picture representing the microscopic domain structure in single crystal ferroelectric material (a) $Pb(Zn_{1/3}Nb_{2/3})O_3-0.2PbTiO_3$ and (b) $BaTiO_3$. (c) The polarization in polycrystalline ferroelectric material before and after poling^{45,46}.....</i>	21

Figure 2.8	Impedance (blue line) and phase angle (black line) responses of a typical bulk piezoelectric material ⁴⁷	23
Figure 2.9	The relationship between (Left) electromechanical coupling coefficient and bandwidth, and (Right) the band peak shape and quality factor ⁴⁸	25
Figure 2.10	Induction of the acoustic reflection due to the acoustic impedance mismatch.	25
Figure 2.11	KLM model scheme ⁵¹	27
Figure 2.12	Pulse echo shape and frequency spectrum obtained in an experimental echo system using air backing transducers with (a) no front matching, and (b) one quarter-wavelength thickness matching layer $Z=6.0$ MRayl ⁵³	28
Figure 2.13	Pulse echo and frequency spectrum of pUT with (a) $Z=0.5$ MRayl, (b) $Z=5$ MRayl and (c) $Z=24$ MRayl backing layer ⁵³	30
Figure 2.14	Resolution profile in 3-D imaging of array-transducer ⁵⁵	32
Figure 2.15	Ultrasound beam profiles of unfocused and focused single-element transducers ⁵⁵	35
Figure 2.16	The beam profile of a 1-D array with simultaneous excitation (Top) and the dimension structure of the array (Bottom) ⁵⁵	36
Figure 3.1	Acoustic response of the developed transducer with (a) one quarter wavelength matching layer and (b) double quarter wavelength matching layer ⁵³	38
Figure 3.2	(Left) the process flow of the silicon-epoxy 2-2 composite fabrication method. (Right) The cross-section SEM image of the fabricated 2-2 composite ⁸²	40
Figure 3.3	The picture of matching layer under an 8 tons weight in a custom designed mold (Left) and the cured matching layer after the compression (Right).	42
Figure 3.4	The setup (Left) and the fixture (Right) of the measurement of acoustic velocity and attenuation.	43
Figure 3.5	The setup of two-way impulse measurement (Top) and its schematic diagram (Bottom).	47
Figure 3.6	a) The graph of acoustic longitudinal velocity (Black) and density (Blue) versus applied weight and b) the relationship between applied weight and acoustic impedance (Black) or attenuation at 4 MHz (Blue) at a fixed 2:1 aluminum oxide powder to epoxy ratio.	50
Figure 3.7	a) The longitudinal velocity (Black) and density (Blue) versus the weight ratio of aluminum oxide and b) the acoustic impedance calculated by the measured results (Black) and the attenuation versus the weight ratio of aluminum oxide.	52

Figure 3.8	(a), (b) and (c) The scanning electron microscopy image of matching layers developed by centrifuge method with silver powder, centrifuge method with aluminum oxide and high pressure compression method with alumina, respectively, at 100X magnification. (d), (e) and (f) at 2000X magnification.	54
Figure 3.9	The picture of the single element ultrasound transducer attached with the high pressure compressed matching layer.	56
Figure 3.10	The obtained acoustic response of the transducer casted the matching layer fabricated by high pressure compression method (Black) and its frequency spectrum (Blue).	57
Figure 4.1	The experimental set up of laser micro-machining.	67
Figure 4.2	An optical photograph of the surface of the laser micro-machined kerf of the PMN-0.28PT single crystal (laser parameters: 50 to 230 mW, 1 kHz, 0.1mm/s, 1 passes).	67
Figure 4.3	Dependences of the laser power on the kerf width of the PMN-0.28PT single crystal surface with one pass.	68
Figure 4.4	SEM cross-section image of the edge of the laser micro-machined kerf of the PMN-0.28PT single crystal showing the kerf depth as a function of laser power.	68
Figure 4.5	Dependences of the laser power on the kerf depth of the PMN-0.28PT single crystal with one pass.	69
Figure 4.6	An optical photograph of the top of the laser micro-machined kerf of the PMN-0.28PT single crystal (laser parameters: 50mW, 1 kHz, 0.1mm/s, 1 to 10 passes).	70
Figure 4.7	SEM cross-section image of the edge of the laser micro-machined kerf of the PMN-0.28PT single crystal showing the kerf depth as a function of pass number.	71
Figure 4.8	SEM cross-section image of (a) the middle part, (b) area using 50mW laser energy and (c) energy from 125 mW (Left) to 175 mW (Right) of the laser micro-machined kerf of the PMN-0.28PT single crystal.	72
Figure 4.9	SEM cross-section image of the middle part of the laser micro-machined PMN-PT crystal.	73
Figure 4.10	Piezoresponse amplitude images of (a) 20 μm , (b) 50 μm and (c) 100 μm distance away from the 355 nm Nd:YAG laser cut kerf ⁸⁷	74
Figure 4.11	The picture of the dicing blade (model ZHZZ series).	75
Figure 4.12	The surface profile of the diced PMN-0.28PT.	76
Figure 4.13	Cross section of the diced PMN-0.28PT specimen.	77

Figure 4.14	Profile picture of the diced PMN-0.28PT without surface polish treatment (Left) and, with surface polish treatment by 3000 grit sand paper (Right).....	78
Figure 4.15	Profile picture of the diced PMN-0.28PT with surface polish treatment by using 3 μ m polishing paper (~8000 grit).....	78
Figure 4.16	SEM cross-section image of the middle part of the (a) laser micro-machined and (b) diced kerf of the 100 μ m-thick PMN-0.28PT single crystal, bright and dark color denote PMNPT crystal and epoxy, respectively.	80
Figure 5.1	Working mechanism of piezo-meter ¹⁰⁸	86
Figure 5.2	The simulated directivity of the designed elements dimension on the front surface from -90 degree to 90 degree.....	88
Figure 5.3	The simulated directivity of the designed elements dimension on the front surface from -10 degree to 10 degree.....	88
Figure 5.4	The simulated directivity of the designed elements dimension steering at +30 degree (Left) and +60 degree (Right).....	89
Figure 5.5	Schematic diagram of the designed phased array transducer.....	92
Figure 5.6	A schematic diagram of the fabrication procedure of the high frequency phased array transducer.....	94
Figure 5.7	Polarization hysteresis loop of PMN-0.28PT.....	95
Figure 5.8	The profile of kerfs diced by the mechanical dicing saw.....	96
Figure 5.9	Picture of the tungsten wires holder.....	100
Figure 5.10	The setup of the rat cardiac ultrasound imaging.....	101
Figure 5.11	Simulated pulse-echo (black) and frequency (red) spectra.....	103
Figure 5.12	Simulated electrical impedance (black) and phase angle (red) spectra.....	104
Figure 5.13	(a) The 2-D model inputted to the FEM software PZFlex and (b) the simulated 2-D acoustic pressure field of the 2-D phased array ultrasound transducer in water.....	105
Figure 5.14	The pressure field along (a) lateral direction and (b) axial direction.....	106
Figure 5.15	(a)The simulated acoustic pressure at 4 mm focal distance across time and (b) the simulated two-way frequency spectrum of designed phased array transducer.....	106
Figure 5.16	Top view of fabricated phased array transducer.....	108
Figure 5.17	Insertion loss of all 128 elements.....	108
Figure 5.18	Electrical impedance (black) and phased angle (red) of all functional elements.....	109
Figure 5.19	Capacitance (black) and loss (red) of all functional elements.....	109
Figure 5.20	The setup of the two-way impulse measurement.....	110

Figure 5.21	<i>Pulse-echo waveforms of all functional elements displayed in superpositioned (Top) and in waterfall (Bottom).</i>	111
Figure 5.22	<i>Frequency response spectra of all functional elements displayed in superpositioned (Top). The center frequency and -6 dB bandwidth of all 128 elements (Bottom). The center frequency is represented by the square dot. Upper and lower -6 dB frequencies are represented by the error bar.</i>	112
Figure 5.23	<i>Crosstalk of adjacent elements (left and right sides) and one more next to the adjacent elements (left and right) of element #100.</i>	113
Figure 5.24	<i>Wire phantom image of 20 μm tungsten wires.</i>	114
Figure 5.25	<i>Brightness intensity of the representing spot in the wire phantom image (Figure 5.24) along the (a) axial and (b) lateral directions.</i>	115
Figure 5.26	<i>The in-situ imaging setup (Top). (a) The in-situ captured image by the phases-array ultrasound transducer and the structure image of fish eye^{113,114}.</i>	117
Figure 5.27	<i>A cropped brightness image of the in-vivo imaging of a rat's heart captured by the developed phased array ultrasound transducer(Top), and the rat cardiac image captured by VisiualSonics's high frequency ultrasound imaging system(bottom).</i>	118
Figure 6.1	<i>(a) Axial MRI at the level of the mesencephalon equivalent to the TCS image of the mesencephalon. (b) TCS image of the mesencephalic brainstem. 1: hypoechogenic mesencephalic brainstem surrounded by the hyperechogenic basal cisterns; 2: frontoorbital cortex and falx; 3: sulcus lateralis with the middle cerebral artery; 4: cerebellum; 5: temporal lobe; 6: tentorium; 7; contralateral skull¹²⁵.</i>	128
Figure 6.2	<i>Infant and adult cranial ultrasound imaging^{124,125}.</i>	128
Figure 6.3	<i>The schematic structure of the 2D annular array transducer.</i>	131
Figure 6.4	<i>Traditional annular array with Fresnel structure⁸¹.</i>	131
Figure 6.5	<i>Schematics of (a)cross-section view and (b) top view of a piezoelectric layer of Fresnel annular array transducer¹²⁹.</i>	133
Figure 6.6	<i>The profile of the patterned PZT.</i>	135
Figure 6.7	<i>The photo mask used in photolithography.</i>	135
Figure 6.8	<i>Top view and cross-sectional view of the schematic electrical connection diagram in annular 2D array transducer.</i>	136
Figure 6.9	<i>The prototype of the 2D annular array ultrasound transducer.</i>	137
Figure 6.10	<i>The 2D spatial structure of the simulation (Left) and the inputted 3D model (Right).</i>	139

<i>Figure 6.11</i>	<i>Simulated pressure field of one pair of sectors of the 2D annular array(top) and the pressure change along the axial direction at $x=0$.</i>	<i>140</i>
<i>Figure 6.12</i>	<i>The two-way impulse response of (a) center element, (b) first ring, (c) second ring and (d) third ring, along time domain (Black) and frequency domain (Blue).</i>	<i>141</i>
<i>Figure 6.13</i>	<i>Effective electromechanical coupling coefficient of PMN0.3PT and PZT-5 as a function of element's thickness to width ratio¹³⁰.</i>	<i>142</i>
<i>Figure 6.14</i>	<i>Pulse echo frequency spectrum for all five rings of the 40 Hz annular array¹³¹.</i>	<i>143</i>

LIST OF TABLES

<i>Table 2.1</i>	<i>The table of all piezoelectric constants.</i>	<i>22</i>
<i>Table 2.2</i>	<i>Electromechanical coupling coefficient in different resonance mode.</i>	<i>24</i>
<i>Table 2.3</i>	<i>Acoustic impedance of human organs and tissues.</i>	<i>26</i>
<i>Table 2.4</i>	<i>The required acoustic impedance of different matching combination.</i>	<i>27</i>
<i>Table 3.1</i>	<i>The specifications of the high frequency single element transducer.</i>	<i>54</i>
<i>Table 3.2</i>	<i>The optimized specification of each layer of the developed transducer.</i>	<i>55</i>
<i>Table 3.3</i>	<i>Measured acoustic responses of transducers attached with alumina epoxy composite matching layer under high compression pressure at 62.4 MPa and 3:1 weight ratio.</i>	<i>58</i>
<i>Table 3.4</i>	<i>The acoustic properties of matching layer developed by mutilpute method from pervious reported articles.</i>	<i>61</i>
<i>Table 5.1</i>	<i>Measured piezoelectric properties of PMN-0.28PT bulk material.</i>	<i>92</i>
<i>Table 5.2</i>	<i>Properties of different acoustic layers.</i>	<i>103</i>
<i>Table 5.3</i>	<i>List of the designed phased array's specifications.</i>	<i>104</i>
<i>Table 5.4</i>	<i>Measured electrical impedance and phase angle properties of a representative element.</i>	<i>110</i>
<i>Table 5.5</i>	<i>Measured results in the pulse-echo waveform and frequency response spectrum of a representative element.</i>	<i>119</i>
<i>Table 6.1</i>	<i>Measured piezoelectric properties of PZT bulk material.</i>	<i>138</i>
<i>Table 6.2</i>	<i>The dimension of each ring in the 2D annular array ultrasound transducer.</i>	<i>138</i>
<i>Table 6.3</i>	<i>Properties of different acoustic layers.</i>	<i>139</i>
<i>Table 6.4</i>	<i>The two-way acoustic response of the inner first elements along time domain (Black) and frequency domain (Blue).</i>	<i>145</i>

CHAPTER 1

LITERATURE REVIEW AND MOTIVATION OF THESIS WORK

1.1 INTRODUCTION ABOUT MEDICAL ULTRASOUND TRANSDUCER

In medical imaging, the creation of an image from acoustic wave is done with three steps – ultrasound generation, echoes receiving and echoes interpretation. This high-frequency ultrasound wave has a shorter pulse length and less diffraction which make the ultrasound possess a higher dissolving resolution for producing a clearer image. Compared with other medical diagnostic imaging techniques such as X-Ray, magnetic resonance imaging (MRI), computing tomography (CT) etc., medical ultrasound imaging has non-destructive and remarkable low ionizing radioactive merits. These characteristics benefit ultrasound on diagnosing breast cancer and obstetrics due to the extremely high sensitivity of breast tissues and fetus to ionizing radiation.

The market analysis report in 2019 as shown in Figure 1.1 presents that the global ultrasound market size grows continuously from USD 6489.0 million at 2014 to 8015.9 billion USD at 2018¹. The expected CAGR is around 5.5% from 2019 to 2026. This growth rate is similar to the CAGR of MRI from 2021 to 2028². The increased demand of ultrasound imaging systems is mainly attributed to the demand for non-intravascular technology and government recommendation for routine checkups using ultrasound devices. Ultrasound imaging and therapeutic techniques provide a non-radioactive or non-intravascular choice for patients, giving a great opportunity for ultrasound imaging

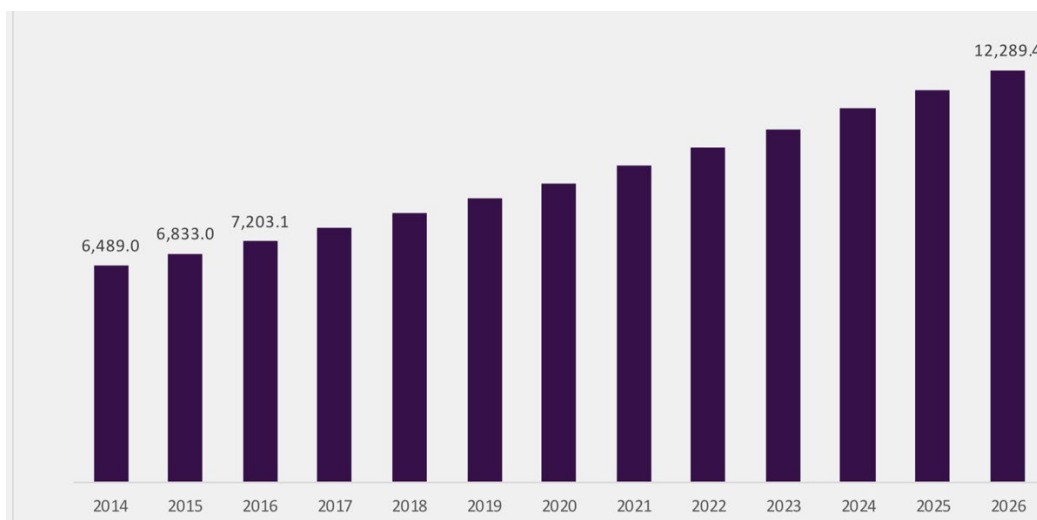


Figure 1.1 U.S. device market size from 2014 to 2026(USD Million)¹.

to extend in areas which are used to rely on radiative diagnostic tools.

In spite of safety issue, ultrasound is a cost effective, portable and real time imaging tool³.

Ultrasound imaging can also acquire novel physiological data, for example, blood flow speed in tissue or vessel. Therefore, ultrasound imaging and simultaneous measuring of dynamic data are suitable for diagnosing moving objects such as cardiograph, ophthalmology and obstetrics⁴⁻⁷. Moreover, the lower price and relatively smaller size make the ultrasound diagnosis system widely applied in extended areas and developing countries for improving the medical service

Besides, the high frame rate of dynamic image acquisition can benefit on veterinary medicine and biology research^{4,5,8}. Especially in biology research, the animal in experiment normally is rat or mouse which has a smaller size than human. The heart bit rate and blood flow of them are significantly higher than human, therefore, it requires a high frame rate and fast responsive imaging technique to record their biological response during the experiment. Moreover, the portable ultrasound imaging system, benefited by mobile and wireless telecommunication techniques, can nowadays be operated in mobile objects like ambulance and medical flying service for emergency medical diagnosis. The

product photo of a portable wireless ultrasound imaging system produced by GE Healthcare is shown in Figure 1.2. With these advantages, ultrasound imaging becomes a valuable diagnostic tool.



Figure 1.2 Vscan Air, a pocket-sized ultrasound from GE Healthcare⁹.

However, only a few commercialized ultrasound imaging systems are employed in clinical, and the situation of ultrasound systems for preclinical is worse than this. Therefore, the application aspect or usage of ultrasound devices are still limited. For example, Philips, which is the biggest market share in ultrasound imaging, is only supporting clinical ultrasound imaging instruments related to diagnoses for obstetrics, gynecology and cardiac. Figure.1.3 shows the picture captured by Philips's ultrasound system EPIQ 5. The center frequencies of those transducers are mostly under 20 MHz for achieving a penetration depth deep enough depending on the human size. On the contrary, laboratory mouse is the main imaging target in biology and medical research. As shown in Figure.1.3, fine details of the human kidney cannot be distinguished

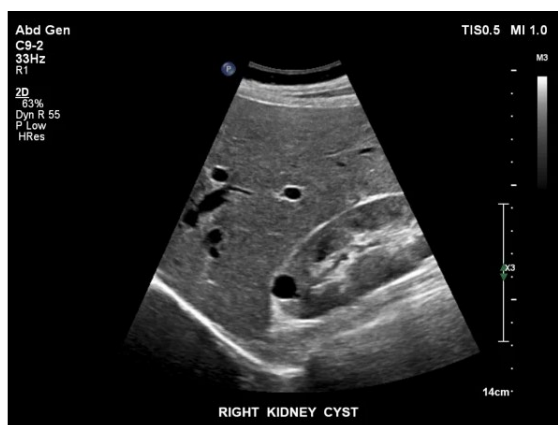


Figure.1.3 A right kidney ultrasound image by EPIQ 5 ultrasound system for radiology¹⁰.

clearly in this image. It indicates that the resolution of the transducer is still not enough for capturing the feature of a smaller scaled objects. Meanwhile, the size of clinical used transducers produced by companies are too large that may affect the mobility of the testing target. The only company that produces high-frequency transducers for small bio-object imaging is VisualSonics. Their products are mainly focusing on linear array transducer from frequencies 10 MHz to 71 MHz and photo-acoustic transducers. The limited development of ultrasound transducer for imaging may affect the progress of research in biology, however, it provides a great opportunity for academia to investigate and improve the ultrasound transducer for not only clinical ultrasound imaging but also some new imaging techniques assisting academic research on medicine.

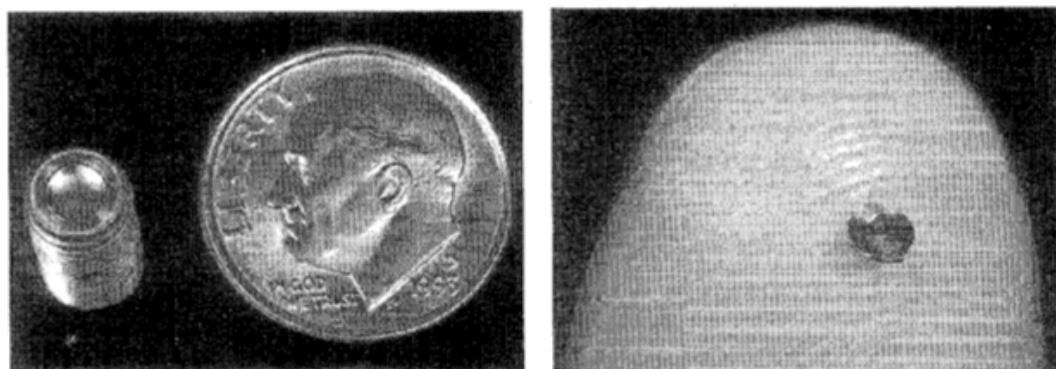


Figure 1.4 Photography of 50 MHz PVDF polymer (Left) and 60 MHz PZT ceramic (Right) spherically shaped single element transduce^{5,11}.

1.2 DEVELOPMENT OF ULTRASOUND TRANSDUCERS

Application of ultrasound biomedical imaging has been investigated academically since 1989. In early time, only single element transducer was made to produce an ultrasound medical image due to the fabrication difficulty and insufficient computing technology. Figure 1.4 shows polymer-based and ceramic-based focusing single element ultrasound transducers at high frequencies^{5,11}. The increased center frequency gives rise to the resolution so that the transducer can capture the feature of human eyes assisted by mechanical scanning¹²⁻¹⁴. Pavlin *et al.* has developed a 60 MHz-transducer for glaucoma imaging in 1992¹². The human eye scanned by 60 MHz single element transducer is shown in Figure 1.5.

High-frequency ultrasound imaging has also been applied on skin tumor staging, boundary definition, dynamic studies of the response of tumors and investigation of inflammatory skin disease. A 50 MHz or even 100 MHz frequency transducer reported by Passmann *et al.* in 1993 has produced a clear visualization of structures in epidermis and

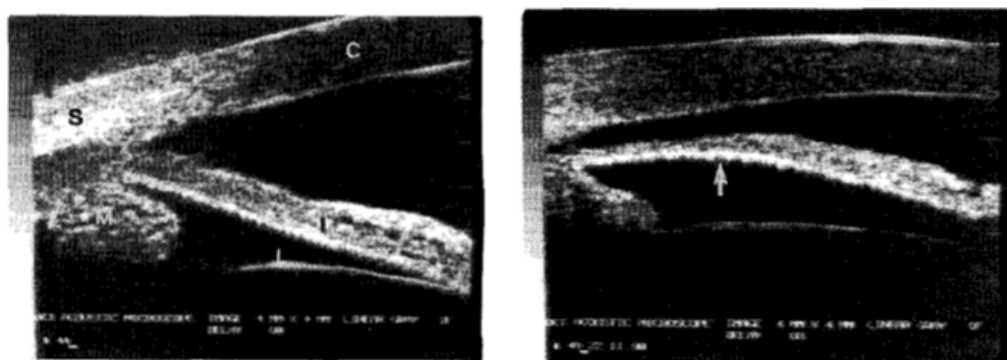


Figure 1.5 (a) The normal anatomy of the eye and (b) a bulge forward of iris in pupillary glaucoma image captured by a 60 MHz single element transducer¹².

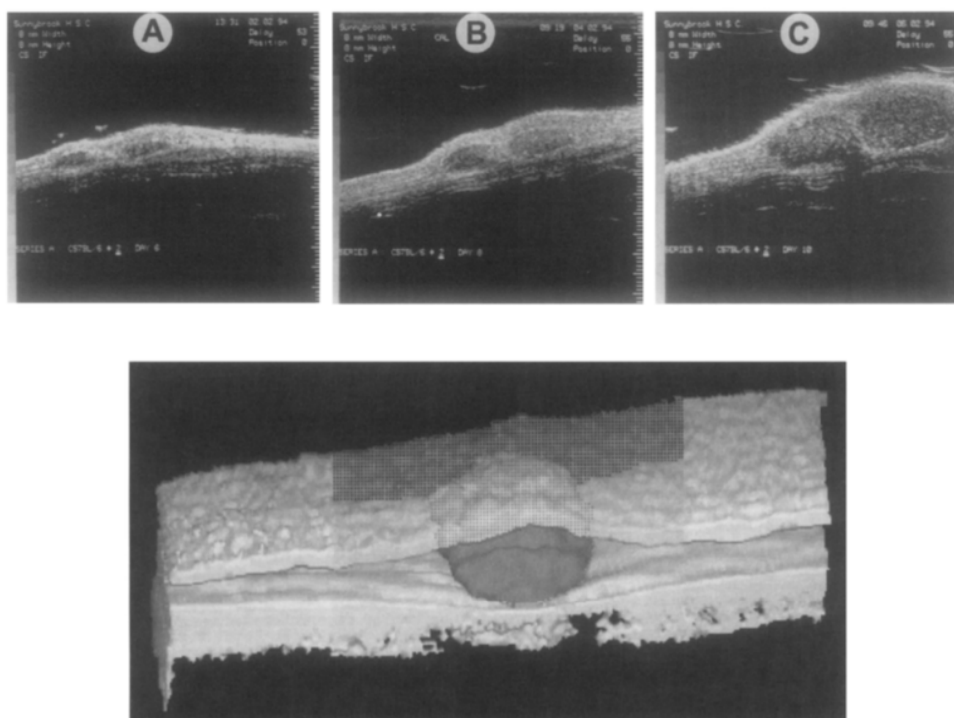


Figure 1.6 UBM images tumour morphology. In this example, an interesting branching structure was detected and imaged (at approximately the same location) on 5 successive days. UBM images are shown on (a) day 6, (b) day 8 and (c) day 10 after the injection of B16 melanoma cells, at which point the two branched regions were completely abutted. (d) A 3D image of the melanoma tumour¹⁵.

superficial dermis¹⁶. Mechanical scanning along axial direction has presented simultaneously for compensating the narrow depth of field drawback of an ultra-high frequency ultrasound transducer. Scientists have also applied the ultrasound imaging on measuring the growth of cutaneous melanoma to prognosticate the melanoma cancer in early state¹⁷. The ultrasound image of a growing melanoma tumour reported by Turnbull *et al.* in 1996 is shown in Figure 1.6¹⁵. Figure 1.6 (d) also shows a computer rendering 3D image composited by multiple 2D images. However, using the single element transducer, the 2D image frame around 5 frames per second is relatively low. Therefore, in recent years researchers are mainly focusing on linear array investigation to implement a higher frame rate 2D ultrasound images, resulting in a real time 3D ultrasound image.

A real time cardiac image of an adult mouse shown in Figure 1.7 was reported by Zhang *et al.* in 2010. The image was acquired by a 30 MHz 64-elements linear array transducer with frame rate of 400 fps. A Doppler blood flow measurement for small animal with a wide range of detection from 0.1 mm/s to 1m/s was presented by the high frame rate linear array transducer. Furthermore, a 2D array ultrasound transducer design and study for clinical imaging at low frequency has been suggested since 1998¹⁸⁻²⁰. Butreau *et al.* has developed and tested a 50×50 2D array transducer prototype as shown in Figure 1.8²¹.

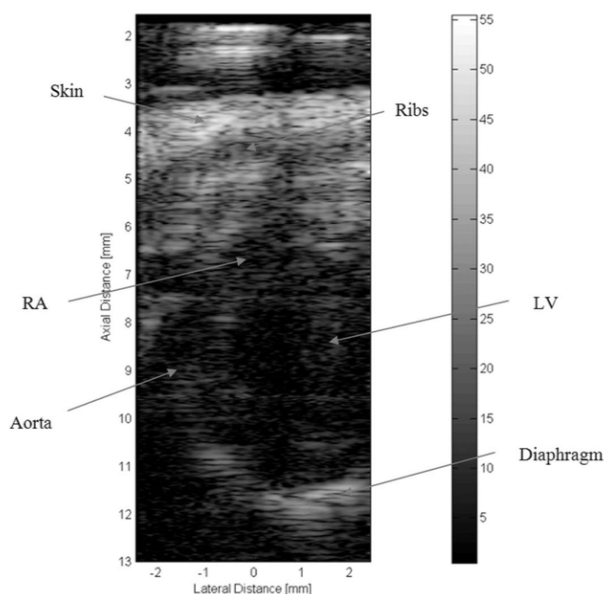


Figure 1.7 *In vivo* imaging of an adult mouse cardiovascular system using the duplex linear array imaging system with a 30 MHz linear array²².

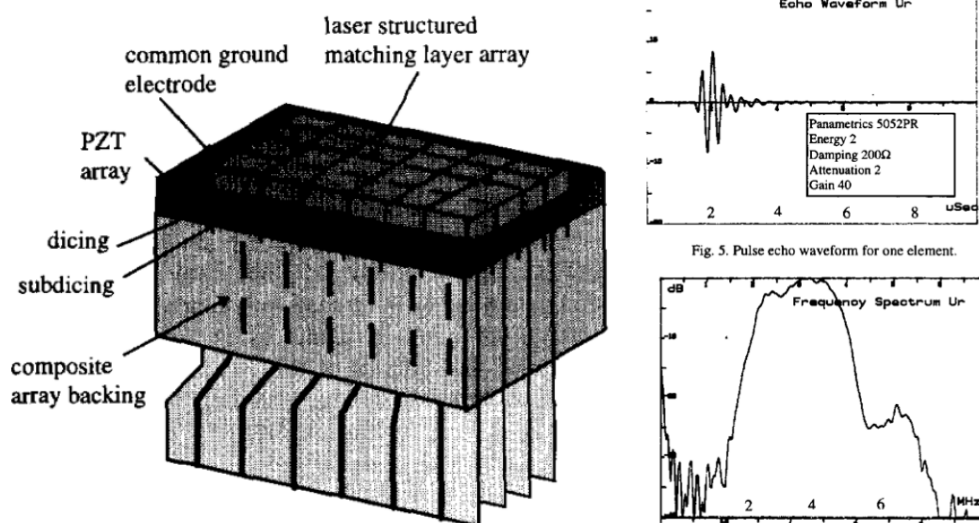


Figure 1.8 The structure of 2D array (Left) and acoustic response of the representative element (Right)²¹.

Recently, research of ultrasound transducer for medical imaging can be divided into three main directions: new materials for transducers targeting at performance improvement, new fabrication method of transducer or its component, and new application of transducers. New materials with high piezoelectric properties, such as lead indium niobate-lead magnesium niobate-lead titanate(PINMT), lead magnesium niobate-lead titanate(PMNPT) and Sm-doped PMNPT, have been utilized in different types of transducers for maximizing transducer's performance²³⁻²⁷. Apart from new materials, new fabrication process of transducers are also studied^{28,29}. For instance, a highly regular, collinear, porous alumina samples using a chemical anodizing process was reported. By varying the porosity of the matching layer, impedance was varied from 5 to 18 MRayl³⁰⁻³³. Matching layers made of 1-3, 2-2 or 0-3 composites configuration were reported³⁴⁻³⁶. In term of new applications, ultrasound transducers have been routinely used for lung ultrasound in patients with the COVID-19 disease pandemic^{37,38}.

1.3 MOTIVATION OF THIS THESIS WORK

In recent years, many groups of researchers are investigating the improvement of ultrasound transducers for different medical applications as mentioned in previous session. From a single element ultrasound transducer to 2D array design, there has been a great interest in studying ultrasound transducers. Owing to the favourable factors, including non-ionizing radiation, non-destructive, high-frame rate for dynamic data acquisition, fast-responsive and portable imaging techniques, ultrasound transducers offers an opportunity to be one of the promising alternatives for medical diagnoses and therapeutic applications. It is worth to study the characteristics of high-frequency ultrasound transducers. Yet, there are still a plenty of rooms for the ultrasound transducer development. The majority of ultrasound applications is in large macroscopic scale, lack of the investigation in smaller scale applications.

The motivation of this thesis is to investigate the high-frequency ultrasound transducers for different medical applications from cardiac to brain arteries and to study the improvement for ultrasound transducer in medical imaging. Although there are several clinical products providing imaging diagnosis from cardiac, the resolution for fine structure is limited by the bandwidth and sensitivity. In order to obtain a better visualization of target tissue, *in vivo* ultrasound imaging with high resolution should be demonstrated. By improving the frame rate and enlarging the steering angle using different transducer array design, the improvement of small features visualization and even 3D image capture can be further explored.

In addition, by modulating the acoustic properties of the components of ultrasound transducer, the performance of transducers can be enhanced. It is well-known that the reflection and transmission of acoustic wave depend on the acoustic impedance mismatch

between two mediums. A high acoustic impedance matching layer is important to optimize the acoustic wave transmission because of the significantly large acoustic impedance difference between ultrasound generating material (i.e. ~ 30 MRayl for piezoelectric material) and human tissues and organs (i.e. ~ 1.6 MRayl). Otherwise, most of the signal intensity will be reflected if the piezoelectric material is in direct contact to the loading medium. Therefore, it offers an opportunity of matching layer to become one of the most critical candidates for the performance determination of piezoelectric-based ultrasound transducers. The first objective of this thesis work is to develop a fabrication process and advanced acoustic materials for transducer's performance improvement. Then, we will focus on the development of small animal image acquisition using high-frequency phased array transducer. An advanced cranial ultrasound imaging application apart from infant brain imaging will also be investigated by designing a new-structured 2D annular array transducer.

1.4 SCOPE OF THE THESIS

In this thesis, seven chapters are organized. A flowchart of this thesis content is shown in Figure 1.9.

Chapter 1: The overview of ultrasound transducers is introduced. Improvement and investigation of the previous research about the high frequency (≥ 20 MHz) phased array ultrasound transducer are introduced³⁹. Followed by the brief description of transducers development in medical imaging, the motivation and objectives of the present work are given in this Chapter.

Chapter 2: Literature review of ultrasound transducers is reported. Followed by the introduction of ultrasound imaging system, characteristics and properties of

transducer and its component as well as the corresponding relationship to transducers' performance are described.

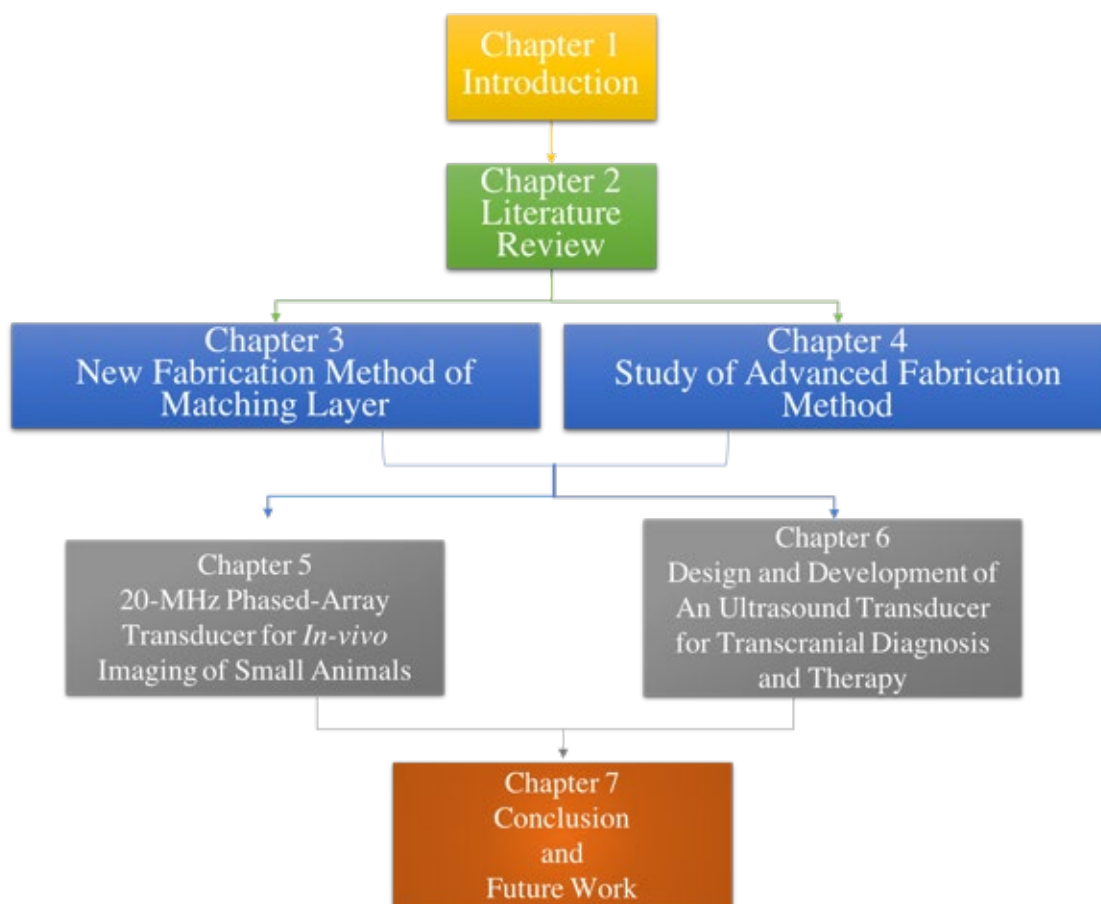


Figure 1.9 Flowchart of thesis's content.

Chapter 3: The influence of advance materials on transducers' performance are reported. By using high pressure compression, a new matching layer development method has been presented. The manipulative longitudinal velocity and acoustic impedance of the developed matching is described by modulating applied pressure and component weight ratio.

Chapter 4: Fabrication process of single crystal patterning is studied. By comparing laser cutting method and mechanical dicing method, the limitation, possible

failures and the manufacturing difficulties, especially for single crystal material PMN-0.28PT, during fabrication are analyzed.

Chapter 5: Phased array transducer based on a PMN-0.28PT single crystal relaxor ferroelectric material is fabricated. A high uniformity and performance, including high sensitivity and bandwidth, is demonstrated. Accompanied by high resolution verification, an *in-vivo* medical brightness-mode (B-mode) imaging acquisition for small scaled organism or tissues, such as fisheyes and heart of rat, is demonstrated.

Chapter 6: An annular array is invented based on the Fresnel structure. Acoustic properties of the annular array transducer are tested, and simulation result and experimental result of the 2D annular array shows the coincident relationship. Then, the possibility of conical 3D imaging through a small aperture due to the annular design is achieved. The ability for imaging and stimulation simultaneously is also examined.

Chapter 7: Conclusion and future prospect are given.

CHAPTER 2

INTRODUCTION TO ULTRASOUND TRANSDUCER

2.1 ULTRASOUND IMAGING SYSTEM

Normally, an ultrasound imaging system has three main parts which are the data processing system, electrical signal processing system and ultrasound transducer (UT). Figure 2.1 shows the block diagram of an imaging system⁴⁰. The data processing system controls the pulse emission pattern, processing the received data, receiving the user commands and displaying the image. Electrical signal processor contents a complex electrical circuit converting the digital signal to analog, multiplexing and amplifying the signal. The ultrasound transducer is a device that converts an electrical signal to an

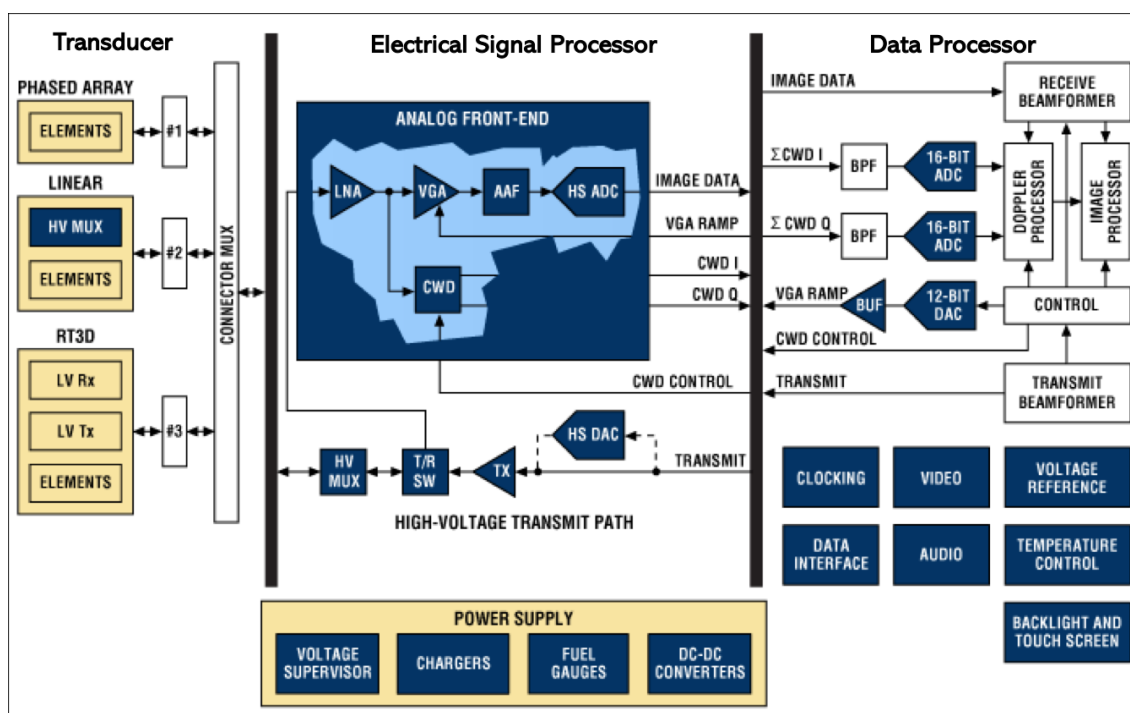


Figure 2.1 The block diagram of the imaging system⁴⁰.

acoustic signal and vice versa. This electrical to mechanical energy conversion can be done through capacitive or piezoelectric effect. However, in this chapter, only the piezoelectric method is focused. After transmitting an acoustic pulse, the UT can also transform the reflected acoustic pulse (echo) from the target to an electrical pulse signal. The characteristics of the received echo can be analyzed by the data processing system to produce an image represented by brightness spots in the B-mode image. Alternatively, by using different types of ultrasound transducers or different scanning methods, 2-dimensional (2-D), 3-dimensional (3-D) or even real time 3-D (4-dimensional (4-D)) imaging can be performed.

2.1.1 Mechanism of ultrasound transducer

The ultrasound wave for medical imaging is mainly artificially generated by two ways. The first one is using a capacitive method, called capacitive ultrasound transducer (cUT). The second way is using a piezoelectric material's vibration to generate an acoustic wave called piezoelectric ultrasound transducer (pUT). Most of the ultrasound transducer nowadays are using the pUT method. The mechanism of both cUT and pUT will be illustrated in the following sections.

2.1.1.1 Capacitive based

In cUT, the capacitance change is caused by applying an AC signal on a metal coated membrane which is constructed on semiconductor materials using micromachining technology. The change of capacitance generates mechanical vibration, i.e. ultrasound wave, so the device is also called capacitive micro-machined ultrasound transducer (cMUT). The membrane vibration has the same frequency of the applied ac signal, so an

ultrasound wave can be generated in the medium if the ac signal has a frequency higher than 20 kHz. The structure of the cMUT is shown in Figure 2.2⁴¹. Since cMUT uses the micromachining technique, it is easy to be fabricated in an array format with massive number of elements in a small area for generating a high-resolution image. The advantages of the cMUT include robust design, low cost in IC manufacturing, high level of integration, miniaturization, easy for producing high-frequency device and lead free for disposable. However, the acoustic power generated by cMUT is generally much lower compared to pUT.

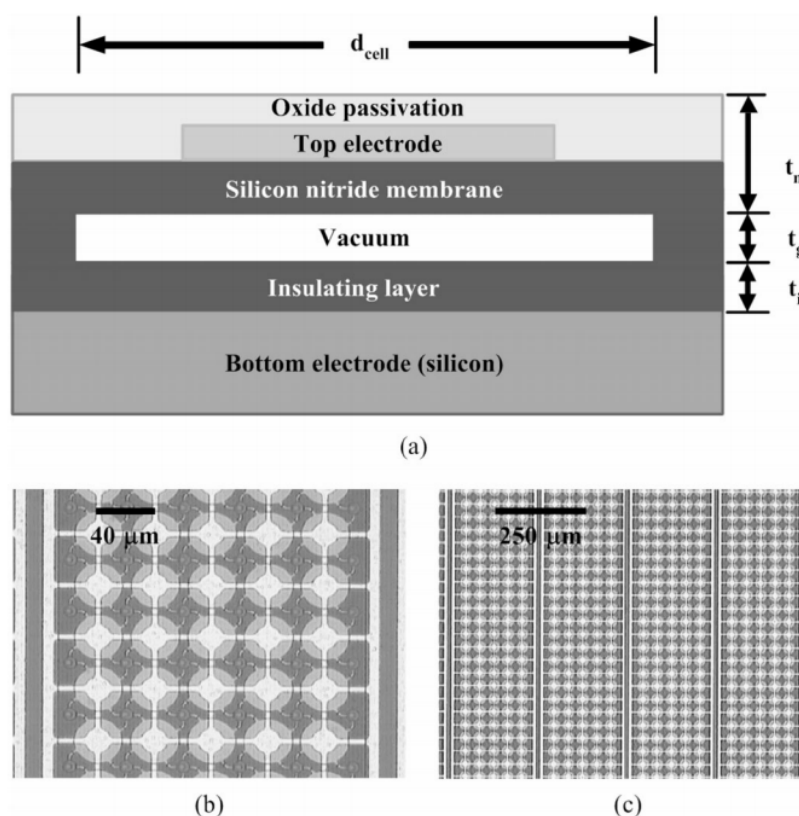


Figure 2.2 (a) The structure of a single cMUT. (b) and (c) The SEM image of a linear array of cMUT⁴¹.

2.1.1.2 Piezoelectric based

The second way to produce an ultrasound is using a piezoelectric material. Piezoelectric

materials possess piezoelectric effect that transfers mechanical stress to electric charges on the material's surfaces or vice versa. The piezoelectric effect was first discovered and demonstrated by two French scientist Pierre Curie and Paul-Jacques Curie in 1880⁴². The mechanical stress applied on the material deforms the lattice to elongate or compress, resulting in surface charges corresponding to the internal electric polarization. Since the piezoelectric effect is a reversible effect, it has been divided into direct piezoelectric effect and converse piezoelectric effect defined by the mechanical input or electrical input, respectively. Both of the mechanism diagrams are shown in Figure 2.3³.

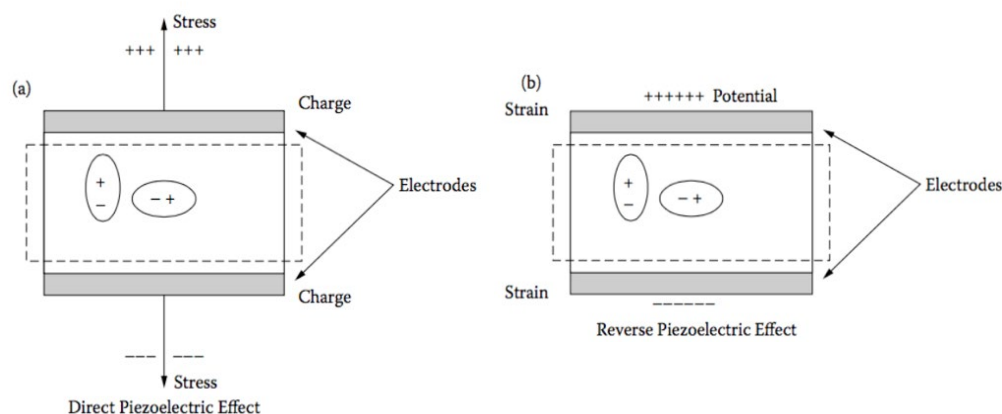


Figure 2.3 The indication diagram of (a) direct piezoelectric effect by applying an elongation on the material and (b) converse piezoelectric effect by applying an electrical potential on the surface of the material³.

2.2 CHARACTERISTIC OF PIEZOELECTRIC ULTRASOUND TRANSDUCER

In this section, the factors affecting the resolution and sensitivity of transducers are elaborated and investigated in detail for designing a suitable transducer that can accomplish biomedical imaging for different purposes.

2.2.1 Structure of piezoelectric ultrasound transducer

In general, an ultrasound transducer consists of three main components including an

active element, a matching layer and a backing layer. Figure 2.4 illustrates the basic structure of a typical array transducer. Same as the description in section 2.1.1, the active layer piezoelectric layer uses the piezoelectric effect to convert an electrical signal into an acoustic signal and vice versa. The mechanism of the piezoelectric material being the active layer depends on the piezoelectric effect that an external electric field applied on the piezoelectric material redirects the dipoles inside the material, and thus a strain is generated in either the lateral direction or the longitudinal direction. Similarly, an AC electric field applying on the piezoelectric material can induce its vibration. The vibration frequency would depend on the AC electric field frequency and the intrinsic characteristics of the piezoelectric material. Consequently, the vibration of the piezoelectric material vibrates the molecules of the surrounding medium, and then generates an acoustic pulse based on the resonance frequency of the piezoelectric material.

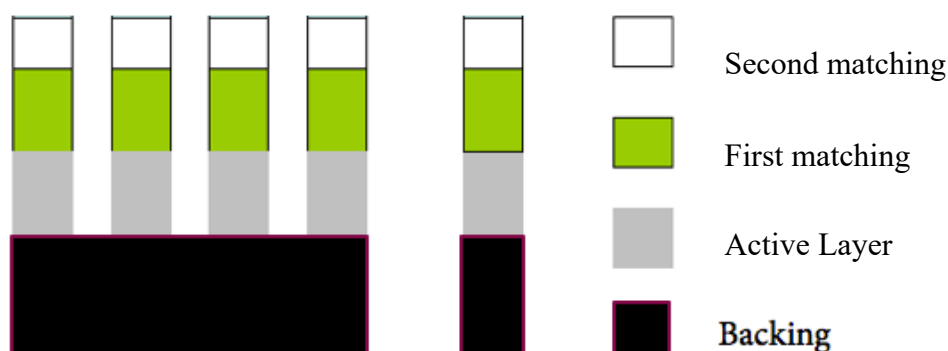


Figure 2.4 Basic structure of array transducer with double matching layer.

The second component is the matching layer. The main effect of matching layer is enhancing the transmission rate of the ultrasound wave between the active layer and the loading medium. The impedance gradient can be reduced by inserting single or multiple matching layers in-between. The enhanced transmission rate would increase the energies of transmitted and received acoustic waves, and therefore, enhance the sensitivity of the

ultrasound transducer. The third component is the backing layer whose mechanism is very similar to that of the matching layer. The only difference is that the function of backing layer intends to absorb the acoustic wave propagating through the backside of the ultrasound transducer, which is the direction opposite to the target.

2.2.1.1 Piezoelectric properties of active layer

The factors affecting the performance of the UT are the piezoelectric properties of the material, the matching layer and the electrical coupling. Piezoelectric properties induce the strength of the piezoelectric effect. It not only affects the sensitivity of the transducer but also the resolution of the transducer. A piezoelectric material with a stronger piezoelectric property can generate a larger strain to the loading medium and has a relatively less energy loss during the conversion.

Piezoelectric crystal structure

The origin of piezoelectricity can be explained by the crystal structure of the material. According to the crystallographic, which has been shown in Figure 2.5, 21 classes out of 32 solid materials crystal classes are non-centrosymmetric. Except of the class 432, the non-centrosymmetric structure can present piezoelectricity that includes 10 classes of non-polar crystal class essentially performing a change from non-polar crystal to polar crystal while applying a mechanical load. More specific, the applied mechanical load induces ion displacement a net electric dipole moment change that produces surface charges. Another 10 classes have polar axis that exhibits permanent polarization, called spontaneous polarization, even after the external mechanical stress or electrical field is removed. These 10 classes can be stated as pyroelectric, in which the spontaneous

polarization is temperature dependent; thus charges will be generated when the polarization is affected by temperature change. Furthermore, some of the pyroelectric material's polarization direction can also be switched. These materials can be stated as the ferroelectric materials that can produce piezoelectricity for generating a strong ultrasound signal.

A ferroelectric shows a unique of polarization hysteresis as shown in Figure 2.6(a). In the figure, P_s is the saturation polarization of the material which is the maximum polarization of the material with presence of an electrical field. P_r is called the remnant polarization, which is the polarization remained after the external E-field is removed from a ferroelectric material. E_c is called coercive field whose physical meaning is the minimum

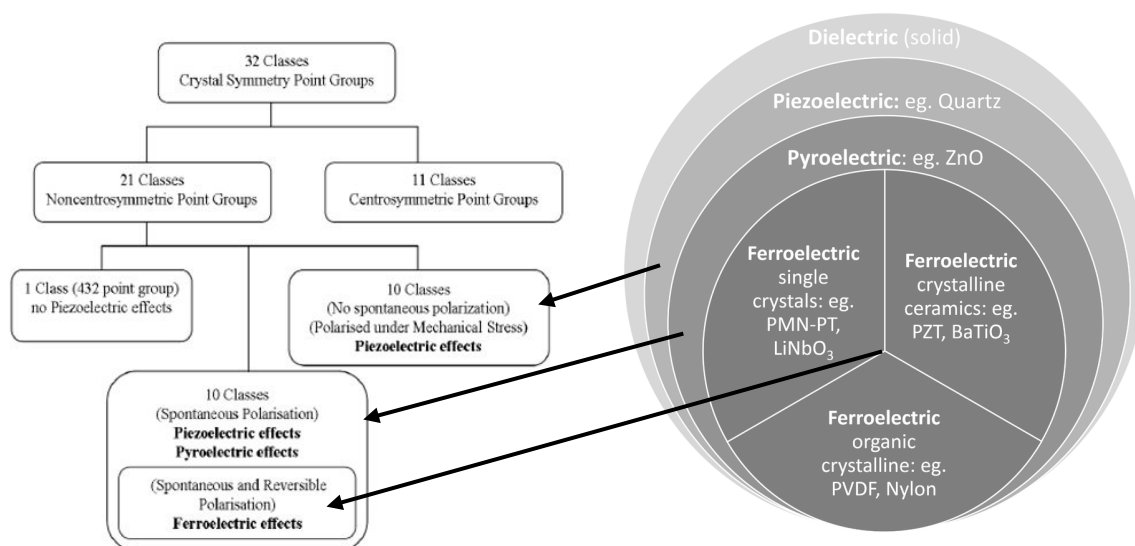


Figure 2.5 The relationship between classification of piezoelectric and crystal classes⁴³.

external electric field that can switch the polarization direction of the ferroelectric material. Figure 2.6 (b) also shows the relationship between the polarization hysteresis loop and temperature. The saturation polarization and the spontaneous polarization of the

ferroelectric decreases when temperature increases. However, the coercive field of the ferroelectric also reduces with the increase of temperature. This is an important phenomenon that has been applied on the ferroelectric's polarizing process, which is called as polling process. The polling process is to make a ferroelectric sample polarized by applying a static electric field on surface of the material. The macroscopic polarization appears after the polling process. A polling process operated at a high temperature can reduce the necessary electric field for poling and the risk of break-down of the material or ionizing the medium around the material.

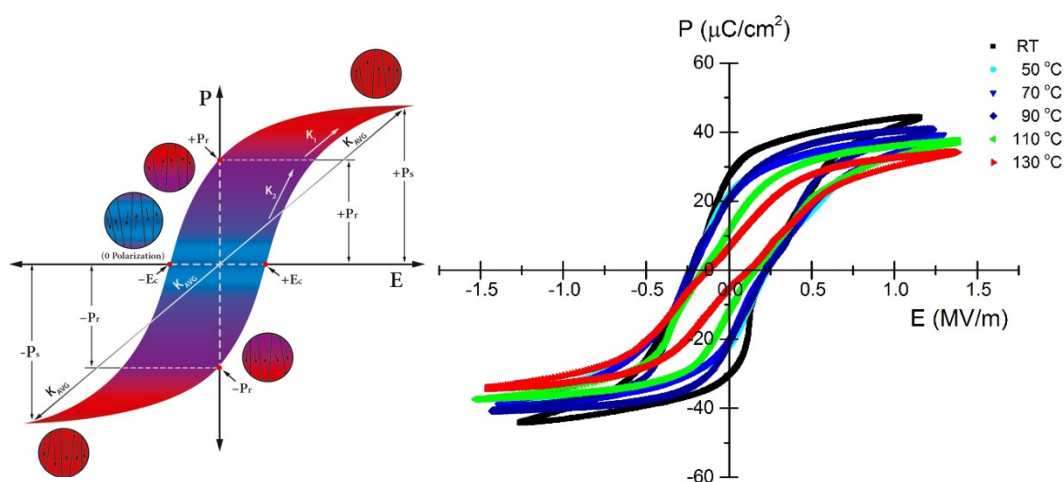


Figure 2.6 (a)The polarization hysteresis loop, and (b) the hysteresis loop change with temperature.

Mechanical oscillations generated from piezoelectric effect compress and decompress the medium and generate an acoustic signal propagate through the medium. The generated acoustic waveform and its frequency are controlled by the applied electrical field and the piezoelectric properties of the material. Piezoelectric materials mostly are solid ceramic-based materials in single crystal or polycrystalline structure. In recent decade, some biological matter such as bone, tendon, DNA and different proteins, have been discovered as a piezoelectric material⁴⁴. Focusing on the solid materials, single crystal structured ferroelectric materials normally possess higher piezoelectric properties than

polycrystalline material due to the structure affects the microscopic or even nanoscopic polarization. Figure 2.7 shows the polarization microscopically in a single crystal, and polycrystalline structure^{45,46}. The microscopic domain structure of two single crystal based ferroelectric $\text{Pb}(\text{Zn}_{1/3}\text{Nb}_{2/3})\text{O}_3\text{-}0.2\text{PbTiO}_3$ and BaTiO_3 are shown in (a) and (b), respectively. The absence of grain boundary in a single crystal results in a mono-axial

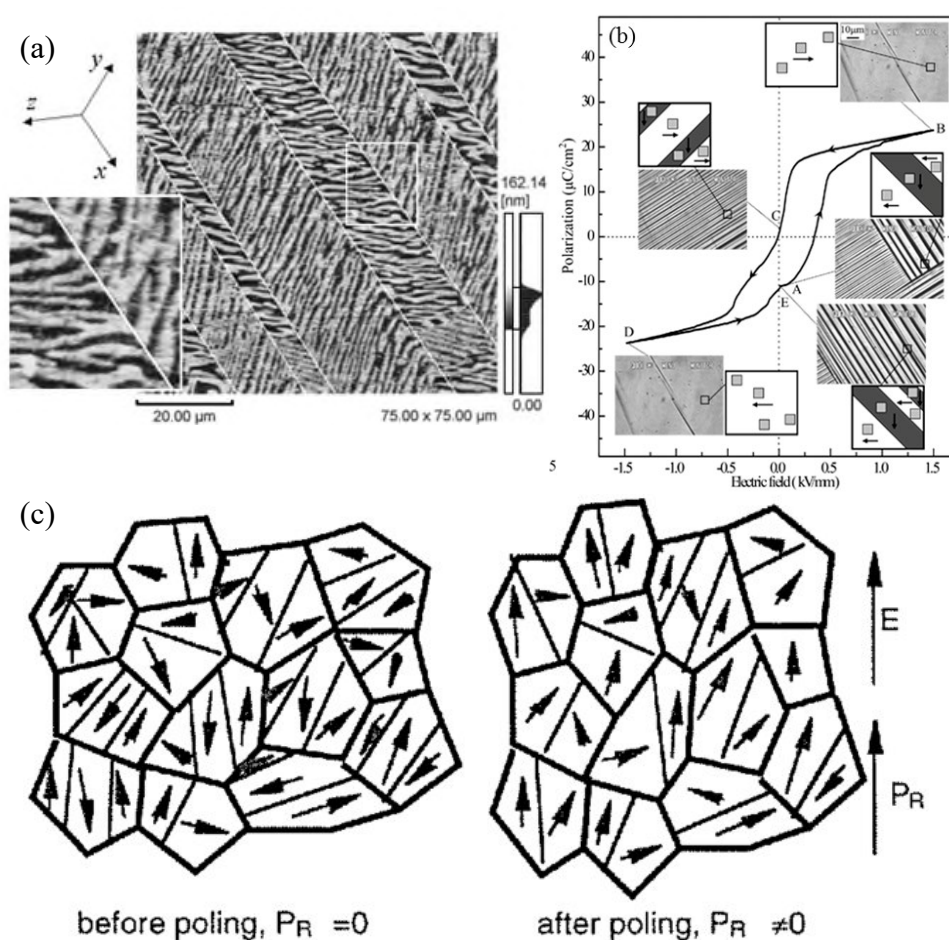


Figure 2.7 The PFM picture representing the microscopic domain structure in single crystal ferroelectric material (a) $\text{Pb}(\text{Zn}_{1/3}\text{Nb}_{2/3})\text{O}_3\text{-}0.2\text{PbTiO}_3$ and (b) BaTiO_3 . (c) The polarization in polycrystalline ferroelectric material before and after poling^{45,46}.

polarization in a large area according to the domain pattern shown in Figure 2.7(a) and (b) at points B and D. On the other hand, in the polycrystalline ferroelectric, the domains inside the grain grow when the external E-field is presented. However, the random aligned

grain boundaries block the domain growth, therefore the microscopic polarization aligned in non-axial direction resulting in a lower overall spontaneous polarization (Figure 2.7(c)).

Piezoelectric constant

One of the parameters that affects the performance of the UT is the piezoelectric constant. There are four different types of piezoelectric constants illustrating the strength of the piezoelectric effect conversion under different circumstances and directions. Table 2.1 lists all the direct and converse piezoelectric constants under all the circumstances.

TABLE 2.1 THE TABLE OF ALL PIEZOELECTRIC CONSTANTS.

	Direct	Converse
d_{ij}	$= \left(\frac{\partial D_i}{\partial T_j} \right)^E$	$= \left(\frac{\partial S_j}{\partial E_i} \right)^T$
e_{ij}	$= \left(\frac{\partial D_i}{\partial S_j} \right)^E$	$= - \left(\frac{\partial T_j}{\partial E_i} \right)^S$
g_{ij}	$= - \left(\frac{\partial E_i}{\partial T_j} \right)^D$	$= \left(\frac{\partial S_j}{\partial D_i} \right)^T$
h_{ij}	$= - \left(\frac{\partial E_i}{\partial S_j} \right)^D$	$= - \left(\frac{\partial T_j}{\partial D_i} \right)^S$

Where D , E , S and T represent electric displacement, electric field strength, strain and stress, respectively. i and j are the vectors of the inducer and trigger. The power of the equation is the constant factor. By comparing the formulas listed in the table and the realistic situation, the direct piezoelectric effect for transferring an ultrasound signal to electrical signal is the factor g_{ij} . Besides, the converse piezoelectric effect for generating the ultrasound signal is the factor d_{ij} . For a piezoelectric material with large values of g_{ij}

and d_{ij} , a stronger received electrical signal or emitted ultrasound signal can be achieved. Consequently, a higher sensitivity of the UT can be achieved by using a material possessing a high g_{ij} or d_{ij} .

Electromechanical coupling coefficient

Instead of the piezoelectric constant, electromechanical coupling coefficient k_{ij} of the piezoelectric layer is another piezoelectric property showing the efficiency from electrical to acoustic transformation of a piezoelectric material. The value of the coupling coefficient is between 0 to 1, which can also be a percentage of the energy conversion.

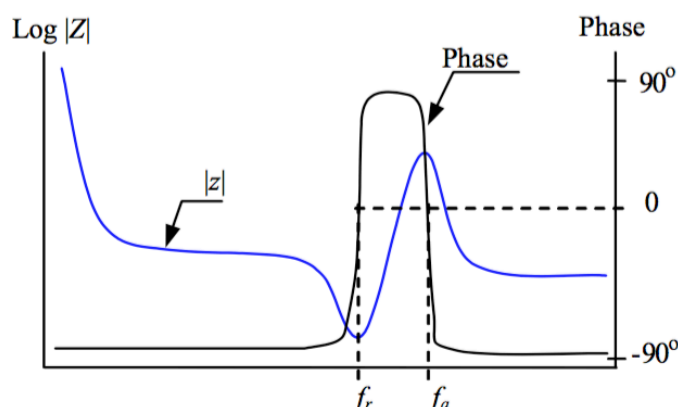


Figure2.8 Impedance (blue line) and phase angle (black line) responses of a typical bulk piezoelectric material⁴⁷.

According to the frequency and direction dependence phenomena, the formulas of the electromechanical coupling coefficients are shown in the following Figure2.8. Where d_{ij} is the piezoelectric constant, ϵ_{ij}^T the permittivity under constant stress, f_a and f_r the anti-resonance and resonance frequencies of the material, respectively. Sensitivity may be higher if the transducer uses a material with higher electromechanical coupling coefficient. By considering the equation at high frequency, the coefficient is proportional to the frequency difference between the resonance and anti-resonance. According to the

equation of the mechanical quality factor Q_m of the piezoelectric showing in (1), the

$$Q_m = \frac{f_a^2}{2\pi f_r C_0 Z_r (f_a^2 - f_r^2)} \quad (1)$$

TABLE 2.2 ELECTROMECHANICAL COUPLING COEFFICIENT IN DIFFERENT RESONANCE MODE.

	Static or low frequency	High frequency
k_p^2	$= \frac{2d_{31}^2}{((s_{11}^E + s_{12}^E)\epsilon_{33}^T)}$	$= \frac{2.51(f_a - f_r)}{f_a} - \left(\frac{f_a - f_r}{f_a}\right)^2$
$k_t^2 = k_{15}^2$	$= \frac{d_{33}^2}{\left(\frac{1}{s_{33}^E} + \frac{d_{33}^2}{\epsilon_{33}^T}\right)\epsilon_{33}^T}$	$= \frac{\pi f_r}{2 f_a} \tan\left(\frac{\pi}{2}\left(\frac{f_a - f_r}{f_a}\right)\right)$
k_{33}^2	$= \frac{d_{33}^2}{(s_{33}^E \epsilon_{33}^T)}$	$= \frac{\pi f_r}{2 f_a} \tan\left(\frac{\pi}{2}\left(\frac{f_a - f_r}{f_a}\right)\right)$
k_{31}^2	$= \frac{d_{31}^2}{(s_{11}^E \epsilon_{33}^T)}$	$= \frac{\frac{\pi f_a}{2 f_r} \tan\left(\frac{\pi}{2}\left(\frac{f_a - f_r}{f_r}\right)\right)}{1 + \frac{\pi f_a}{2 f_r} \tan\left(\frac{\pi}{2}\left(\frac{f_a - f_r}{f_r}\right)\right)}$

quality factor is anti-proportional to the frequency difference between the resonance and anti-resonance, thus the quality factor also anti-proportional to the k_{ij} . The quality factor presenting the mechanical loss of the material as well as the amplitude sharpness along the frequency domain. The relationship between mechanical loss ($\tan \delta_m$), quality factor, and bandwidth has been illustrated as follows:

$$\tan \delta_m = \frac{1}{Q_m} = \frac{2\Delta\omega}{\omega_0} \quad (2)$$

While the ω_0 and $\Delta\omega$ are the center frequency and the bandwidth of the mechanical response. To conclude, the mechanical coupling coefficient is proportional to the frequency bandwidth of the piezoelectric material. Figure 2.9 shows the bandwidth

change with the electromechanical coupling coefficient enhancement⁴⁸. Besides, Figure 2.9 also shows that the band edge becomes sharper (representing a lower loss) while the quality factor is increased, which may also affect the frequency bandwidth of the pUT. Thus, k_{ij} coefficient is also a critical factor controlling both the resolution and sensitivity of pUT.

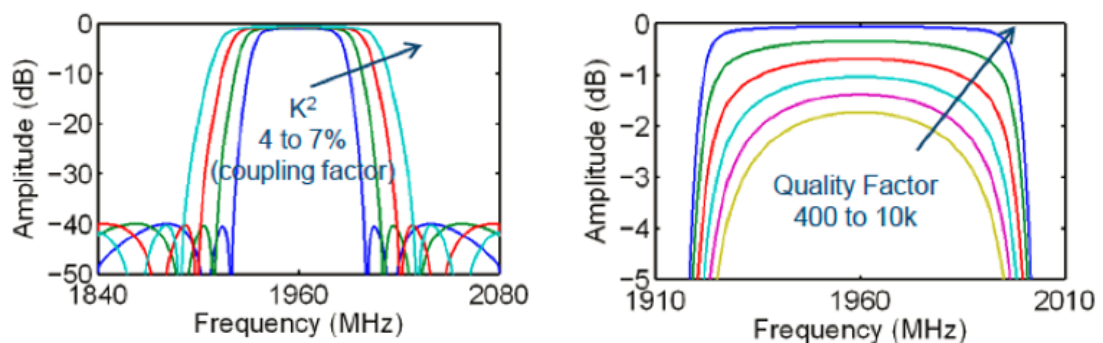


Figure 2.9 The relationship between (Left) electromechanical coupling coefficient and bandwidth, and (Right) the band peak shape and quality factor⁴⁸.

2.2.1.2 Matching layer

A matching layer definitely plays an important role in enhancing the sensitivity of the pUT. The matching layer can adjust both sensitivity and bandwidth of the UT in emission and receiving process.

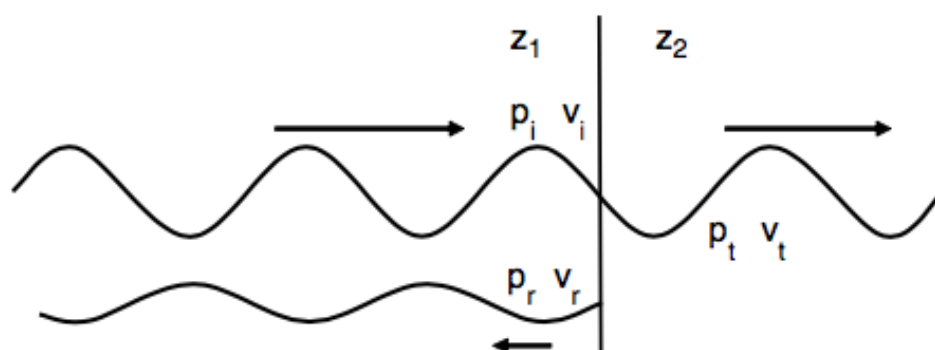


Figure 2.10 Induction of the acoustic reflection due to the acoustic impedance mismatch.

The acoustic reflective (R_i) and transmission (T_i) coefficients are dependent on the acoustic impedance mismatch between two mediums. Figure 2.10 shows an acoustic wave propagates through two mediums with different acoustic impedances Z_l and Z_2 . The equation of reflective and transmission coefficients are shown as follows⁴⁹:

$$R_i = \frac{Z_l - Z_p}{Z_l + Z_p} \quad (1)$$

$$T_i = \frac{2Z_p}{Z_l + Z_p} \quad (2)$$

Where Z_l and Z_p are the acoustic impedance of the loading medium and the piezoelectric material, respectively.

TABLE 2.3 ACOUSTIC IMPEDANCE OF HUMAN ORGANS AND TISSUES.

Body Tissue	Acoustic Impedance (MRayl)
Air	0.0004
Lung	0.18
Fat	1.34
Liver	1.65
Blood	1.65
Kidney	1.63
Muscle	1.71
Bone	7.8

Targeting at clinical ultrasound imaging, the human tissues has around 1.5 MRayl (shown in Table 2.3) and most of the piezoelectric has an impedance around 32 MRayl, thus over 80% of the signal intensity is reflected if the ceramic based piezoelectric material is in direct contact with the loading medium. Therefore, to optimize the propagation intensity, a medium with acoustic impedance value in between the piezoelectric layer and the loading is required. The research finding of DeSilets *et al.* has shown that the required value of matching follows the equations listed in Table 2.4 depending on the number of

matching layer⁵⁰. This calculation depends on the KLM model of suggested by Krimholtz, Leedom and Matthaei^{51,52}. The KLM model is shown in Figure 2.11. In this model, the capacitor and inductor are employed to connect with certain formats to represent an ultrasound transducer with a piezoelectric element, matching layer and backing layer. By assuming whole acoustic transmission line from the pUT to medium as an electrical circuit, the acoustic impedance of matching, including multiple layers, can be calculated.

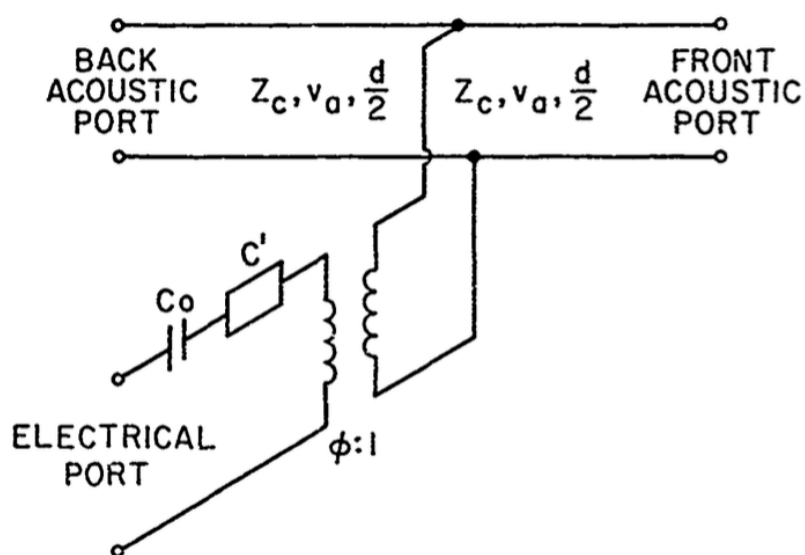


Figure 2.11 KLM model scheme⁵¹.

TABLE 2.4 THE REQUIRED ACOUSTIC IMPEDANCE OF DIFFERENT MATCHING COMBINATION.

	Z_1	Z_2	Z_3
Single matching layer	$Z_p^{1/3} Z_r^{2/3}$		
Double matching layer	$Z_p^{4/7} Z_r^{3/7}$	$Z_p^{1/7} Z_r^{6/7}$	
Triple matching layer	$Z_p^{11/15} Z_r^{4/15}$	$Z_p^{1/3} Z_r^{2/3}$	$Z_p^{1/15} Z_r^{14/15}$

The investigated result from Persson *et al.* group at 1985 shown in Figure 2.12 illustrates that both of the bandwidth and sensitivity of a pUT have been enhanced by using one quarter-wavelength matching layer⁵³. They also reported that bandwidth of the pUT can be further enhanced by using a double matching layer, but the sensitivity of pUT is not noticeably enhanced due to the total thickness increase of matching with higher attenuation. Theoretically the thickness of matching layer is quarter wavelength of the center frequency depending on the material's acoustic velocity. At this thickness, a constructive interference is complemented to minimize the acoustic energy loss passing through the matching. By controlling the thickness and acoustic impedance matching, the performance of pUT can be optimized.

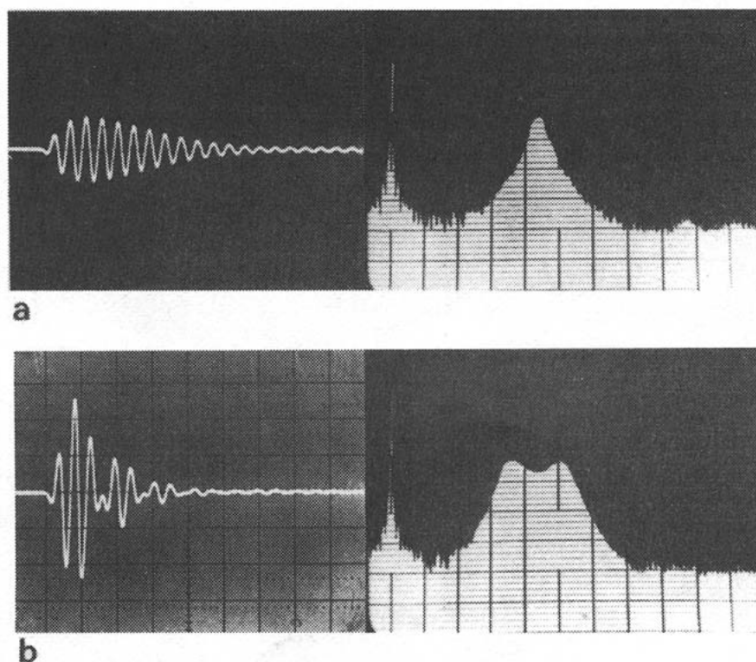


Figure 2.12 Pulse echo shape and frequency spectrum obtained in an experimental echo system using air backing transducers with (a) no front matching, and (b) one quarter-wavelength thickness matching layer $Z=6.0$ MRayl⁵³.

2.2.1.3 Backing layer

The backing layer produces a similar effect of matching but has an opposite purpose. Once the piezoelectric effect is triggered, vibrations in all resonance modes are triggered and emit acoustic wave at frequencies correlated to the dimension of sample. Along the axial direction pointing to the target, not only an acoustic pulse approaching to the target has been emitted, another acoustic pulse propagating in an anti-direction generated by the back surface is also emitted. The backside emitted acoustic pulse has an extremely strong reflection if the back surface of the piezoelectric layer is directly loaded on the medium due to the acoustic impedance mismatch. The strong reflected pulse superposes with the front emitted acoustic pulse and consequently produces a longer ring-down acoustic pulse. The ring-down extends the pulse length which decreases the axial resolution of the UT. Because of this, the backing layer with a high attenuation is required for absorbing the back emitted pulse wave. Thus, most of the backing is thicker than others layer to create a longer propagation path to enlarge the attenuation. The bandwidth of the acoustic pulse emitted by the transducer becomes boarder while the back emitted acoustic wave has been partially or fully absorbed. Figure 2.13 shows the investigation of Persson *et al.* in 1973⁵³. The pulse length of pUT can be reduced due to the ring-down suppression. The frequency spectrum is also enlarged with the increase of acoustic impedance.

Some of the backing contains a high roughness back surface to maximize the scattering at the back to prevent an axial reflection. Furthermore, some backing has a non-parallel back plane with the piezoelectric layer for enlarging the reflection times and propagation path of the back emitted acoustic pulse. However, a backing layer also possesses some drawbacks affecting the performance of the UT. A high density of backing is required to minimize the acoustic impedance difference between the medium for maximizing the

acoustic transmission rate from piezoelectric layer to backing. High acoustic impedance composite can be achieved by using a high-density material. Therefore, most of the backing layer consists high-density component to enlarge the back emitted wave absorption. By considering the mass spring model of acoustic wave propagation, a higher mass particle has a longer relaxation time in medium that produces a relatively higher attenuation coefficient at high frequency.

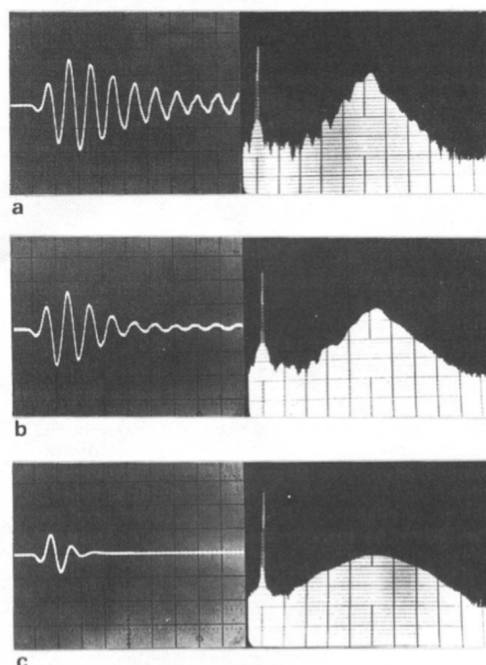


Figure 2.13 Pulse echo and frequency spectrum of pUT with (a) $Z=0.5$ MRayl, (b) $Z=5$ MRayl and (c) $Z=24$ MRayl backing layer⁵³.

In a short summary of performance of pUT, the compensation between the resolution and sensitivity of the pUT mainly depends on the purpose of pUT. For clinical imaging, a high sensitivity is more important than resolution because the organs are embedded in a deeper location which requires a stronger penetration. On the other hand, for research-based ultrasound imaging, mouse and rat are much smaller in size and feature than human so the image resolution is more critical than sensitivity. The compensation can be controlled

by the properties of active layer, matching layer and backing layer. An active layer contents high dielectric constant, piezoelectric constant and electromechanical coupling coefficient can theoretically enhance either resolution or sensitivity of the pUT. Besides, improving the acoustic properties of matching layer and backing layer appropriately can also help to accomplish a higher performance of the transducer.

2.2.2 Sensitivity of piezoelectric ultrasound transducer

The performance of the ultrasound transducer for biomedical imaging applications is determined by its sensitivity and resolution. The sensitivity is simply defined as the electro-acoustic transducer energy conversion efficiency. Sensitivity can be assumed as the ratio of an input amplitude to an output amplitude. For the ultrasound transducer applied on biomedical imaging, there is a network that converses amplitudes of voltage (V , I) and current at the electrical port to amplitude of force and velocity (F , v) at acoustic port. Since the transducer is used as both transmitter and receiver, the sensitivity is defined as the product of the transmission sensitivity and reception sensitivity. Normally, the logarithmic units of sensitivity can be described as⁵⁴:

$$S=20\log_{10}(V_{out}/V_{in}) \quad (3)$$

Where V_{in} is the applied electrical voltage for exciting the transducer and V_{out} is the voltage signal of the received transducer. In the case of ultrasound imaging, the receiving transducer is the same one as the transmission transducer. Therefore, the V_{out} becomes as the receiving voltage of the transmission transducer at the original position where receives the acoustic signal reflected by a reflector.

2.2.3 Resolution of piezoelectric ultrasound transducer

The spatial resolution of a 1-D array transducer is divided into two directions, which are the axial resolution and lateral resolution. Both resolutions describe the power of resolving two points of objects along one direction. The spatial resolutions of transducer in three different directions are shown in Figure 2.14⁵⁵.

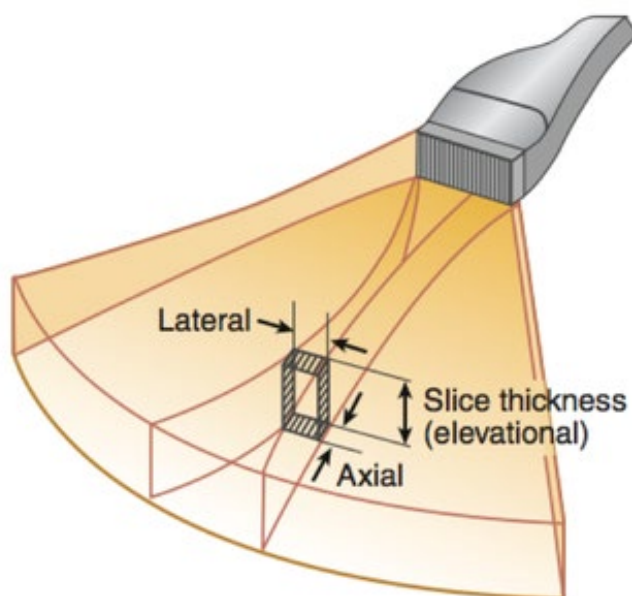


Figure 2.14 Resolution profile in 3-D imaging of array-transducer⁵⁵.

2.2.3.1 Axial resolution

The axial resolution is the resolution along the ultrasound pulse propagation direction, which is defined as $1/2$ of the pulse length. With a shorter pulse length, the echo reflected by the first object can be distinguished from the echo reflected by the adjacent object that is located deeper in the axial direction of the transducer. Then, the first and the second echoes can be identified as two distinct signals and displayed in the image after signal processing.

However, the pulse length is hard to define in the time domain, so the fast Fourier transform (FFT) is applied to transform the echo signal from the time domain to the frequency domain. In the frequency domain, the pulse length is represented by the -6 dB bandwidth of the spectrum. According to the below equation, -6 dB represents half output of the input value, meaning that the signal with the amplitude lower than half of the input is not counted in the pulse length.

$$dB = -20 \times \log(V_o / V_i) \quad (4)$$

With the FFT, the equation is listed as follows,

$$G(\omega) = \int_{-\infty}^{+\infty} g(t) e^{j\omega t} dt \quad (5)$$

A single acoustic pulse is seen to be a function $g(t)$ in the time domain combined by various sinusoidal waves with different periods t . $G(\omega)$ is the resultant component at a specific frequency, ω . By transferring each sinusoidal wave function from the time domain to the frequency domain, several discrete $G(\omega)$ are defined if the acoustic pulse repetition is short. In the usual excitation cases, the acoustic pulse repetition is far longer than the pulse length, thus, the function $G(\omega)$ becomes a continuous function. The width of the function in the frequency at -6 dB has an inversely proportional relationship with the acoustic pulse length. Therefore, the axial resolution of the transducer increases simultaneously with the -6 dB frequency bandwidth, consequently, it can be determined scientifically rather than calculating the pulse length in the time domain. The following equation presents the axial resolution in term of bandwidth:

$$R_{axial} = \frac{c}{2BW} \quad (6)$$

where c is the acoustic wave velocity in the medium and BW is the -6 dB frequency bandwidth of the transducer. Therefore, a high axial resolution (short pulse length) can be achieved by increasing the resonance frequency of pUT.

The frequency bandwidth is highly dependent on the resonance frequency of the pUT. The center frequency of the pUT is mainly depending on the thickness and acoustic velocity of the piezoelectric layer along the resonance mode direction. The relationship between thickness d and resonance frequency f can be defined as the following equation.

$$v/2 = N_f = f \times d \quad (7)$$

Where v is the acoustic velocity of the piezoelectric material and N_f is the frequency constant.

2.2.3.2 Lateral resolution

The lateral resolution is related to the beam width of transducer. With a narrower beam width, the resolution is increased because the adjacent objects can be determined. The beam width of the acoustic beam emitted by the transducer is defined as follows:

$$\text{Beamwidth} = \lambda L / D \quad (8)$$

In equation (8), for an unfocused transducer, λ is the wavelength of the acoustic pulse in the medium, L is the distance between the transducer and the target, D is the aperture size of the transducer. Figure 2.15 shows schematic diagrams of acoustic beams emitted by the unfocused and focused single-element transducer, respectively⁵⁵. It is shown that the unfocused acoustic beam is nearly parallel (equal beam width) within the near-field zone (also called Fresnel zone), and dispersed with a certain divergence angle to the infinite distance after the near-field zone. Thus, the lateral resolution of the unfocused transducer is almost the same within the near-field zone. The resolution is the highest at the near-field far-field transition point, but it drops gradually beyond the transition point along the axial direction of the transducer. On the other hand, the focused transducer has the narrowest beam width (and so the highest resolution) in the focal zone between the

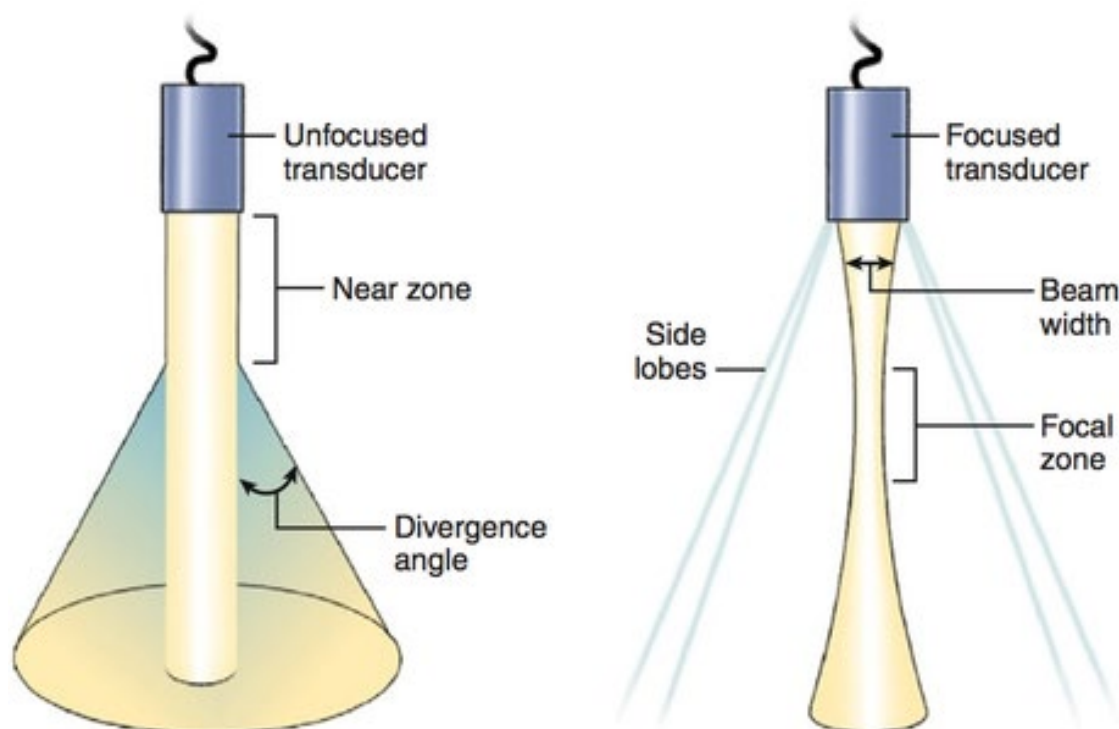


Figure 2.15 Ultrasound beam profiles of unfocused and focused single-element transducers⁵⁵.

near zone and far zone. Since the applicable range is narrow, the focused single-element transducers are not appropriate for medical imaging. The following Figure 2.16 shows the beam width of 1-D array transducer. The lateral resolution of array transducer depends on the main beam lobe angle θ and its equation is shown as follows:

$$\sin \theta = \text{lateral resolution}/L = \lambda/w \quad (9)$$

where L is the focal length of the beam. The equation is similar to the one of single element but the aperture size factor is replaced by the array total width. According to structure of array, the lateral resolution of it is also proportional to the element number, kerf widths and element widths.

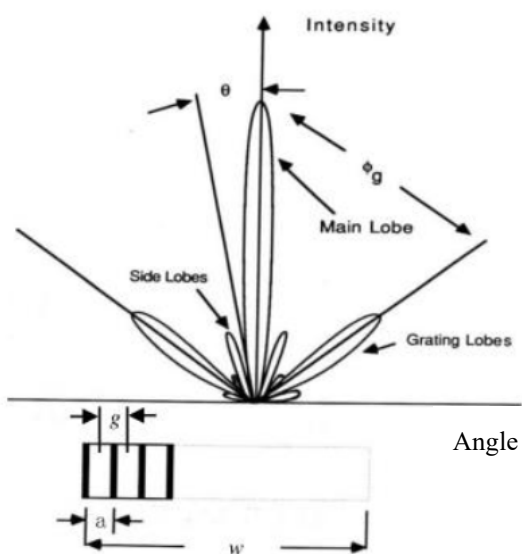


Figure 2.16 The beam profile of a 1-D array with simultaneous excitation (Top) and the dimension structure of the array (Bottom)⁵⁵.

CHAPTER 3

TUNABLE HIGH ACOUSTIC IMPEDANCE ALUMINA-EPOXY COMPOSITE MATCHING FOR HIGH FREQUENCY ULTRASOUND TRANSDUCER

3.1 INTRODUCTION

In recent decades, the investigations on pUT have been mainly focused on achieving high-quality image in clinic and research targeting at finer features. For these applications, the operation frequency of the ultrasound transducer is required to be as high as possible from 20 to 200 MHz^{39,56-64}. Other than enhancing center frequency, some ceramic based piezoelectric materials such as a polycrystalline PZT and single crystal PMN-0.28PT, which have high piezoelectric properties, have been widely used in the commercialized or research-based pUT in the last few decades^{5,23,26,36,39,65-81}. Although those materials have potential in enhancing the frequency bandwidth of the product, they have a relatively high acoustic impedance around 32 MRayl that increases the acoustic impedance mismatch between the piezoelectric element and human tissue. The acoustic impedance of human tissues and organs are shown in Table 2.3.

As shown in Table 2.4, the acoustic impedance values of the first matching layer in single, double and triple matching schemes are 4.2, 8.4 and 14.15 MRayl, respectively. The value of single matching is easy to achieve but the single matching layer has lower sensitivity and bandwidth compared to double and triple matching according to the investigation of Persson *et al.* in 1985 and T. Manh *et al.* in 2014^{53,82}. Figure 3.1 shows the investigated

result from Persson's group. The transducer with single quarter wavelength matching layer, 3.7 MRyals acoustic impedance, obviously shows a lower bandwidth than the one contents double quarter wavelength matching layers with acoustic impedance values of 2.1 MRayl and 6.1 MRayl. However, the amplitude of the double matching layer transducer only shows a slight enhancement. This unexpected lower amplitude enhancement is caused by the relatively thicker double matching. The thicker double matching layers result in a higher attenuation which compensates the enhanced signal benefited by the smoother acoustic impedance distribution.

Except the single matching layer, the required value of acoustic impedance of double and triple matching schemes are difficult to reach, especially the first layer of the triple-layer

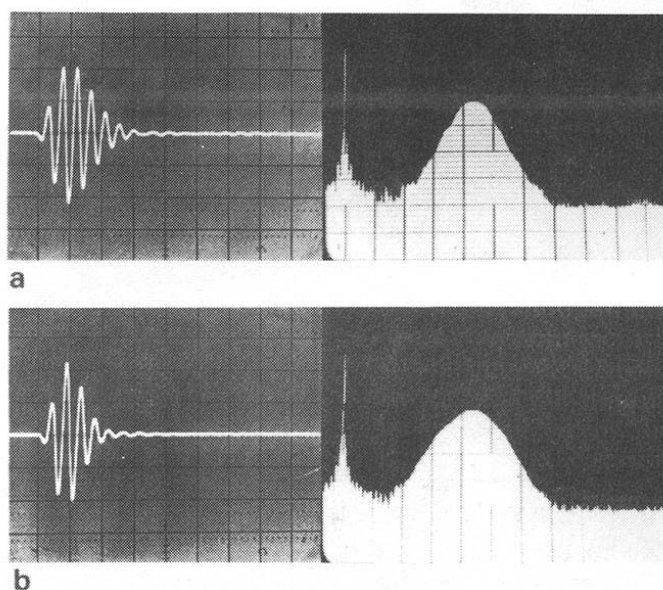


Figure 3.1 Acoustic response of the developed transducer with (a) one quarter wavelength matching layer and (b) double quarter wavelength matching layer⁵³.

matching since its acoustic impedance is too high to be achieved by traditional method. Traditionally, matching layer is made with centrifugal force to concentrate the 0-3 composite-like mixture of epoxy and other high acoustic impedance materials due to

liquid-like nature of the uncured mixture. However, the force supplied by centrifugal is far less than enough to enhance either the density or acoustic velocity, resulting in low acoustic impedance and cavities on the surface. Previous investigations have reported that matching layers composed of high-density metal and epoxy using traditional fabrication method can barely achieve the required high impedance. However, metal involved matching layers have a relatively higher attenuation, thus reducing the sensitivity and possibly the frequency bandwidth of the pUT^{83,84}.

Moreover, the matching layer fabricated by centrifugal method has a low uniformity due to the force gradient along radial axial of centrifugal. Recently, some reported findings have shown that matching layers containing oxide powders have impedances ranging from 2.8 MRayl to 10 MRayl using new-structured materials or new methods but they are either too complex for manufacturing or unsuitable for wide frequency range applications³¹⁻³⁵. For example, the fabrication method proposed by Manh *et al.* used photolithography plus etching or dicing and filling to pattern a pure silicon with filled epoxy in the gaps, i.e. a silicon-epoxy 2-2 composite matching. Figure 3.2 shows the fabrication process flow and a photo of the product⁸². Photolithography and etching are complex processes requiring high precision machine and ambient condition control which is extremely high cost compared to traditional fabrication method. Besides, there is a large acoustic impedance difference between theoretically modeled result and the experimental result, meaning that the acoustic impedance using this method is hard to be estimated and controlled. Such that, a high acoustic reflection may still be obtained in those parts resulting in an overall low sensitivity.

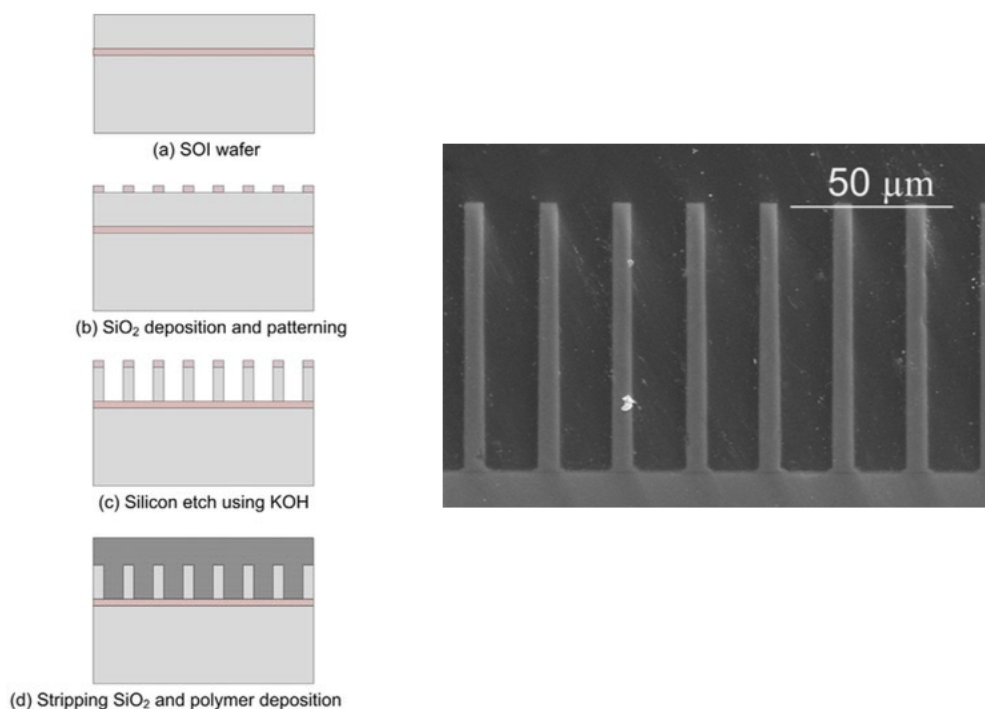


Figure 3.2 (Left) the process flow of the silicon-epoxy 2-2 composite fabrication method. (Right) The cross-section SEM image of the fabricated 2-2 composite⁸².

Therefore, it has been a critical problem bothering the pUT research field for decades to develop a suitable matching to further enhance the performance of pUT with high performance piezoelectric ceramic-based materials. A matching layer fabrication method that can accomplish high acoustic impedance and simultaneously low-cost is desired for multiple matching layer scheme. In this chapter, a method using a high-pressure compression method is demonstrated and investigated for enhancing and manipulating the density and acoustic longitudinal velocity. This method possesses the advantages of low cost and is easy for manufacturing. More importantly, the acoustic impedance of the alumina epoxy matching has been enhanced to maximum 9.50 MRayl which is much higher than the traditional fabrication methods. Thus, the developed matching is suitable for pUT with high acoustic impedance piezoelectric active layer.

3.2 FABRICATION AND CHARACTERIZATION

3.2.1 *Matching Layer Fabrication*

In the preparation of the compressed matching layer, alumina powder with 1-2 μm particle size (Buehler, U.S.A.) required a treatment before the mixing process. The powder was heated up to 1200 degree Celsius for 2 hours for changing its structure to α phase in a furnace (KF1700-I, Nonjing Boyuntong Instrument, China) with a 5 $^{\circ}\text{C}/\text{mins}$ heating rate due to the α -phase aluminum oxide has a relatively higher longitudinal acoustic velocity than other phases. Variant weight ratio of the powder was then mixed with the epoxy (Insulcast 502, ITW Insulcast, U.S.A). The mixture was continuously agitated for 30 minutes in an agate mortar to accomplish a more uniform distribution of aluminum oxide. This agitate time was set as close as the epoxy's pot life which obtained a double epoxy viscosity before compressing. More aluminum oxide is squeezed along with the epoxy if the mixture has low viscosity. More extrudate of aluminum oxide reduces its concentration in the matrix leading to reduced acoustic impedance of the produced matching layer. Thus, it is critical to minimize the extrudate of aluminum oxide powder during the compression.

The mixture was placed into a 4 cm-diameter circular compartment of a customized stainless-steel mold. Two stainless steel circular rods with same diameter located on the top and the bottom of the compartment was compressed by a hydraulic press as shown in Figure 3.3. To further increase the concentration of the alumina powder, a 4-hour prepress pressure of 7.8 MPa was applied to squeeze out the exceeded epoxy. A high compressing pressure was continuously added to the mold maintained for 12 hours at room temperature preventing a relaxation of the epoxy during curing process. The pressure would drop after 12 hours compression due to the fact that epoxy was further squeezed out. The curing

time of the epoxy would be longer than normal caused by the applied external pressure. According to this, a recompression process was employed to raise the pressure back to the original compression pressure for another 3 hours. Afterward, a final curing process was carried out by placing the mixture released from pressure in an oven for 12 hours at 65 °C. Figure 3.3(a) and (b) show the setup during compression and the profile of the compressed matching layer.



Figure 3.3 The picture of matching layer under an 8 tons weight in a custom designed mold (Left) and the cured matching layer after the compression (Right).

The compression pressure was controlled by an applied weight which has a range from 39.0 MPa to 85.8 MPa with a 7.8 MPa step. Simultaneously, the ratio factor of the aluminum oxide and epoxy was trailed from 1:1 to 4:1. The acoustic properties, including longitudinal velocity, density and attenuation, were estimated after the curing process.

3.2.2 Acoustic impedance characterization

The acoustic impedance Z of the matching layer is calculated by multiply its longitudinal velocity v and density ρ as the following equation:

$$Z = v\rho \quad (10)$$

Therefore, both the velocity and density will be measured as shown as follows.

3.2.2.1 Acoustic Velocity

In the longitudinal velocity measurement, samples were clamped by two 4-MHz ultrasound transducers with identically acoustic performance. A pulser/receiver (Panametrics 5900PR, Olympus) in transmission mode was connected with one of the transducers for emitting an acoustic pulse. The execution electrical signal energy was 1 μ J within a frequency range from 1 kHz to 20 MHz. The emitted acoustic pulse was passed through with and without the sample and received by another transducer whose surface was aligned perfectly to the emitting transducer. An acoustic jell with water like acoustic attenuation was filled in all interfaces along the acoustic propagation path for preventing the energy loss caused by the air gas. The received signal was returned back to pulser/receiver through the receiver port. A digital oscilloscope (HP Infinium DSO-S 204A, Keysight Technologies, U.S.A.) with 50 Ohms electrical coupling mode was connected to the pulser/receiver for obtaining both emission and transmission pulses. The photo of this setup is shown in Figure 3.4.

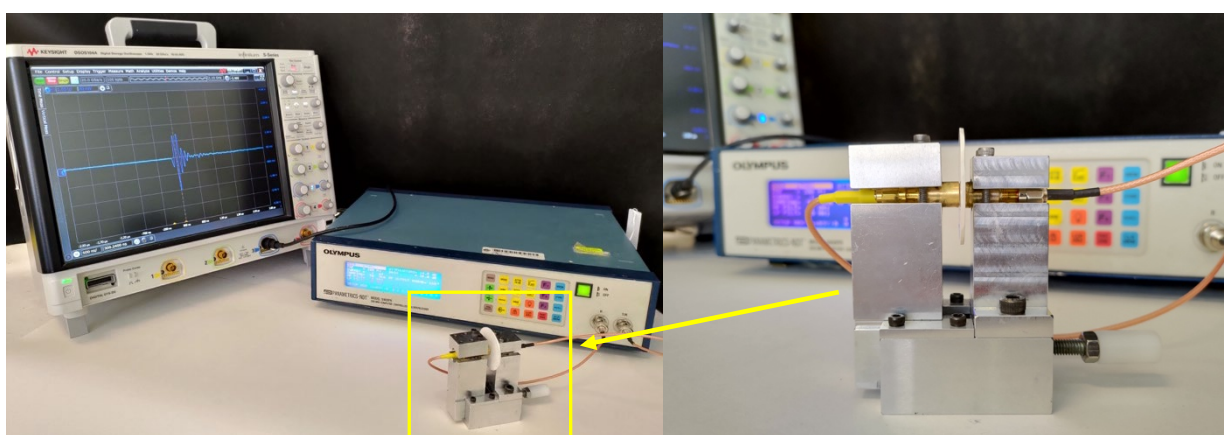


Figure 3.4 The setup (Left) and the fixture (Right) of the measurement of acoustic velocity and attenuation.

The measurement has two main steps. First, the propagation time (t_0) of acoustic pulse without the specimen was measured by connecting both transducers' head-by-head. The time was simply displayed on the oscilloscope. Second, the propagation time (t_s) with the specimen was measured. The time delay of acoustic wave passing through the matching was measured and the longitudinal velocity v can be calculated by the following equation:

$$v=d/\Delta t \quad (11)$$

Where d is the thickness of the tested matching layer and Δt is the time delay which is the time difference between t_0 and t_s .

The acoustic wave also has a shear wave that moving the medium particle perpendicular to its wave propagation direction. Unlike longitudinal wave, shear wave is hard to propagate through medium without a strong shear strength such as water. Its needs a medium which is rigid enough for propagation.

Although the shear wave is not a desired signal in most of the array transducers, it can still propagate through the medium along lateral and longitudinal directions and affect the signal of the UT. For the shear velocity measurement, a shear acoustic transducer was used. The measurement method is similar to the previous one. The pulse/receiver or the signal generator excites the shear wave such that a shear acoustic pulse propagates along the axial direction of the transducer. The specimen was clamped between the transducer and a 5-mm thick quartz. The propagated pulse and the pulse reflected by different interfaces were displayed by the oscilloscope connected with the transducer. The maximum amplitude of the reflected pulse was obtained by rotating the transducer along the normal direction. The time difference of two pulses reflected by different interfaces was measured by the oscilloscope. Using the following equation, the shear velocity of the specimen is calculated as:

$$v_{shear} = 2d/t \quad (12)$$

where t is the time difference and d is the thickness of the specimen. Using equation (12), the acoustic impedance of piezoelectric material, matching layer and backing layer can be calculated.

3.2.2.2 Density

The density of the matching layer was measured by using the Archimedes' principle. The weights of the specimen in air and immersed in water were measured by an electrical balance, respectively. With the following equation, the density of the specimen can be determined as:

$$\rho_{specimen} = \rho_{water} \cdot (m_{air} / m_{water}) \quad (13)$$

where ρ_{water} is the density of water ($\approx 1000 \text{ kg/m}^3$), m_{air} and m_{water} are the masses of specimen in air and in water, respectively. This measurement is limited by the density of the specimen that should be higher than that of water, and the specimen that should not exhibit strong water absorption effect. For the specimen not fulfilling the requirements, the fluid should be changed, and the density of water should be replaced by the density of that fluid in Equation (13).

3.2.3 Acoustic attenuation characterization

The attenuation characterization was also carried out. Both surfaces of the matching layer were polished by 1200 grid sandpaper for standardizing the surface roughness to eliminate acoustic power variant caused by an uneven reflection. This is important since the attenuation is not only affected by the absorption and scattering inside the matching but also the reflection both macroscopically and microscopically at every interface along

the acoustic propagation. If the matching layer has a uniform acoustic impedance, the macroscopic reflection of the matching layer is mainly due to the surface roughness rather than the material nature. The transmission amplitude matching layer V_0 at thickness d_0 then was measured using the previously setup in acoustic velocity part. The thickness of the matching layer was lapped to half of the original thickness and the surface was polished. The transmission amplitude after lapping V_l was measured again and the attenuation at 10 MHz frequency can be calculated by the equation shown as follows:

$$\text{Attenuation (dB/mm)} = 20 \log(V_l/V_0) / (d_l - d_0) \quad (14)$$

Where V_0 and V_l are the transmission acoustic amplitudes before and after the lapping, respectively. The d_0 and d_l are the thicknesses of the matching layer before and after the lapping, respectively.

3.2.4 Acoustic response of transducers

3.2.4.1 Pulse echo response and frequency spectrum

The pulse-echo response of the transducer was measured in a water tank at room temperature. A Panametrics 5900PR pulser/receiver was connected to the UT and excited the UT using an 1 μ J energy electrical impulse with 50 Ω damping at 500 Hz repetition. The echo was reflected by a thick (~37 mm) stainless steel target at a distance of the near field-far field (nf-ff) transition point. The nf-ff distance of a square shape element was calculated using the following equation:

$$N = A / \pi \lambda \quad (15)$$

Where A is the aperture of the element and λ is the wavelength of the acoustic pulse in the medium. The reflected signal was received through the same path as the excitation.

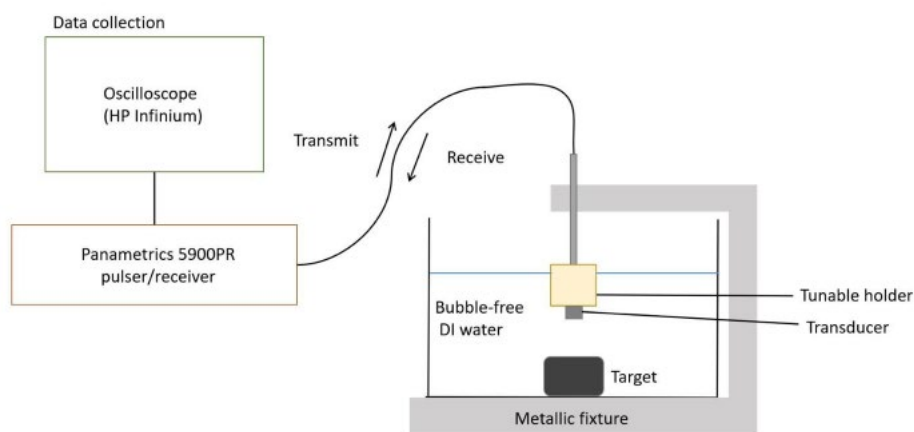
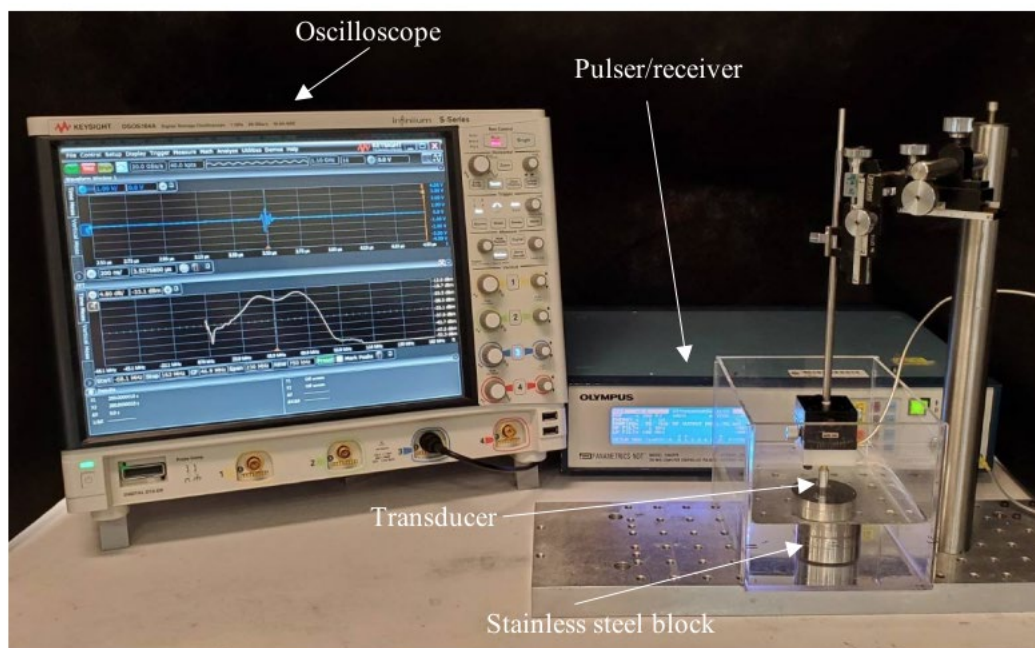


Figure 3.5 The setup of two-way impulse measurement (Top) and its schematic diagram (Bottom).

A 26 dB gain was added to the received signal and further transmitted to an oscilloscope (HP Infinium DSO-S 204A, Keysight Technologies Inc., Santa Rosa, CA). The time domain echo response was displayed simultaneously with frequency spectrum in-situ calculated by the fast Fourier transformation (FFT) mathematic program of the oscilloscope. Figure 3.5 shows the measurement setup of two-way acoustic response measurement. Two -6 dB points in the frequency spectrum were found at the -6 dB

difference from the maximum amplitude. The equation of bandwidth calculation is shown as follows^{3,26,27}:

$$\text{-6 dB bandwidth} = 2(f_H - f_L) / (f_H + f_L) \quad (16)$$

where f_H and f_L are the frequencies of the -6 dB points.

3.2.4.2 Insertion loss

The insertion loss (IL) measurement setup is same as Figure 3.5. The transducer was excited by a signal generator (AFG3251, Tektronix, Beaverton, U.S.A). The excitation waveform is a sinusoidal wave with an amplitude V_i and a frequency of the center frequency in a tone burst mode. The pulse propagated through the water and reflected by the interface between water and stainless steel. The amplitude (V_o) of the reflected pulse was obtained by the transducer and displayed on the oscilloscope connected with the signal generator and the transducer simultaneously. The impedance of the oscilloscope was set as $1\text{M}\Omega$ for V_o measurement and $50\ \Omega$ for V_i measurement. The following equation shows the calculation of IL :

$$IL = -20 \times \log(V_o/V_i) \quad (17)$$

3.3 RESULTS

3.3.1 *Applied pressure variant*

In the first part, the weight ratio of aluminum oxide to epoxy is fixed at 2:1. The applied pressure varies in a range from 39.0 MPa to 85.8 MPa with a 7.8 MPa step. All the developed specimens before characterization have been lapped down to a 2 mm thickness. Each condition in the result has sampled multiple specimens developed individually for

achieving a repeatable and precise result. The measured longitudinal velocity of each step is shown in Figure 3.6 (a). The dot represents the mean of specimens' set and the error bar represents the maximum to minimum range of the specimens set. In this graph, the result shows a velocity enhancement from 3376 ms^{-1} to maximum value 3652 ms^{-1} along with applied pressure from 39.0 MPa to 62.4 MPa, respectively. When applied pressure beyond 62.4 MPa, the acoustic velocity suddenly drops to 3380 ms^{-1} . The velocity value is maintained at around 3380 ms^{-1} with 20 ms^{-1} variation within the applied weight range from 70.3 MPa to 85.8 MPa. The measurement data only has a maximum 2.9% error which shows that the matching layer developed by this method has a high consistency and reliability. The relationship of density and applied weight of the matching material is illustrated in Figure 3.6(a), where it is apparent that the density of matching layer with fixed 2:1 aluminum oxide to epoxy weight ratio shows an enhancement from 2366 kg/m^3 to maximum value 2399 kg/m^3 when the applied pressure increases from 39.0 MPa to 54.6 MPa. However, the density shows a decrease when the applied weight exceeded 54.6 MPa. In the measurement, a maximum error of 2.1% has been obtained at 39.0 MPa and the rest of the measurement data shows an error lower than 1.4% error.

In Figure 3.6 (b), the relationship of acoustic impedance and applied pressure shows a similar trend as the velocity one, while the minimum value of velocity is already 1.4 times than the maximum value of density, and the dynamic range of velocity is much higher than the density. This explains why the impedance behavior is dominated by the velocity. The value increases from 7.99 MRayl to maximum 8.51 MRayl along with the applied pressure increased from 39.0 MPa to 62.4 MPa. The impedance drops to 7.81 MRayl immediately once the applied pressure increases to 70.2 MPa.

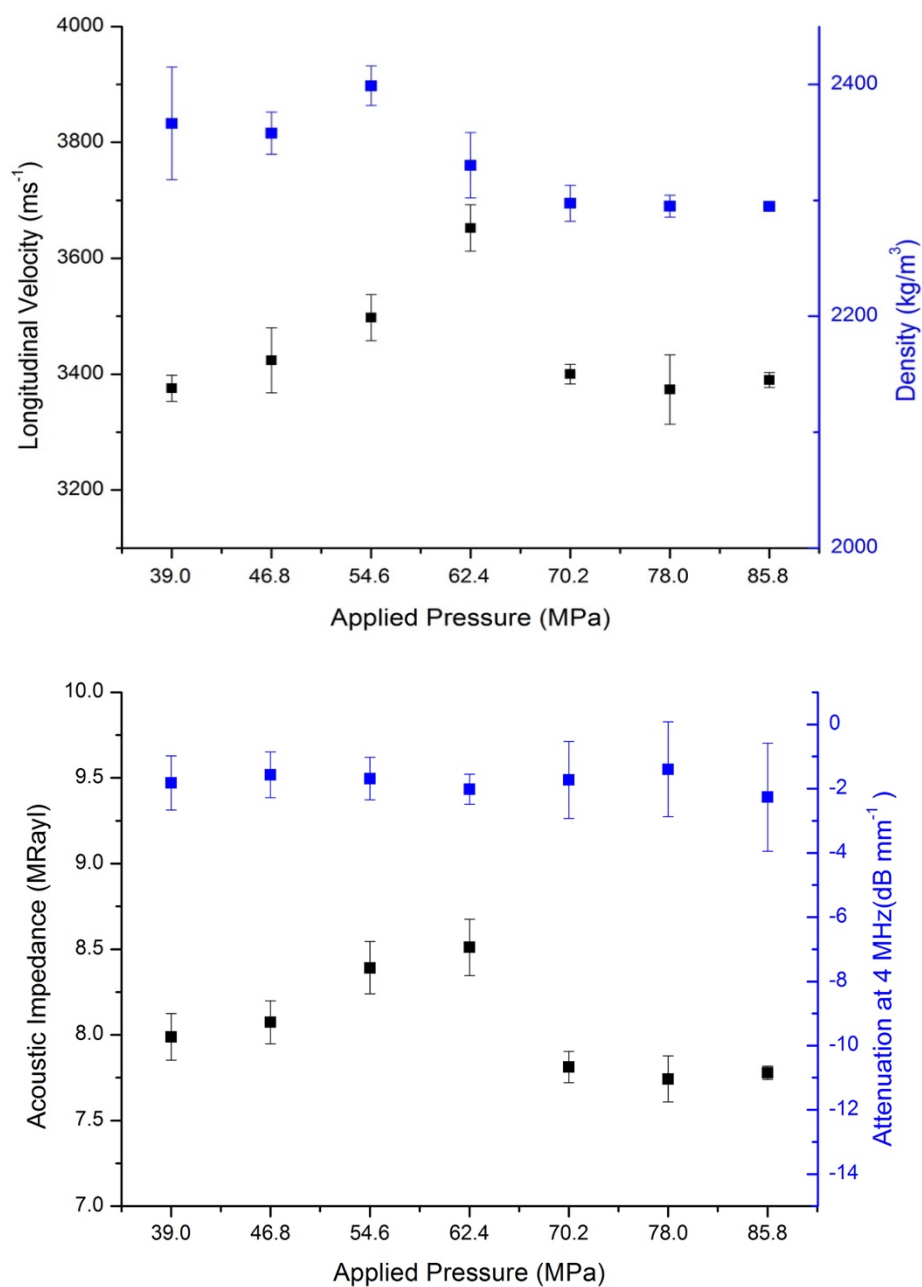


Figure 3.6 a) The graph of acoustic longitudinal velocity (Black) and density (Blue) versus applied weight and b) the relationship between applied weight and acoustic impedance (Black) or attenuation at 4 MHz (Blue) at a fixed 2:1 aluminum oxide powder to epoxy ratio.

The measured attenuation of all the developed matching layers with fixed 2:1 aluminum oxide powder to epoxy ratio are illustrated in Figure 3.6(b). The attenuation values in all

applied weights are almost constant with only a slight variation between -1.40 dB/mm to -2.27 dB/mm at 4 MHz frequency. According to the equation shown below, the measured average frequency has a power ratio $\eta = 0.9$.

$$\text{Attenuation} = \alpha_0 \omega^\eta (\Delta x) \quad (18)$$

Where the α_0 is the attenuation coefficient, ω the frequency, and Δx the propagation distance. The calculated maximum and minimum attenuations of the matching layer at 40 MHz are -11.12 dB/mm and -18.03 dB/mm, respectively. At the pressure point that obtains the maximum acoustic impedance in this development method, the attenuations are -2.08 dB/mm at 4 MHz and -16.5 dB/mm at 40 MHz, respectively. This value is compatible to previous research finding from other investigators using the same ceramic material which has shown a minimum -15 dB/mm attenuation at 40 MHz^{30,85}. The acoustic impedance using this developed method is much higher than those reported results. Concluding the measured results above, the 8 tons applied weight is the best parameter in this method to produce a matching layer that has the highest acoustic impedance and compositely low attenuation for ferroelectric materials that has high acoustic impedance.

3.3.2 Powder concentration variant

According to our hypothesis mentioned above in the fabrication section, concentration of the component which contents a higher acoustic velocity and density determinates the maximum achievable acoustic properties of product ultimately. Instead of the applying pressure to enhance the concentration of the aluminum oxide, the mixing weight ratio is also a factor that can further enhance its concentration in the matching pushing the acoustic properties as close as to the raw aluminum oxide. Thus, the affection of

aluminum oxide's weight ratio in the mixture has been investigated and the acoustic property of the produce is illustrated in the following Figure 3.7(a) and (b).

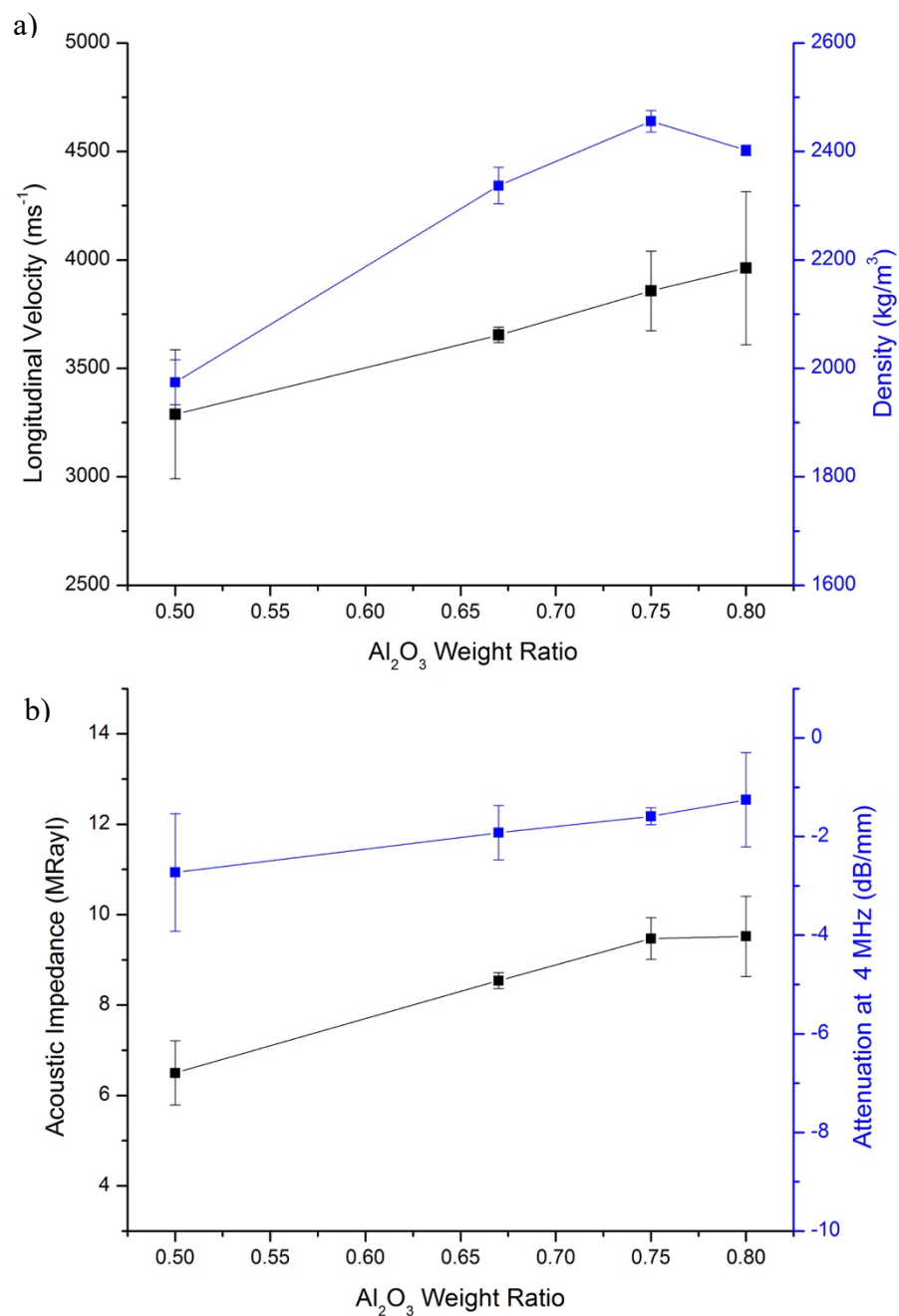


Figure 3.7 a) The longitudinal velocity (Black) and density (Blue) versus the weight ratio of aluminum oxide and b) the acoustic impedance calculated by the measured results (Black) and the attenuation versus the weight ratio of aluminum oxide.

In Figure 3.7(a), the longitudinal velocity shows an almost linear properties from 3288 ms⁻¹ to 3961 ms⁻¹ at aluminum oxide to epoxy ratio from 1:1 to 4:1. The measured density illustrates an increment from 1974 kg/m³ to a maximum 2456 kg/m³ in a weight ratio from 1:1 to 3:1. The density lightly dropped down to 2402 kg/m³ while the weight ratio was raised up to 4:1. The acoustic impedance of the matching shown in Figure 3.7(b) is a nearly linear enhancement from value 6.50 to 9.47 MRayl along with the aluminum oxide to epoxy weight ratio increased from ratio 1:1 to 3:1. However, due to the density of the matching dropped at 4:1 weight ratio, the impedance of matching shows a saturation with a maximum value 9.52 MRayl after the ratio reached 3:1 although the velocity value at ratio 4:1 is higher than the one at 3:1.

3.3.3 Microscopic structure

The matching layer not only has excellent acoustic properties but also a high uniformity microscopically. The following SEM pictures in Figure 3.8 show the macro and microscopy structure of the matching layer developed by the high compression pressure method. SEM images of matching layers containing same metal component developed by centrifuge method, which is one of the most common and traditional matching layer development method, are shown in Figure 3.8(a), (b), (d) and (e) for comparison. Figure 3.8(a), (b) and (c) show the surface structure of matching layer developed by high compression method with alumina, centrifuge method with alumina and centrifuge method with silver, respectively. In Figure 3.8(a) and (b), the matching layers developed by centrifuge method have cavities on the polished surface. The cavities have diameter around from minimum 10 μm to maximum 100 μm.

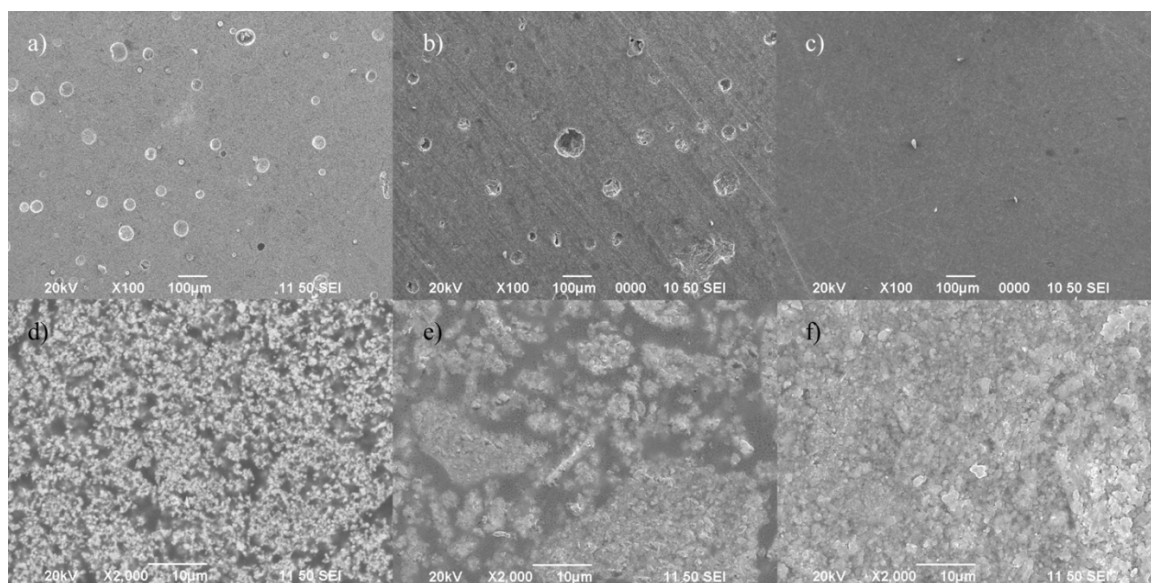


Figure 3.8 (a), (b) and (c) The scanning electron microscopy image of matching layers developed by centrifuge method with silver powder, centrifuge method with aluminum oxide and high pressure compression method with alumina, respectively, at 100X magnification. (d), (e) and (f) at 2000X magnification.

TABLE 3.1 THE SPECIFICATIONS OF THE HIGH FREQUENCY SINGLE ELEMENT TRANSDUCER.

Designed center frequency	55 MHz
Elements width	1.5 mm
Elements length	1.5 mm
PZT thickness	33 μm
Compressed Al_2O_3 epoxy mixture thickness	18 μm
Parylene thickness	9 μm
Backing layer thickness	5 mm

The performance of the matching layer has been demonstrated on a high frequency ultrasound transducer in the following section. The specification of the transducer with a double matching layer design is optimized by a Krimholtz, Leedom and Matthaef (KLM) based simulation software PiezoCAD (Sonic Concepts, Woodinville, WA). The specifications and acoustic properties of the transducer have been listed in the Table

3.1 and Table 3.2, respectively. The transducer is using a PZT (PIC151, PI Ceramic, Germany) as the piezoelectric layer.

According to the acoustic impedance of the PZT and the calculation listed in Table 2.4, the first matching layer and second matching layer are set as 9.49 MRayl and 2.59 MRayl, respectively. The 62.4 MPa compressed alumina-epoxy composite with 3:1 weight ratio and the parylene C are chosen as the first and second matching layer, respectively. Backing layer is a pure epoxy EPO-TE 301-1 which has almost 3.00 MRayl acoustic impedance. Instead of using a heavy backing, a light backing can reduce the clamping effect at high frequency, thus the frequency reduction of the transducer would be lower. All the factors were imported to a simulation programme PiezoCAD based on KLM model, so the optimized thickness of each layer can be determined. Considering the clamping effect of ultrasound transducer at high frequency, the simulated center frequency was set as 60 MHz in the programme to implement a 55 MHz transducer realistically. The optimized thickness of all layers including the piezoelectric layer are showing the in Table 3.2.

TABLE 3.2 THE OPTIMIZED SPECIFICATION OF EACH LAYER OF THE DEVELOPED TRANSDUCER.

	Piezoelectric Layer	First matching	Second Matching	Backing layer
Material	PZT	High pressure compressed Al ₂ O ₃ powder + Epoxy 502	Parylene C	EPO-TEK 301-1
Weight ratio	N/A	3:1 at 62.4 MPa	N/A	N/A
Acoustic impedance (MRayl)	38.82	9.47	2.59	3.00
Velocity (ms⁻¹)	4967	3857	2350	2650
Density (kgm⁻³)	7816	2456	1100	1132
Thickness (mm)	0.033	0.018	0.009	5

According to Table 3.2, the thicknesses of both first and second matching layers is not the exact quarter wavelength value but really close to that value. The simulated thicknesses of the PZT, the first matching layer and the second matching layer are 33, 18 and 9 μm , respectively. In the fabrication process, the PZT was lapped to the required thickness, and a Cr/Au electrode with 95 nm total thickness was deposited on the PZT's surface by magnetron sputtering. Subsequently, an aluminium housing was bounded around the PZT and an EPO-TEK 301-1 was filled in the housing as a backing layer and a mounting medium. A SMA connector was installed on the transducer and a line electrode was deposited on the front surface of the transducer to produce an electrical connection between the PZT and housing. Finally, a lapped 15 μm -thick high compressed alumina epoxy composited matching was attached on the front surface of the transducer using epoxy M-Bond 610 (Micro-Measurements, Raleigh, U.S.A). A fixture was



Figure 3.9 The picture of the single element ultrasound transducer attached with the high pressure compressed matching layer.

employed for clamping the matching layer attached to the transducer during epoxy curing. This made the epoxy layer as thin as possible. The epoxy was cured in an oven at 65 °C under atmospheric pressure for 24 hours. Finally, a thin layer of parylene C was deposited on the transducer using a parylene deposition system (SCS PDS2010E LABCOTER, Specialty Coating System, Inc., USA).

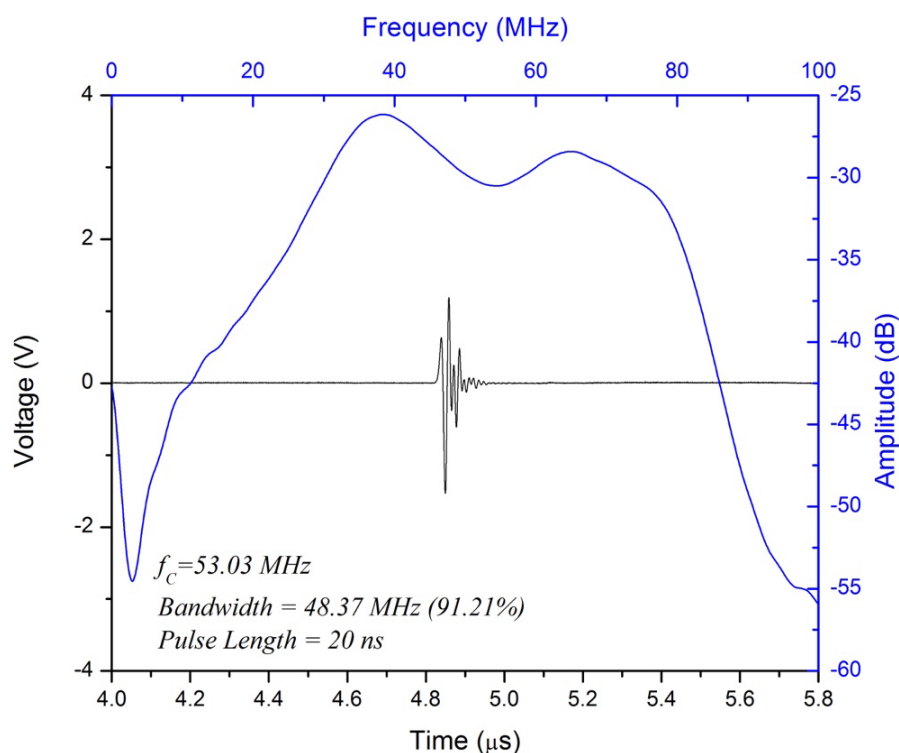


Figure 3.10 The obtained acoustic response of the transducer casted the matching layer fabricated by high pressure compression method (Black) and its frequency spectrum (Blue).

The developed transducer is shown in Figure 3.9. The two-way impulse acoustic response in water of the representative transducer is shown in Figure 3.10. The center frequency of the measured acoustic pulse reflected by a stainless-steel board at near-field far-field transition point is 53.03 MHz. The -6 dB bandwidth shown in the frequency spectrum is around 48.37 MHz which is 91.21%. Besides, the insertion loss is -36.66 dB, and the

measured -6 dB pulse length is 20 ns. The emission pulse of pulser/receiver in this measurement is 1 μ J energy. The peak-to-peak amplitude of the received pulse with a 26 dB gain is 2.72 V. In this demonstration, 5 individually developed transducers using the same specification have been developed. All the measured results are shown in Table 3.3. The results show a high consistence. All the transducers with the matching layer developed by the high-pressure compression method show an ultra-wide bandwidth according to its center frequency. However, for achieving a massive wide bandwidth, the signal amplitude has to be sacrificed due to the large back reflected wave absorption. Fortunately, the signal to noise ratio of this developed transducer is high thus the signal can be amplified massively to produce a high amplitude signal.

TABLE 3.3 MEASURED ACOUSTIC RESPONSES OF TRANSDUCERS ATTACHED WITH ALUMINA EPOXY COMPOSITE MATCHING LAYER UNDER HIGH COMPRESSION PRESSURE AT 62.4 MPa AND 3:1 WEIGHT RATIO.

	Center (MHz)	Frequency (MHz)	Bandwidth (MHz)	Bandwidth (%)	Insertion Loss (dB)
Representative					
Transducer	53.03		48.37	91.21	-36.66
Transducer-2	52.90		45.08	85.22	-36.27
Transducer-3	52.67		46.45	88.19	-34.11
Transducer-4	49.70		44.13	88.79	-33.25
Transducer-5	51.29		44.00	85.79	-33.55

3.4 DISCUSSIONS

3.4.1 Pressure Variant

In Figure 3.6, the behavior of density is incoherent to the one of longitudinal velocity. The applied pressure for obtaining maximum value in density shifts to 54.6 MPa instead of 62.4 MPa in the velocity. This phenomenon is unmated to the expectation that both of

the velocity and density should react coherently to the applied pressure in this development method. Besides, the gradient of increment in density has a much lower value than the velocity, consequently, lower the dynamic range of the value from the applied variable from 39.0 MPa to 85.8 MPa. This suggests a non-linear relationship of the sound velocity and the density of alumina, and it could be process history dependent. The similarity between two measurements is that the values illustrate a saturation while the applied pressure reaches 70.2 MPa. However, the density of a matching layer is not as important as velocity because it only varies the acoustic impedance value of matching layer but velocity also controls the thickness of the matching as well as the fabrication difficulty, thickness tolerance and the attenuation of the matching. Thus, the unexpected behavior of density has a limited effect to this investigation that can be ignored.

The increase of longitudinal velocity is possibly caused by the correlation effect of the composite while most of the surface of aluminum oxide powders in the composite are basically connected by applying a high compression pressure from 39.0 MPa to 62.4 MPa. This made the acoustic signal propagated through the connected surface of powder has a velocity as fast as the aluminum oxide as single crystal structure. The enhancement of the density within this pressure range is an evidence to proof that the distance between the aluminum oxide is narrowed in the composite. For pressure higher than 62.4 MPa, the compression force stored a high potential energy in the composite. Simultaneously, the viscosity of the epoxy is not high enough to against the stored potential energy within the normal curing time given by the manufacturer due to the high pressure extends the curing time of the epoxy. Thus, the composite exhibits a rebound while the applied pressure has been removed after curing, furthermore, this rebound has been held by the final baking curing. This rebound causes the decrease of density and velocity of the alumina composite

which explains the trend of density as a function of pressure as shown in Figure 3.6(a) which has a similar trend to sound speed while pressure exceeds 62.4 MPa.

3.4.2 Powder concentration variant

According to results of pressure variant measurement, it can be expected that both of the density and velocity should increase beside with the aluminum oxide concentration enhancement. The most possible explanation of the density drop is due to the fact that the epoxy at this high weight ratio is no longer enough to form composite to all aluminum oxide particle in the developed matching. Thus, the matching layer developed at this ratio in fact suffers from peeling off of alumina powder from the edge even though the matching layer is fully cured. However, the affected zone only appears at around 1 mm width at the edge. The inner part of the developed piece still performs a solid state that formed a composite with the epoxy. A -2.73 dB/mm attenuation is obtained at 1:1 weight ratio and reduced to -1.26 dB/mm at 4:1 weight ratio. According to the results listed in this section, the 4:1 aluminum oxide powder to epoxy weight ratio under 62.4 MPa applied compression pressure combination is the best parameter in this new matching layer fabrication method that produced a highest acoustic impedance value and lowest attenuation simultaneously.

The matching fabricated by this high compression pressure method shows excellent acoustic properties by comparing with other fabrication method in previous reported investigation. Table 3.4 lists the comparison, where the matching layer developed by the high compression method has a significantly higher acoustic impedance than other reported alumina/epoxy matching using other methods. The only reported matching layer has comparable acoustic impedance to our method are using extremely high-density metal

component of tungsten³⁰. However, its attenuation is -25 dB/mm at 30 MHz which is remarkable higher than the matching layer develop by our high compression method. The matching layer developed in this thesis work even has a higher acoustic impedance than

TABLE 3.4 THE ACOUSTIC PROPERTIES OF MATCHING LAYER DEVELOPED BY MUTILPUTE METHOD FROM PERVIOUS REPORTED ARTICLES.

	Longitudinal velocity(ms⁻¹)	Density(kg/m³)	Acoustic Impedance (MRayl)	Attenuation (dB/mm)
Al₂O₃ + Insulcast 502 (0.80 Weight ration compressed under 62.4 MPa)	3961	2402	9.52	-10.0 (at 40 MHz)
Al₂O₃ + EPO-TEK 301⁸⁶	3200	1630	5.22	-15.0 (at 40 MHz)
Al₂O₃ + Insulcast 502 (Centrifuge at 62.8 MPa/kg)	2803	1812	5.19	-16.6 (at 40 MHz)
Tungsten + EPO-TEK 301³⁰	~1680	~5654	~9.50	~ -25.0 (at 30 MHz)
Silver + Insulcast 502 (Centrifuge at 62.8 MPa/kg)	1936	3192	6.18	- 38.4 (at 40 MHz)
Al₂O₃ + EPO-TEK 301³⁰	~2868	~1980	~5.68	-12.6 (at 30 MHz)
Silicon polymer 2-2 composite (Chemical Etched)^{34,82}	5818	1349	7.85	Not addressed
Silicon polymer 1-3 composite(Chemical Etched)³⁵	4730	1335	6.31	-1.72 (only in Silicon at 40 MHz)

matching reported by Manh *et al.* using a ceramic material, silicon, which has higher acoustic impedance than aluminum oxide in bulk format^{34,35,82}. This matching layer developed by this high compression method illustrate a great performance although the

original properties of the composited material is lower than others. According to this, the performance of matching can be further enhanced if the component is replaced by silicon or high density metals, therefore, this enhanced value may fulfill the requirement of the first matching in triple matching structure.

3.4.3 Microscopic structure

The generation of cavities shown in Figure 3.8 (a) and (b) are possibly due to the air bubble generated by the stirring while mixing the epoxy and the powder. Theoretically, the air bubble should be removed during the centrifuge due to the density of it is significantly lower than other components in the mixture. However, the bubbles still remained because of the mixture viscosity is too high that the centripetal force is not enough to against the viscosity for isolating the bubble from the mixture. The cavities contents air which has extremely low acoustic impedance and high attenuation. The acoustic wave may be reflected or attenuated while penetrating the matching. This may reduce the sensitivity and frequency bandwidth of the developed transducer. On the other hand, in Figure 3.8(c), the matching layer using the high-pressure compression method does not appear any cavity on the polished surface. The compression method applied a remarkable higher force than the centrifuge method, more importantly, higher than the viscosity although the aluminum oxide to epoxy weight ratio reached 4:1. Macroscopically, from Figure 3.8(d) and (e), the concentration of the samples developed by centrifuge are lower than the high pressure compressed matching layer shown in Figure 3.8(f) that the large epoxy isolation cannot be found in between the island of alumina powder composite. Thus, for using the same amount of alumina powder, the high-pressure compression method produces a relatively higher density. Nevertheless, by benefiting

from the absence of the air cavity and large volume of epoxy, the homogeneity of the compressed matching is higher than other development method which can be seen from the highly close package aluminum oxide and more uniform distribution of epoxy. This high microscopically homogeneity of matching confirmed the equality of acoustic pulse transmission with its aperture to reduce the aberration of acoustic pulse which is more effective in high frequency array transducer. The homogeneity of transmission has barely been mentioned or concerned in most of the previous report related to acoustic matching layer but has been investigated and applied comprehensively in optical filed. On the other hand, for ceramic material due to its crystallinity structure which is harder than metal to form a high uniformity powder. Thus, dynamic range of the ceramic powder diameter is larger than metal. According to this, by using this compression method on metal composted matching, the homogeneity can be further enhanced.

3.5 SUMMARY

In this chapter, a new matching layer development method using high pressure compression has been presented. The longitudinal velocity and acoustic impedance of the developed matching can be manipulated by the applied pressure and the component weight ratio. From the aluminum oxide and epoxy mixture demonstration, the maximum longitudinal velocity and acoustic impedance can be accomplished as 3961 ms^{-1} and 9.52 MRayl , respectively, with a 4:1 aluminum oxide to epoxy ratio and prepared under 62.4 MPa pressure. The acoustic properties are relatively higher than others reported matching with different material and method. The great uniformity and homogeneity of the developed matching by this high-pressure compression method also has been shown in macro and microscopic scale. This may reduce the distortion or the aberration of the

matching to produce a more coherence acoustic signal in array transducer especially the one using electrical steering method for biomedical imaging. Transducers have demonstrated an excellent performance by using the matching fabricated in this investigation. The ultrawide 91% -6 dB bandwidth of a 53 MHz transducer is comparably higher than those formerly reported results. Nevertheless, this new presented method is good for applying on manufacture due to its low-cost consumption and simplicity of process.

CHAPTER 4

STUDY OF ADVANCED FABRICATION METHOD

4.1 ARRAY FABRICATION METHOD INVESTIGATION

In this chapter, laser cutting and mechanical dicing processes for array transducer fabrication are investigated. The array patterning is a very important process since the performance of transducers is significantly influenced by the structure of the elements in array transducers such as phased array. To increase the frequency and bandwidth of a phased array, for example a 20 MHz phased array, the array elements should have an extremely small width thickness ratio of 0.375 to prevent the side lobe effect by narrower the pitch of the element than $\lambda/2$ at center frequency, i.e. $37.5 \mu\text{m}$ using the velocity of acoustic wave in water $\sim 1460 \text{ m/s}$. This narrow pitch is extremely difficult to achieve by any method due to the 70% minimum volume ration requirement of the elements to exhibit the highest electromechanical coupling coefficient. Laser cutting is one the premium choice due to nanoscale narrow wavelength of light wave. Comparing with mechanical patterning method, laser cutting has less or nearly no mechanical vibration, thus the high aspect ratio element would not fall. Shenzhen University has cooperated in processing the laser cutting that fulfilled the technical specification requirement of this phased array design. The laser cutting machine can produce a very narrow pulse width around picosecond or femtosecond. This extremely short pulse width can produce a relatively small focus, down to a few-micrometer diameter, and high pulse amplitude which can further narrower the cutting kerf. Besides, the short pulse width can reduce the recrystallization effect around the laser cutting path, since heat generated by the laser is

only in an extremely small zone that can rapidly diffuse to the surrounding material. A PMN-0.28PT specimen is prepared for trial set as multiple cutting conditions, including laser feeding speed, laser pulse repeating frequency, pulse power and dicing quantity. Piezoelectricity and topography measurement have been done on the specimen after diced to compare the laser cutting and conventional mechanical dicing method, also analyze the feasibility of laser cutting and optimum laser cutting condition for PMN-0.28PT material for fabrication 20-MHz phased array ultrasound transducer.

4.1.1 Laser Cutting

By collaboration with Shenzhen University, we have carried out study of laser cutting process on PMN-0.28PT single crystal as a potential advanced process for fabrication of high-frequency transducer. A Ti-Sapphire femtosecond laser as shown in Figure 4.1 with wavelength of 650-1100 nm and constant frequency of 1 kHz may fulfill the technical specification requirement for phased array kerf cutting. The kerf profile (such as kerf width and depth) and cutting quality of the laser micro-machined PMN-0.28PT single crystal were studied with different laser process parameters. Two different parameters were varied, including power and pass number. At first, laser power from 230 mW to 50 mW, were implemented to investigate the quality of kerf such as depth and width. From Figure 4.2, one can see that the kerf width observed from the top view of PMN-0.28PT single crystal is directly proportional to the laser power. When the laser power is 230 mW, the kerf width is larger than 50 μm , and the element can only be barely observed from the gap between two kerfs. When the laser power reduces to 50 mW, the kerf width is significantly reduced (as shown in Figure 4.3), suggesting that the kerf could be small enough for the phased array ultrasound transducer fabrication at high frequency like 20

MHz. However, the top view only shows the kerf width of the laser cutting. The cutting depth can only be determined by cross-sectional image which is an important factor controlling the resonance frequency of the PMN-0.28PT.

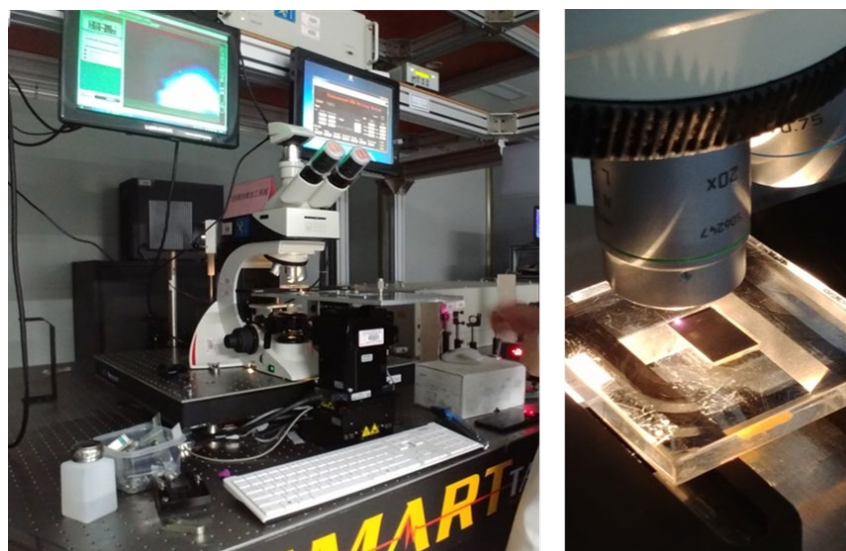


Figure 4.1 The experimental set up of laser micro-machining.

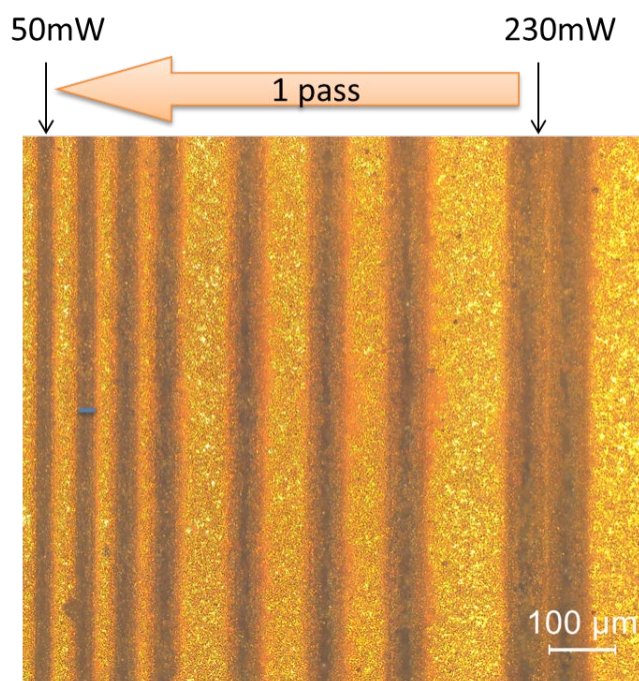


Figure 4.2 An optical photograph of the surface of the laser micro-machined kerf of the PMN-0.28PT single crystal (laser parameters: 50 to 230 mW, 1 kHz, 0.1mm/s, 1 passes).

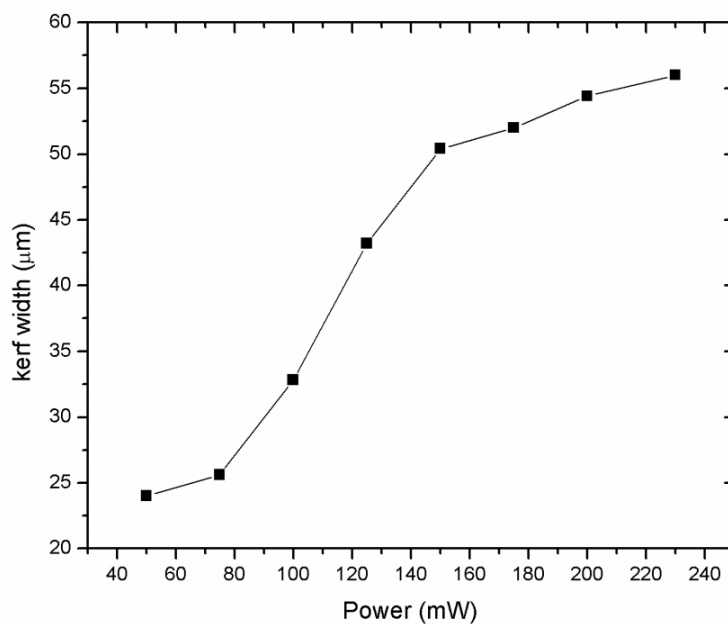


Figure 4.3 Dependences of the laser power on the kerf width of the PMN-0.28PT single crystal surface with one pass.

Figure 4.4 shows cross-sectional images of the laser micro-machined kerf of PMN-0.28PT characterized by scanning electron microscopy (SEM). One can see that there is a close correlation between the kerf depth and laser power, and nearly linear relationship of laser power and kerf depth is plotted in Figure 4.5.

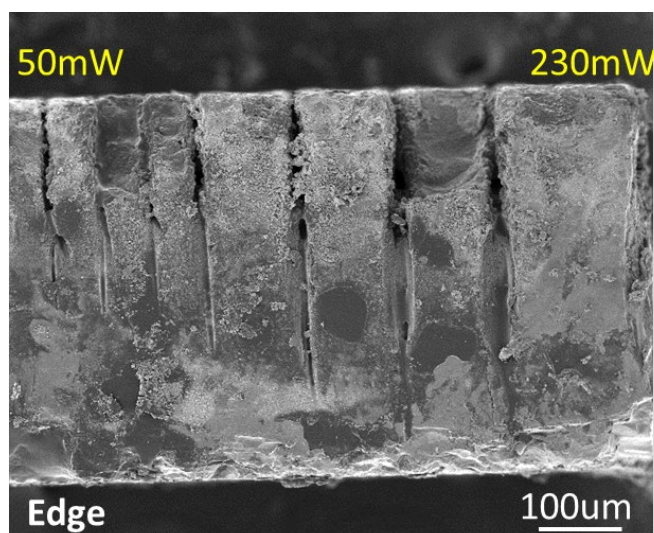


Figure 4.4 SEM cross-section image of the edge of the laser micro-machined kerf of the PMN-0.28PT single crystal showing the kerf depth as a function of laser power.

It is well-known that during laser cutting, the focus zone of the laser beam is located directly at the cutting point, and the material at the focus point is melted and vaporized away, leaving an edge (or kerf). The thermophysical properties of the material sufficiently affect the result of the kerf. Based on our results, it is found that the laser power greatly influences on the kerf depth and width. From the graphs of kerf profile as a function of power in a single pass process, the general proportional relationship between depth and width to the power are shown. These direct relationships provide a fast and effective reference to determine the kerf required to be ablated in PMN-0.28PT single crystal.

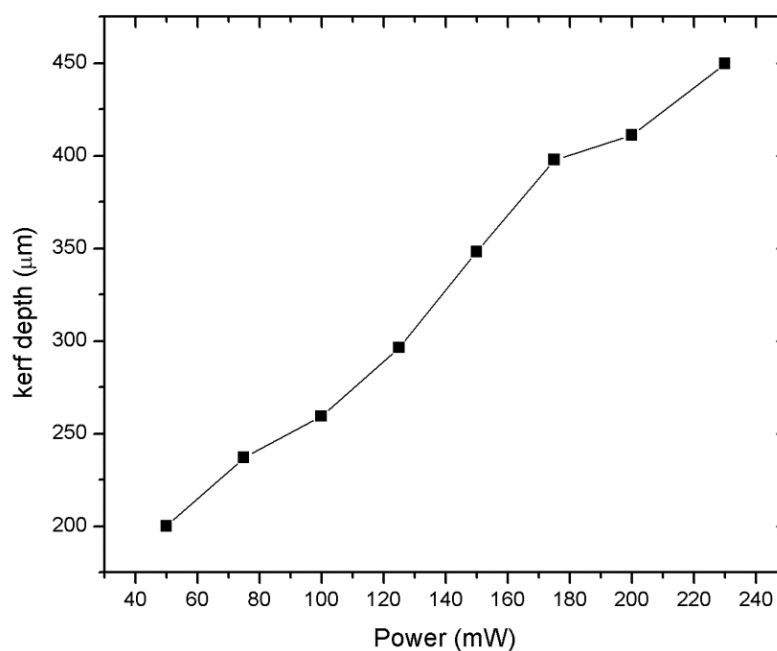


Figure 4.5 Dependences of the laser power on the kerf depth of the PMN-0.28PT single crystal with one pass.

Followed by identifying the optimum laser power, different pass numbers with a constant power 50 mW were used to obtain the cutting profile. As shown in Figure 4.6, it can be seen that the kerf is wider when the pass number increases. During the multi-pass process, the laser beam is supposed to be focused exactly on the surface at the first pass. The laser

beam offset of the later pass is different from that of the former pass so that the laser energy flux would become lower for the later pass. When the pass number increases, the laser energy flux at the crystal surface becomes larger. As a result, an increase of pass number leads to an increase of kerf width.

Besides, the kerf depth is supposed to be increased linearly when the pass number increases. However, there is no significant change with pass number increases as shown in Figure 4.7. The result suggests that the depth relation is limited using a single pass process. During the multi-pass process, the laser energy flux would become lower for the later pass. Consequently, the later pass may not have enough energy for further ablation, so the result of kerf depth versus pass number does not show any correlation.

To further investigate the effect of laser ablation on PMN-0.28PT single crystal, the SEM cross-sectional image of the middle part of laser micro-machined kerf has been displayed in Figure 4.8. Although a clear kerf profile can be observed at the edge of the sample, one

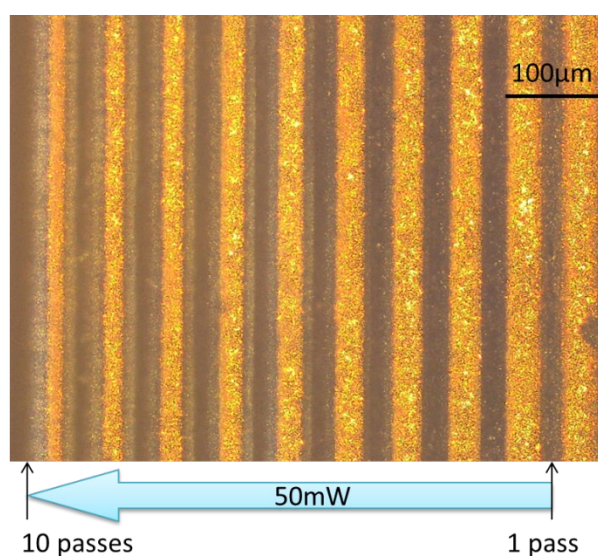


Figure 4.6 An optical photograph of the top of the laser micro-machined kerf of the PMN-0.28PT single crystal (laser parameters: 50mW, 1 kHz, 0.1mm/s, 1 to 10 passes).

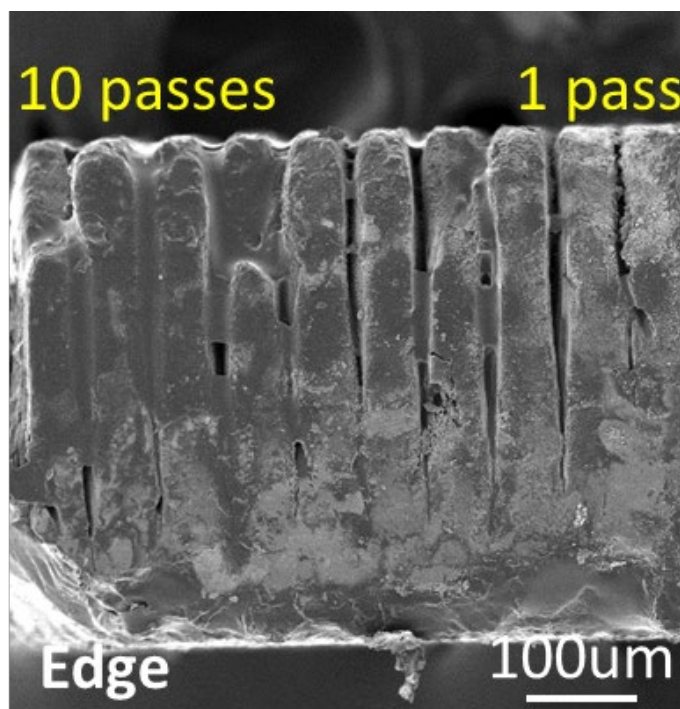


Figure 4.7 SEM cross-section image of the edge of the laser micro-machined kerf of the PMN-0.28PT single crystal showing the kerf depth as a function of pass number.

can see that the kerf can be barely defined in the middle part of the sample as shown in Figure 4.8(a). This middle cross-section was diced by a dicing saw in a cutting direction perpendicular to the laser kerf direction. Using dicing saw can prevent the result affected by the cutting rather than the original testing. From the enlarged image Figure 4.8(b), the kerf width closed to the surface becomes wider when the pass number increases which is consistent with the optical photography obtained from the surface. However, the depth of the kerf can be verified that it is not as deep as the one obtained at the edge. In other word, the result shows a discontinuous edge with one kerf. In Figure 4.8(c), one can see that the kerf is fully filled by residues. It is believed that when the laser passes the sample surface, the crystal is melted and vaporized. However, some materials cannot be vaporized away from the surface because of the narrow valley (or extremely high aspect ratio of the kerf). When the melting rate is faster than the vapor escape speed, the vapor condensed inside

the valley. The wall surface of the kerf supports a large contact surface that allows the vapor releasing heat energy and re-crystallized again. The recrystallization located close to the front surface blocked the laser beam and influencing the laser cutting depth. As a result, a cavity appeared at the bottom of the cutting kerf and the kerf is sealed by the recrystallization. The recrystallization can be reduced by the ultrasound cleaning treatment, but it cannot be fully removed.

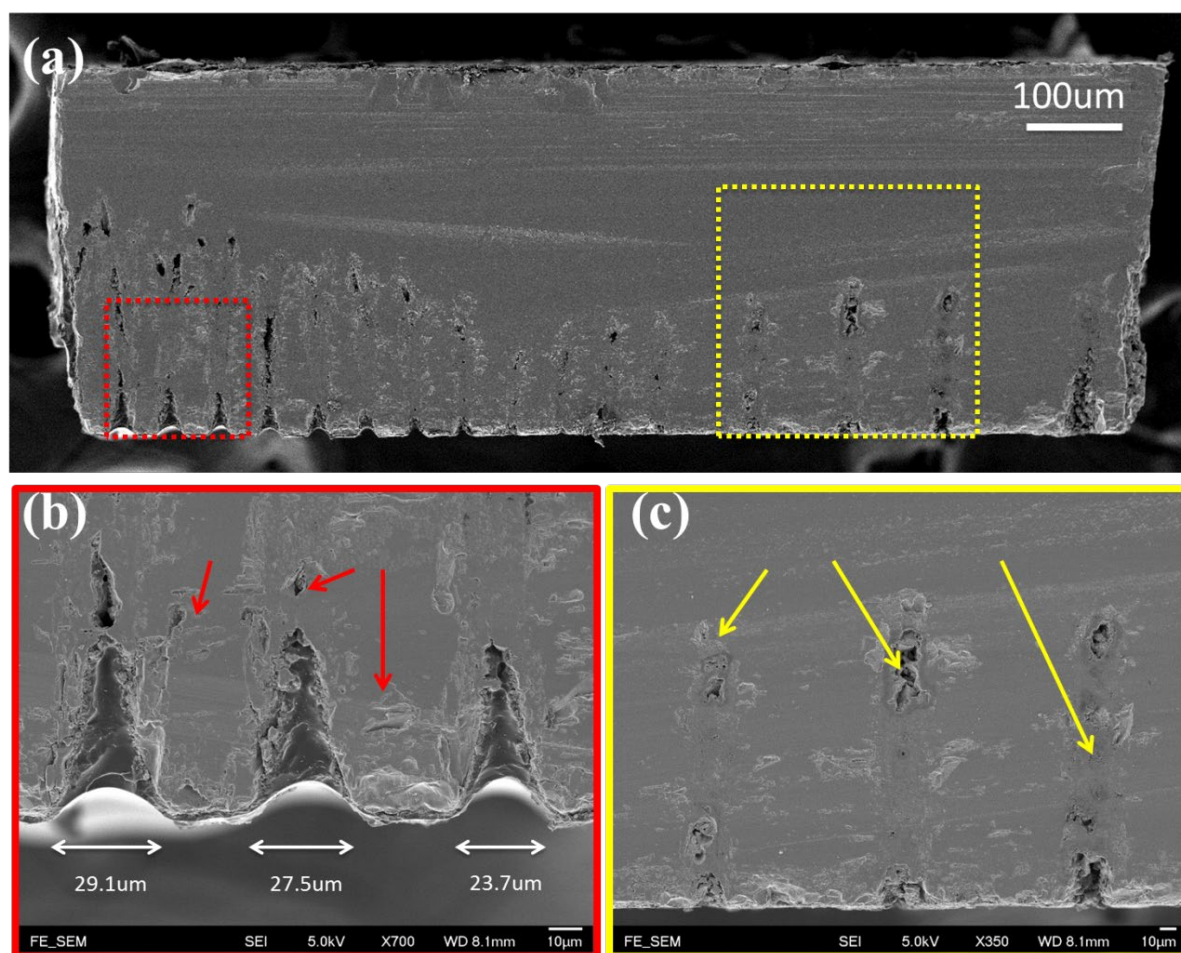


Figure 4.8 SEM cross-section image of (a) the middle part, (b) area using 50mW laser energy and (c) energy from 125 mW (Left) to 175 mW (Right) of the laser micro-machined kerf of the PMN-0.28PT single crystal.

Another PMN-0.28PT sample was processed by laser cutting for further investigating a solution for this problem. With using a focus lens. Since a high cutting pass number and

lowest laser power in a thin sample ($\sim 100 \mu\text{m}$), residues can be significantly removed by the ultrasound cleaning treatment, but the shape of the kerf changes to an elliptical paraboloid shape, which is shown in Figure 4.9. The bright contrast in the images corresponds to the PMN-0.28PT crystal and the dark contrast regions are epoxy filled in the kerf. The single crystal has been cut into several non-rectangular elements with a very narrow top area and wider bottom area. This parabola shape is attributed to the focused laser beam shape. In this case, although no significant residue presents in the kerf, the shape changes to a shape that strongly affects the performance of piezoelectricity as well as the acoustic characteristic of the ultrasound transducer. Besides, the performance of piezoelectric is hard to be estimated that affects the design and improvement progress of the transducer.

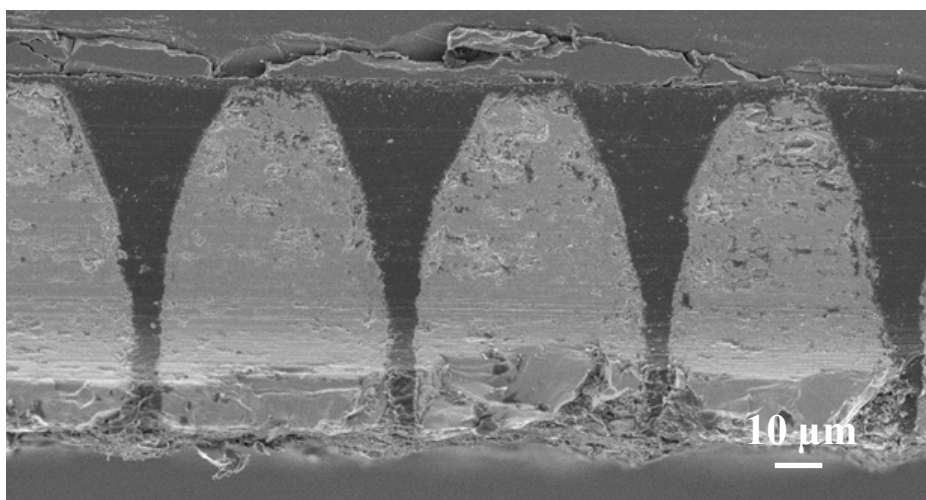


Figure 4.9 SEM cross-section image of the middle part of the laser micro-machined PMN-PT crystal.

These results show that, laser cutting may not fulfill the requirement of our designed high-frequency phase array transducer where the pitch size is about $60 \mu\text{m}$. A larger depth of field laser lens is required to produce a smaller width-to-depth ratio kerf. Other than the

cutting geometry, the piezoelectric properties may also be affected by the heat generated by the laser beam. The influence of piezoelectric properties by laser cutting has been investigated by our group which is illustrated in Figure 4.10⁸⁷. In the PFM picture, the macrodomains of the PMN-0.28PT less than 20 μm distance away from the kerf disappear after the laser cutting. Therefore, the polarization cannot be induced within this range even applying an E-field. The piezoresponse is started to recover at 50 μm distance away from the cutting edge. This piezoresponse reduction may affect the performance of the fabricated transducer, especially the phased array transducer, due to the narrow element width.

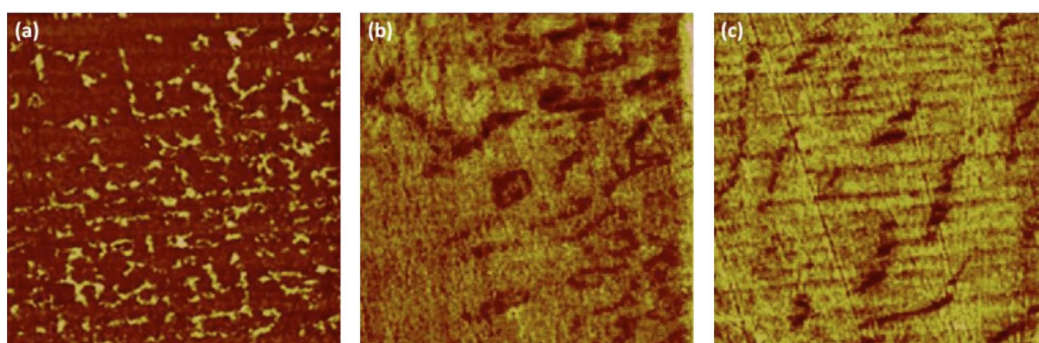


Figure 4.10 Piezoresponse amplitude images of (a) 20 μm , (b) 50 μm and (c) 100 μm distance away from the 355 nm Nd:YAG laser cut kerf⁸⁷.

4.1.2 Mechanical dicing

A new dicing blade with a smaller blade thickness, down to 10 μm thick, has been produced recently by DISCO (model DAD 321, DISCO Co. Ltd., Omori-Kita, Japan). This very thin dicing blade increases the stability during the dicing process and gives us more space to reduce the pitch size approaching ideally $\lambda/2$ with an increased center frequency. The picture of the dicing blade is shown in Figure 4.11. According to its specification, the highest aspect ratio is 38:1, i.e. combination of exposure and kerf width

is 0.38 mm and 0.010 mm, respectively.



Figure 4.11 The picture of the dicing blade (model ZHZZ series).

This high aspect ratio is supreme for transducer fabrication since a transducer usually has an ideal $\lambda/2$ pitch requirement and the surface area affects the electrical impedance of the transducer. For achieving high sensitivity of the transducer, it is desired to have an electrical impedance close to 50Ω to achieve optimized electrical coupling with the input signal. Typically, the impedance of the phased array transducer is a few hundred to a few thousand Ω . Therefore, the impedance can be reduced by increasing the surface area. In our investigation, the experimental dicing kerf of the dicing blade (ZHZZ-AZ model, DISCO Co. Ltd., Omori-Kita, Japan) with 0.01 mm blade width and 0.38 mm exposure was within a range from $13 \mu\text{m}$ to $15 \mu\text{m}$ with a 0.15 mm to 0.18 mm dicing depth tested on a 0.5 mm thick PMN-0.28PT specimen with $8 \times 13 \text{ mm}^2$ dicing area. The feeding speed and the spindle rotational speed were 0.4 mm/s and 20000 rpm. The maximum rotational speed of the spindle is 60000 rpm, however, high rotational speed generates more vibration that may widens the kerf, or more seriously breaks of the element. Our experimental data shows that, when the saw rotation speed is equal to or lower than 20000 rpm, the failure rate of the fabricated array transducers is the lowest.

The surface profile and cross-sectional view of the diced specimen by using 20000 rpm are shown in Figure 4.12 and Figure 4.13. The dicing grooves, i.e. the kerf shape, is extremely straight with such a high aspect ratio. The shape of the dicing grooves affects the shape of the piezoelectric element in the phased array transducer and determines the vibration mode along the axial direction and the frequency uniformity of the elements. In this case, the dicing grooves developed by the ZHZZ new dicing blade already fulfilled the requirement.

With this new dicing blade operating at the optimized dicing speed, the diced specimen had a high yield rate. Besides, a ceramic polycrystalline ferroelectric material PZT, which has a slightly lower piezoelectricity than PMN-0.28PT, was also tested.

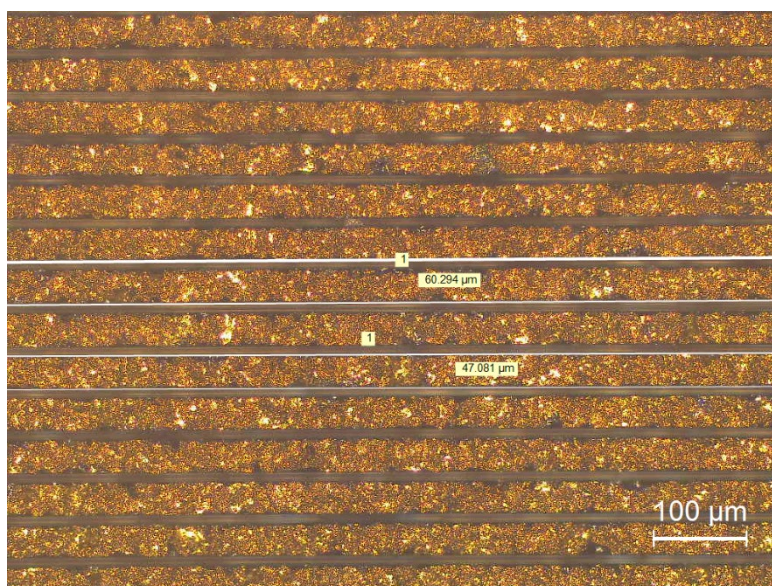


Figure 4.12 The surface profile of the diced PMN-0.28PT.

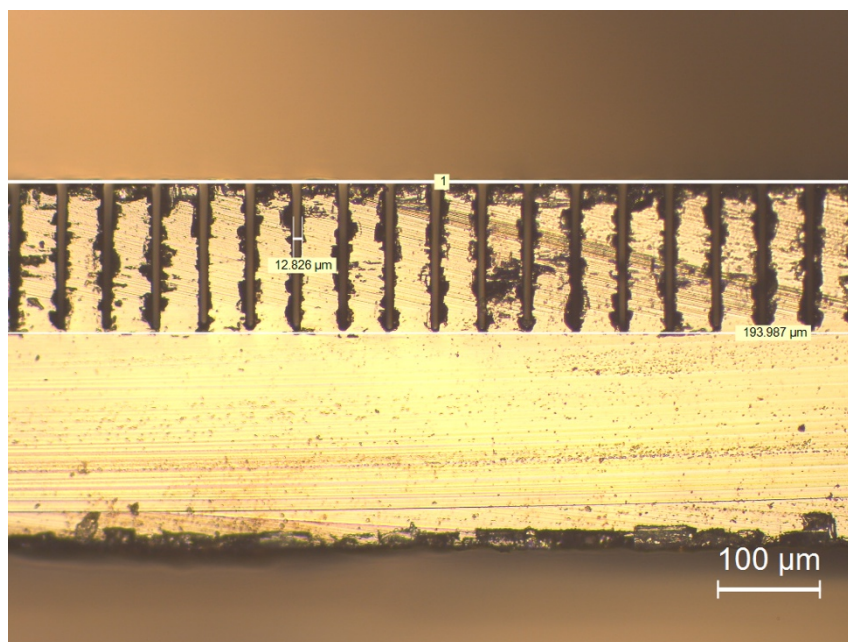


Figure 4.13 Cross section of the diced PMN-0.28PT specimen.

With the same dicing condition as PMN-0.28PT, the PZT specimen shows a successful rate nearly 100%, which is higher than the PMN-0.28PT. To further enhance the success rate of PMN-0.28PT based transducer, the relationship between the surface roughness and dicing parameters was investigated. PMN-0.28PT is a single crystal which is more brittle than the PZT, so any cracks generated on the surface may extend along the weak point, and consequently, the whole element dropped off. A comparing experiment between a polished and unpolished surface of the PMN-0.28PT crystal has been carried out. Figure 4.14 and Figure 4.15 show the result of the diced PMN-0.28PT on the polished and unpolished samples. The PMN-0.28PT polished by a fine polishing paper (the 3 μ m polishing paper which equals to 8000 grit sandpaper) exhibits a 100% success rate, which is slightly higher than the PMN-0.28PT with rough polishing treatment (3000 grit sandpaper) and remarkable higher than the one without any surface treatment.

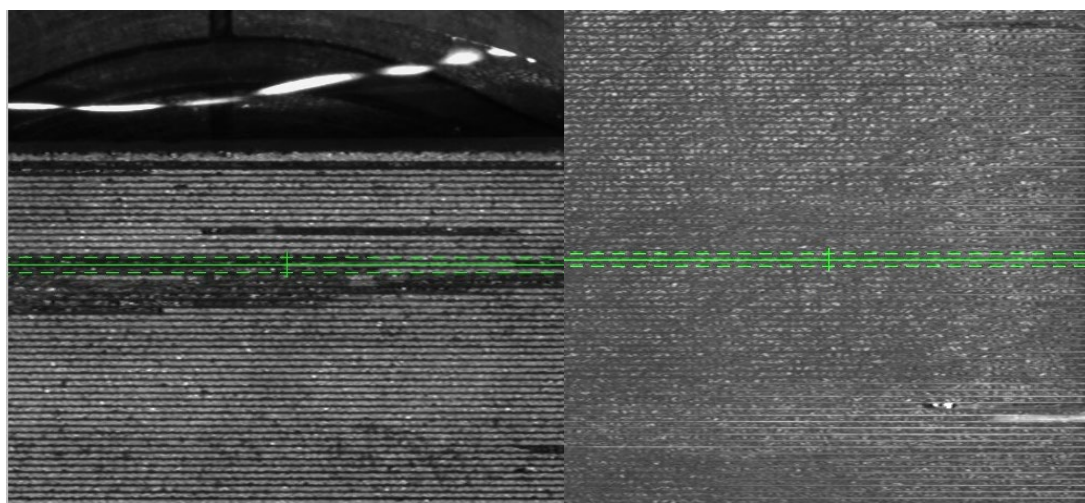


Figure 4.14 Profile picture of the diced PMN-0.28PT without surface polish treatment (Left) and, with surface polish treatment by 3000 grit sand paper (Right).

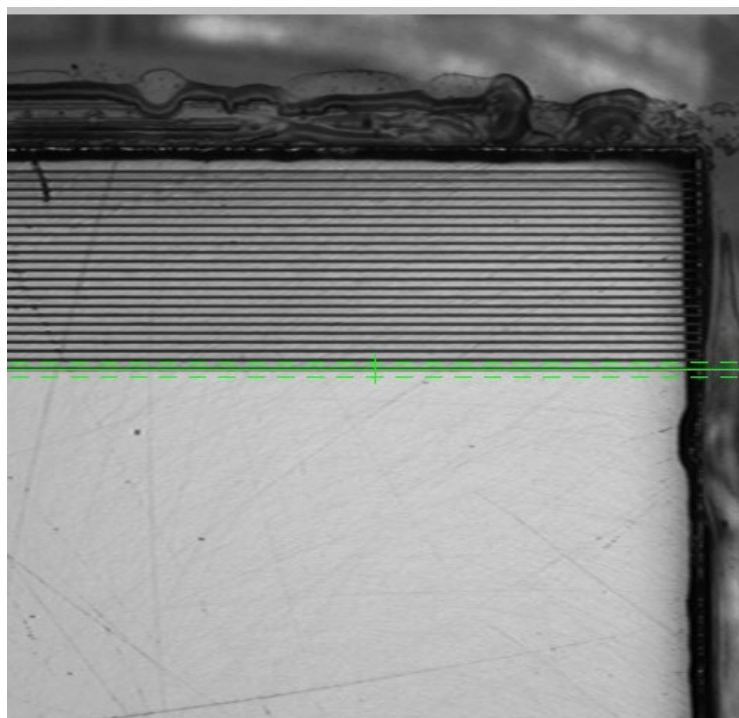


Figure 4.15 Profile picture of the diced PMN-0.28PT with surface polish treatment by using 3μm polishing paper (~8000 grit).

This proves that the surface roughness is a reason causing the element failure during the dicing process. By reducing the surface roughness, the pitch of the array maybe further decreased from 0.8λ ($60 \mu\text{m}$). This may eliminate the side lobe effect of the phased array transducer exhibiting in imaging process, thus increase the lateral resolution.

By comparing the samples with the same thickness prepared by dicing saw and laser cutting, which are shown in Figure 4.16 (a) and (b), the sample prepared by dicing saw has a relatively sharp kerf than that of laser-machined. Also, one can see that the affected area near the kerf of the diced sample is much smaller than that of laser machined. Numerous holes and defects can be found around the kerfs prepared by laser cutting. It suggests that with the significant thermal effect during the laser ablation, single crystal seems to be changed into polycrystalline or amorphous. It may lead to the breakdown of macro-domains into micro-domains nearby the kerf and cause the domain nature changes resulting in impairing the piezoresponse of the crystal locally.

In this implementation, the direct relationships of kerf width, depth and laser power provide a fast and effective reference to determine the kerf required to be ablated in PMN-0.28PT single crystal. However, laser cutting of the crystal will cause local area melting and recrystallization, some of residues still filled in the kerf that the elements cannot be fully separated. If dicing saw is used for cutting, it has a better cutting profile than that of laser cutting in the 15 μm range of kerf width. In fact, this cutting kerf is nearly reaching the limitation for traditional mechanical cutting technique for fragile material like PMN-0.28PT. If the kerf width requires a further reduction ($<10 \mu\text{m}$), further treatment or process improvement of laser cutting, or other cutting method is essential. Under this circumstance, for rectangular or polygon shape cutting, mechanical dicing is better than the laser cutting. For using the pre-treatment, the yield rate of mechanical dicing cutting applied on a PMN-0.28PT is same as the laser cutting. Thus, a mechanical dicing method is chosen for patterning the phase array instead of the laser cutting. Although laser cutting may not be suitable for PMN-0.28PT array transducer, it is still one of the choices for

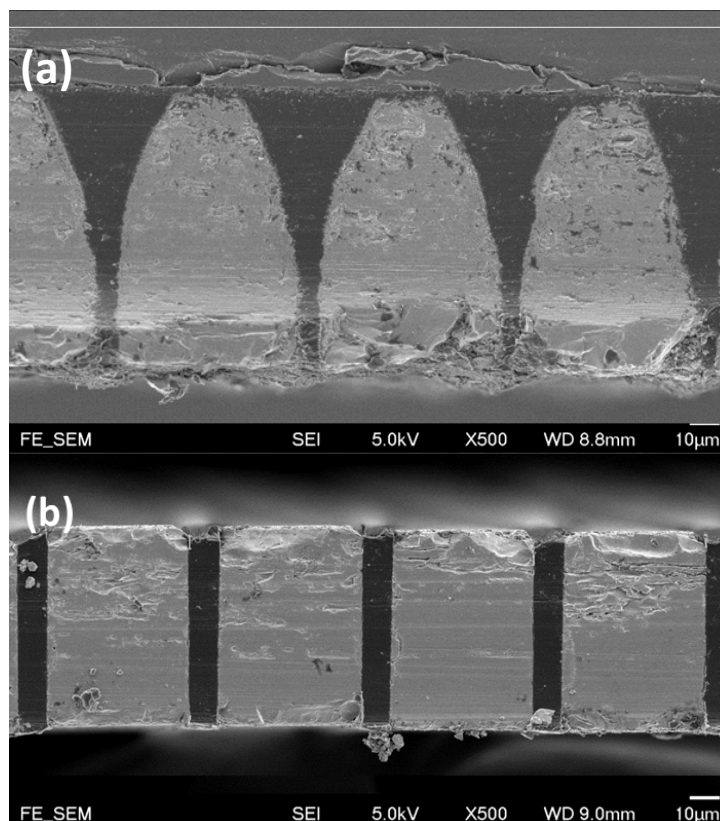


Figure 4.16 SEM cross-section image of the middle part of the (a) laser micro-machined and (b) diced kerf of the 100 μm -thick PMN-0.28PT single crystal, bright and dark color denote PMNPT crystal and epoxy, respectively.

possessing piezoelectric materials with higher Curie temperature. Besides, comparing to mechanical dicing, it can cut sample to a non-rectangular or non-polygon shape which will be adopted for producing an annular array

4.2 SUMMARY

In this chapter, advanced laser cutting process and fine mechanical cutting process are investigated for array transducer fabrication, especially for single crystal PMN-PT based array transducers. Laser cutting has its advantages such as narrower kerf width, less element drop-off and unlimited shape of kerf path, but also show disadvantages such as

v-shaped kerf and high-temperature included degradation of ferroelectricity. Mechanical cutting can reach a limit of 13-15 μm kerf with perpendicular wall, but sample surface has to be fine polished in order to obtain highest success rate of cutting. This study provides references and solutions of alternative fabrication processes for high frequency array transducer, especially transducers based on single crystal piezoelectric materials with fragile nature.

CHAPTER 5

20-MHZ PHASED-ARRAY ULTRASOUND TRANSDUCER FOR IN-VIVO ULTRASOUND IMAGING OF SMALL ANIMALS

5.1 INTRODUCTION

Among many medical diagnostic imaging techniques for human and small animals, ultrasound imaging^{4,5,8} possesses fast acquisition, non-destructive and non-ionizing radiation advantages compared to microcomputed tomography (micro-CT), micromagnetic resonance imaging (micro-MRI) and micro-single photon-emission tomography (micro-SPECT), and therefore, is becoming a popular theragnosis tool for clinical medicine and veterinary medicine⁸⁸⁻⁹⁰. It is also an important imaging tool for preclinical study on pathology and epidemiology. In recent decade, benefited from the rapid development of computing technology, the size of the ultrasound transducer and its electrical circuit structure are reduced. In addition, with its real-time image acquisition capability, it can be used for assisting invasive surgery without producing radiation dose to patient and surgeon from exposing to fluoroscopic X-Ray imaging⁹¹⁻⁹³. However, for veterinary medicine and preclinical study targeting on small size animals, the clinical ultrasound transducers are insufficient to observe small-scaled feature of animal which probably exceeds its spatial resolution limit. Therefore, aiming at acquiring contour and related biological information of small-scaled organs or tissues, ultrasound transducers with high spatial resolution, high sensitivity as well as small aperture size are highly

desired.

Resolution is an important criterion for high-quality *in vivo* small animal imaging. In diagnostic ultrasound, the axial resolution mainly depends on the frequency and acoustic pulse length emitted and received by the transducer; and the lateral resolution depends on frequency, beamforming method and elements' width. Most of these factors are determined by the piezoelectric properties of the active layer in a piezoelectric ultrasound transducer. The single crystal relaxor ferroelectric material $\text{Pb}(\text{Mg}_{1/3}\text{Nb}_{2/3})\text{O}_3\text{-}0.28\text{PbTiO}_3$ (PMN-0.28PT) is an excellent candidate for the active layer fulfilling the stringent requirements of transducer for small animal *in vivo* imaging. Owing to the structural nanoscale cation disorder of relaxor ferroelectric crystal, the impressively high ferroelectricity is achieved with the presence of polar nanoregions (PNRs)⁹⁴⁻⁹⁸. Most importantly, relaxor ferroelectric single crystal at morphotropic phase boundary (MPB) possesses much higher ferroelectricity, piezoelectric constant ($d_{33} \geq 2000$ pC/N), dielectric constant and electromechanical coupling factor ($k_{33} \sim 0.92$) compared to non-relaxor based PZT⁹⁹⁻¹⁰⁴. As a consequence, a relaxor ferroelectric-based ultrasound transducer could accomplish a shorter longitudinal pulse length and higher sensitivity than that with polycrystalline PZT^{26,70,100,105,106}. However, the relaxor PMN-0.28PT has disadvantages such as low ferroelectric phase transition temperature (T_m), low coercive field (E_c) and mechanical quality factor (Q_m), leading to reduced stability of its polarization in driving condition. Consequently, a PMN-0.28PT-based transducer requires a more stringent temperature control or an additional pre-driving DC voltage to retain its polarization and device performance^{70,107}. Rather than its piezoelectric performance disadvantage, single crystal PMN-0.28PT also has a brittle nature that increases the fabrication difficulty of 1-D and 2-D array transducers and reduces the

uniformity and yield rate of final product.

In academic field, Foster *et al.* has demonstrated an *in vivo* small animal imaging with their developed 35 MHz PZT-based linear array ultrasound transducer in 2009⁷², showing a real-time visualization of flow in the mouse placenta, flow development in embryo and flow of the adult cardiac. However, instead of using linear array beamforming, phased array transducer is an alternative method that can accomplish the *in vivo* small animal imaging with a small aperture size and larger angle of view. The lack of the steering angle of linear array provides a freedom in element width and higher sensitivity (using an elements width matching the electrical impedance) but sacrifices further shrinking of aperture size. On the other hand, phased array transducer electrically actuates all elements individually with a specific time delay value to execute an angular steering, and therefore, its aperture size can be further reduced. In a steering image, the enhanced strength of the grating may create a ghost artifact at high contrast object affecting the image quality and the diagnosis. Thus, most of the phased array transducer has a pitch as narrow as $\lambda/2$ to suppress the grating lobe. The total size of the transducer is then significantly smaller than the linear array.

These characteristics of phased array make it high potential in imaging small animals through the relatively much smaller hollow size on high dense tissue for preventing signal loss or artifact caused by reflection. Yet, an *in vivo* image demonstration using phased array transducer is rarely reported due to its limited sensitivity of imaging for a much smaller aperture size compared to a linear array. Therefore, there are plenty of room to investigate the potential for small animal medical imaging using phased array transducer with PMN-0.28PT single crystal at high frequency range. In light of these, in this section, we present a 20-MHz PMN-0.28PT single crystal relaxor ferroelectric phased array

transducer which has higher acoustic performance than polycrystalline PZT linear arrays. Resolution of the developed transducer and the demonstration of *in vivo* small animal imaging are presented. This outcome shows a feasible way to manufacturing single crystal-based high-frequency phased array transducers.

5.2 EXPERIMENTAL DETAILS OR EXPERIMENT

5.2.1 Piezoelectric layer Characterizations

The piezoelectric properties of the piezoelectric material are measured using an impedance analyzer (4294A, Hewlett-Packard, USA) and a piezoelectric constant meter. During the measurement, the impedance analyzer drives an electrical signal with a sweeping frequency, maximum range from 40 Hz to 110 MHz, on the materials or devices through an adapter, 16034E (Hewlett-Packard) for bulk material or 16047D (Hewlett-Packard) for device, and measures the specimens' electrical response. The electrical impedance and phase angle are measured using the impedance-theta ($Z-\theta$) mode. The capacitance and dielectric loss are measured using parallel capacitance-dissipation factor (C_p-D) mode. The impedance and phase-angle responses with frequency of a typical piezoelectric bulk material are shown in Figure 2.8⁴⁷. For the impedance response, f_r and f_a are the resonance frequency and the anti-resonance frequency, respectively. Using the resonance frequency and the thickness, the frequency constant of the material can be calculated. The electromechanical coupling coefficient (k_t) can be calculated by the following equation:

$$k_t^2 = \frac{\pi}{2} \cdot \frac{f_r}{f_a} \cdot \tan \left[\frac{\pi}{2} \cdot \frac{(f_a - f_r)}{f_a} \right] \quad (19)$$

Dielectric constant ε_r and clamped dielectric constant ε_c can be obtained at 1 kHz and $2f_r$,

respectively, through the C_p - D measurement. The calculation is shown as follows:

$$C = \epsilon_0 \epsilon_r / c A / d \quad (20)$$

where C is the capacitance at a certain frequency, A is the area of the electrode, d is the thickness and ϵ_0 is the permittivity at vacuum ($=8.854 \times 10^{-12}$).

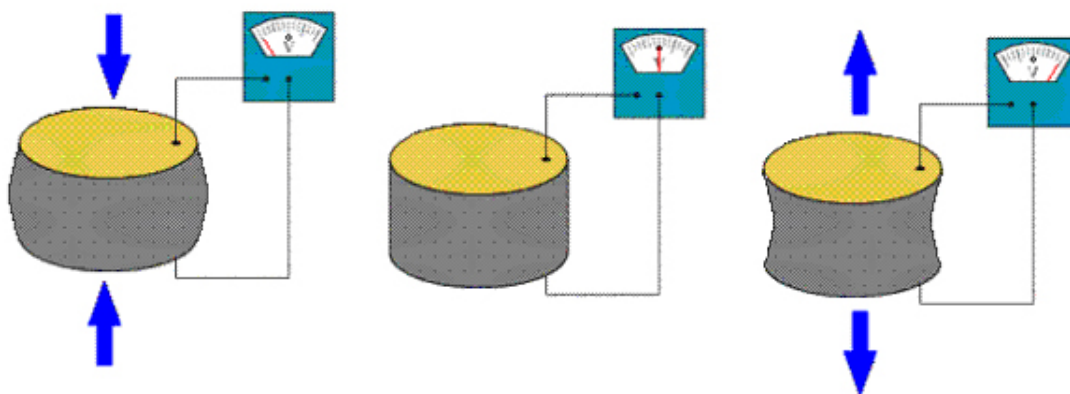


Figure 5.1 Working mechanism of piezo-meter¹⁰⁸.

The piezoelectric constant of the material was obtained using the piezoelectric constant meter. The conceptual diagram of the working mechanism is shown in Figure 5.1¹⁰⁸. The specimen is clamped by the driving probe that compresses the specimen with a fixed frequency. By measuring the generated voltage during the vibration, the piezoelectric constant is calculated and displayed.

The acoustic impedance of PMN-0.28PT piezoelectric material used in the transducer needs to be determined before designing the transducer. This parameter determines the acoustic impedance of the double matching layer and the backing layer that affecting the performance of the product. Those factors are also compulsory input parameters for both simulation software PiezoCAD and PZFlex. The acoustic impedance can be calculated by the acoustic velocity and the density of the material which has been shown in Chapter 3, where the details of the velocity and density measurement are also introduced.

5.2.2 Transducer Design

PiezoCAD has been used to optimize the design of the phased array transducer. By achieving higher uniformity and performance in biomedical imaging than the previous investigation, the side lobe and grating lobe effect, which are the most important factor affecting the lateral resolution or even creating a pseudo image along the lateral direction. Therefore, those effects need to be as suppressed as possible to minimize its adverse effect on imaging. The pitch of the array is designed as $60 \mu\text{m}$ (0.8λ) which is a value that can be produced by the mechanical dicing process with a highest yield rate and is close to the ideal value (0.5λ). The directivity of the phased array has been calculated by the following equation(21).

$$H(\theta) = \left| \frac{\sin\left[N\frac{\pi d}{\lambda}(\sin\theta - \sin\theta_0)\right]}{N \cdot \sin\left[\frac{\pi d}{\lambda}(\sin\theta - \sin\theta_0)\right]} \cdot \frac{\sin\left(\frac{\pi a}{\lambda}\sin\theta\right)}{\frac{\pi a}{\lambda}\sin\theta} \right| \quad (21)$$

Where N is the number of point source, d the pitch width, λ the acoustic's wavelength in water, θ the angle along the lateral-axial plane, and θ_0 the steering angle. The calculated directivity of the design has been shown in Figure 5.2

In this figure, the element number is set as 128. For comparing, different pitch values 1λ , 0.8λ and 0.5λ have been shown simultaneously in this figure. Only 1λ pitch design has shown a grating lobe at -90 and 90 degree. The designs with 0.8λ and 0.5λ pitch show a similar overall performance with the angle larger than 20 degree. An enlarged version figure in angle range from -10 to 10 degree has been shown in Figure 5.3.

A widest beam width is illustrated while the pitch is set as 0.5λ . Besides, the side lobe of

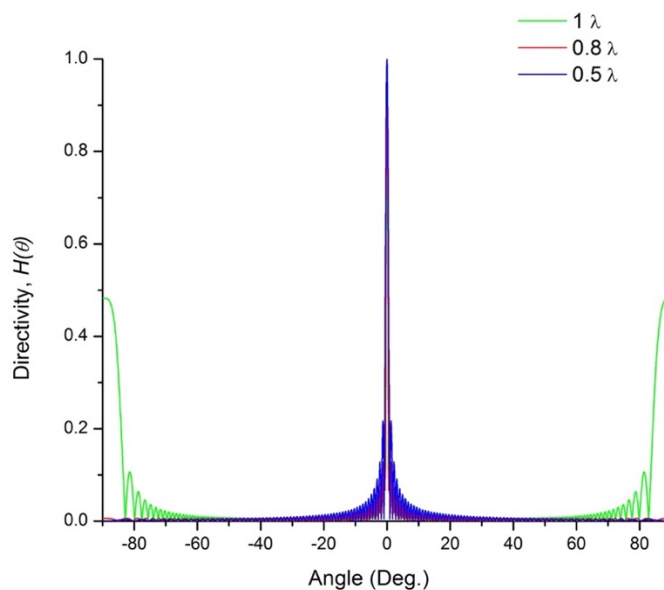


Figure 5.2 The simulated directivity of the designed elements dimension on the front surface from -90 degree to 90 degree.

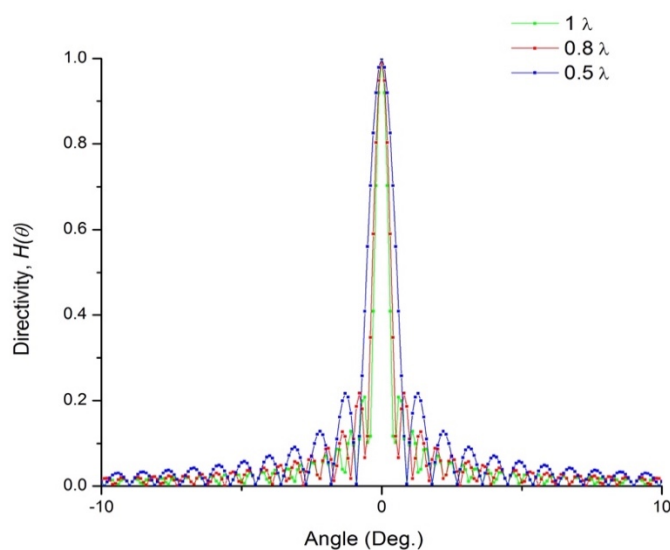


Figure 5.3 The simulated directivity of the designed elements dimension on the front surface from -10 degree to 10 degree.

the 0.5λ pitch design appears at the largest angle, around ± 2 degree, comparing with 0.8λ and 1λ . The side lobe of 0.8λ pitch, which is same as the presenting phased array design, is located at around ± 1 degree. Although the side lobe angle is narrow, the

amplitude of it is only 20% of the main lobe's amplitude. The 1° difference between 0.5λ and 0.8λ pitch is negligible. The following Figure 5.4 shows the beam directivity while the steering angle at $+30$ degree (left) and $+60$ degree (right). No grating lobe appears in any steering angle when the pitch is set as 0.5λ pitch. When the pitch is 0.8λ , grating lobes are shown at around -50 degree and -21 degree, respectively, at $+30$ degree and $+60$ degrees steering angles. In spite of the appearance of grating lobe, the angle between grating lobe and main lobe of 0.8λ pitch is still larger than 1λ and concurrently presenting in a lower amplitude.

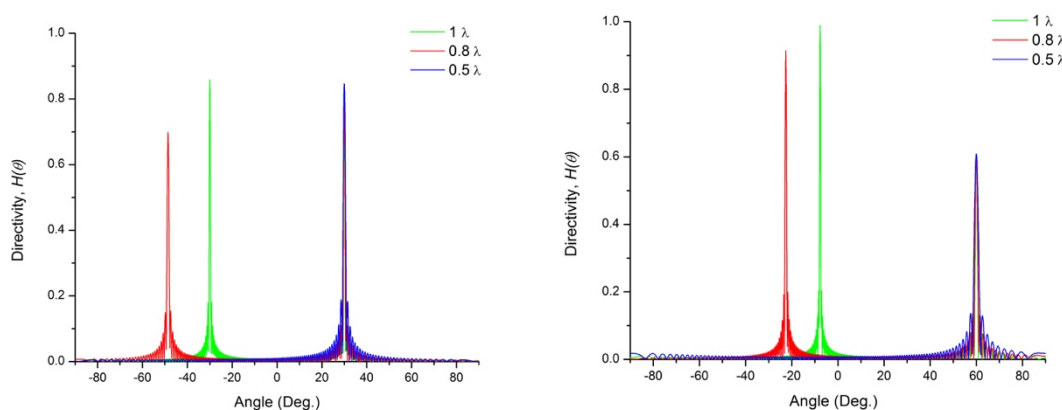


Figure 5.4 The simulated directivity of the designed elements dimension steering at $+30$ degree (Left) and $+60$ degree (Right).

Theoretically, the narrow width of element reduces the dimension of phased array, which is one of its merits allowing cardiac imaging through the narrow gaps of ribs. However, for setting the center frequency at 20 MHz, the 0.5λ pitch would be around $35 \mu\text{m}$. Therefore, an extremely narrow and high aspect ratio kerf is required which is impossible to construct by the mechanical approach. Alternatively, laser cutting could be a choice to construct the phased array. Laser cutting PMN-0.28PT has been reported by Piredda *et al.*, where a $15 \mu\text{m}$ cutting kerf width has been obtained using a 380 fs pulse laser¹⁰⁹. Foster *et al.* has also developed a PZT based linear array by laser cutting into $8 \mu\text{m}$ kerfs⁷².

Nevertheless, even using laser cutting, the cutting aspect ratio may still not be appropriate for producing a 0.5λ pitch. Meanwhile, the above reports also illustrated that the kerf produced by laser cutting shows a v shape valley and the cutting depth is hard to be controlled accurately. A previous investigation also revealed that the macro-domain near the laser cutting kerf was distorted causing an absence of piezoresponse within a range depending on the laser's power⁸⁷. According to the analyses presented above, by compensating the nature of material, patterning technology and performance, 0.8λ pitch is the optimal choice.

To remain the low electrical impedance of the array, the area of the elements should remain unchanged. Under this circumstance, the kerf was the only factor to be reduced. By using a blade model ZHZZ-AZ (DISCO Co. Ltd., Omori-Kita, Japan) which is called hub blade, the fluctuation of the blade during dicing can be reduced. The dicing kerf of the array was within 13.0 to 15.7 μm when using a 10 μm thickness hub blade. The impedance of the re-designed array is around 300 Ω , which has a value closer to 50 Ω . The electrical loss caused by this impedance difference can be slightly suppressed by an electrical coupling method.

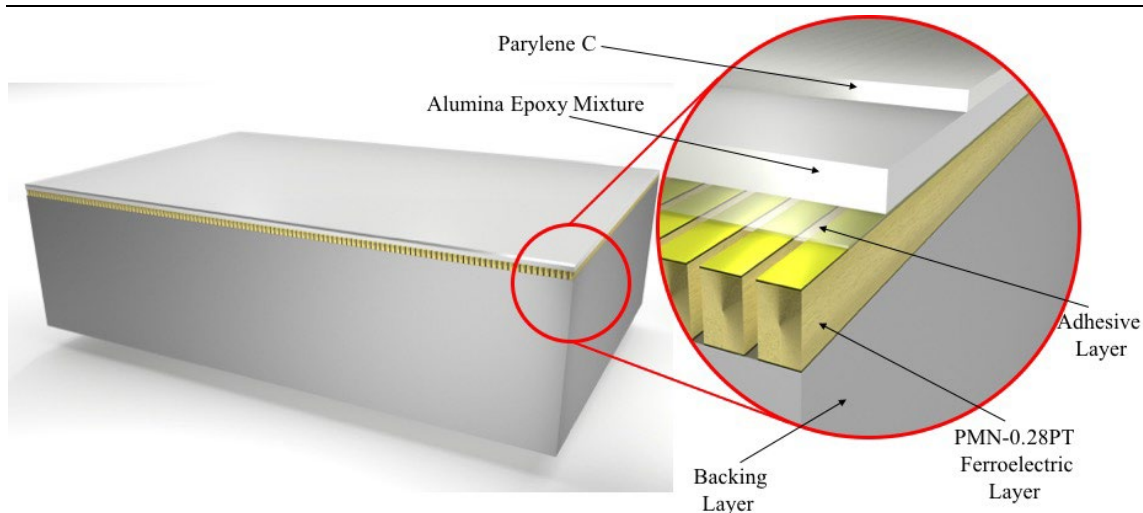
In the structure mentioned in section 1.3, the transducer contained three main components, a matching layer, backing layer and the piezoelectric layer. By achieving optimized performance, the material of matching layers has been investigated in Chapter 3. Besides, the backing layer has also been investigated to maximize the performance of ultrasound. The acoustic properties of the investigated matching and backing are listed in the Appendix 5 and Appendix 6. This matching layer was developed using a 62.4 MPa high pressure compressing stress applied on the alumina epoxy mixture with 2:1 weight ratio. The external pressure densifies the matching in result of an acoustic velocity enhancement.

This leads an acoustic impedance leap forward from a reported average 5.60 MRayl to now 8.54 MRayl^{30,86}. This impedance value is comparable to the heavy metal constituted matching, but with much lower attenuation. The significantly high acoustic impedance which has a better impedance coupling with the high acoustic impedance piezoelectric layer according to the quarter wavelength theory^{83,110}. Most importantly the enhancement is mainly contributed by the acoustic velocity instead of the density which allows a broader tolerance of thickness especially in high frequency.

The second matching layer was designed as Parylene C because it can be deposited to cover the whole transducer directly by using the Parylene C deposition system (Specialty Coating System, Inc., USA) due to the required thickness is extremely hard to produce by lapping method. Furthermore, the acoustic impedance of Parylene C (2.6 MRayl) was close to the calculated ideal acoustic impedance requirement (2.3 MRayl). In addition to the low acoustic impedance, the waterproof and chemical proof features of Parylene C can also prevent the transducer from short-circuited by the water invading into the transducer, concurrently enhancing the reliability of the transducer. The piezoelectric properties of the used PMN-0.28PT material (Shanghai Institute of Ceramics, The Chinese Academy of Sciences, Shanghai, China) and the properties of all acoustic layers are listed in Table 5.1 and Table 5.2, respectively. The schematic diagram of the designed transducer is illustrated in Figure 5.5

TABLE 5.1 MEASURED PIEZOELECTRIC PROPERTIES OF PMN-0.28PT BULK MATERIAL.

Material	PMN-0.28PT
Longitudinal velocity v_z (ms^{-1})	4038
Density ρ (kgm^{-3})	7920
Clamped dielectric constant ϵ_{33}^s	621.6
Piezoelectric constant d_{33} (pC/N)	1400
Electromechanical coupling coefficient k_t	0.58
Acoustic impedance Z (MRayl)	32
Thickness (μm)	500

**Figure 5.5** Schematic diagram of the designed phased array transducer.

5.2.3 Modelling of ultrasound transducer

PiezoCAD (Sonic Concepts, Woodinville, WA) is an ultrasound transducer simulation programme based on KLM model which has been presented in Figure 2.11. KLM model can represent the ultrasound transducer in an equivalent circuit mode and simulate its acoustic responses. In the PiezoCAD software, the simulated results of pulse-echo response, frequency response and electrical impedance of the transducer can be predicted based on the input properties of piezoelectric material, matching layer and backing layer.

After all the specification of the transducer has been optimized by PiezoCAD, a finite element method (FEM) software (PZFlex, Weidlinger Associates, Los Altos, CA) was also employed to simulate the beam profile and pressure field of the designed phased array UT. For a phased array transducer beam forming, a phase delay is applied on each element to simulate a pressure field focusing at 4 mm axial depth instead of using a focus lens. Since the focal point is located at the central axis of the phased array transducer and its symmetric structure, 64 elements on one side of the transducer are excited followed by a mirror process to formulate the comprehensive pressure field of all 128 elements. The phase delay of each element is described as follows:

Every element has a time delay $\Delta t(i)$,

$$\Delta t(i) = \frac{\Delta disp(i)}{v} \quad i=1,2,3 \dots N \quad (22)$$

Where $N=64$ (another 64 elements can be handled by a mirror operation), v is velocity of water and $\Delta disp(i)$ is the displacement which can be expressed as following,

$$\Delta disp(i) = \sqrt{x(i)^2 + y_{focus}^2} - y_{focus} \quad (23)$$

Where $x(i)$ is the central position of the i th element, y_{focus} is the focus distance, which is 4 mm. The excitation voltage of i th element is also varied due to its position difference.

The amplitude $u(i)$ of the excitation signal of i th element can be expressed by

$$u(i) = \mu(i)A_0[\omega(t + \Delta t(i)) + \varphi] \quad (24)$$

Where $u(i)$ is the applied voltage, $\omega = 20$ MHz is the frequency, φ is set to be 0, A_0 is the amplitude and set as 1 V in this model, $\mu(i)$ is the weighting factor showing as follows,

$$\mu(i) = 0.25 + \left[\frac{0.75}{2} \cdot \cos \left[\left(\frac{i}{N} \cdot \pi \right) + 1 \right] \right] \quad (25)$$

The simulated pressure field can provide the depth of field of the designed transducer and the estimated lateral resolution value. Besides, the beam profile can illustrate the grating lobe or side lobe profile with or without a steering angle. The information is important for designing an array structure transducer which is not supported by PiezoCAD. Therefore, this FEM simulation is an extremely useful tool for assisting the array or other new structural transducer. The results of all the simulated results will be shown in section 5.3.1.

5.2.4 Fabrication process

After the simulation progress, all the specification has been determined. The transducer then will be fabricated depending on those specification. The phased array transducer can be fabricated followed by the simulated parameters from the simulation. The fabrication steps will be illustrated in point form as the follows,

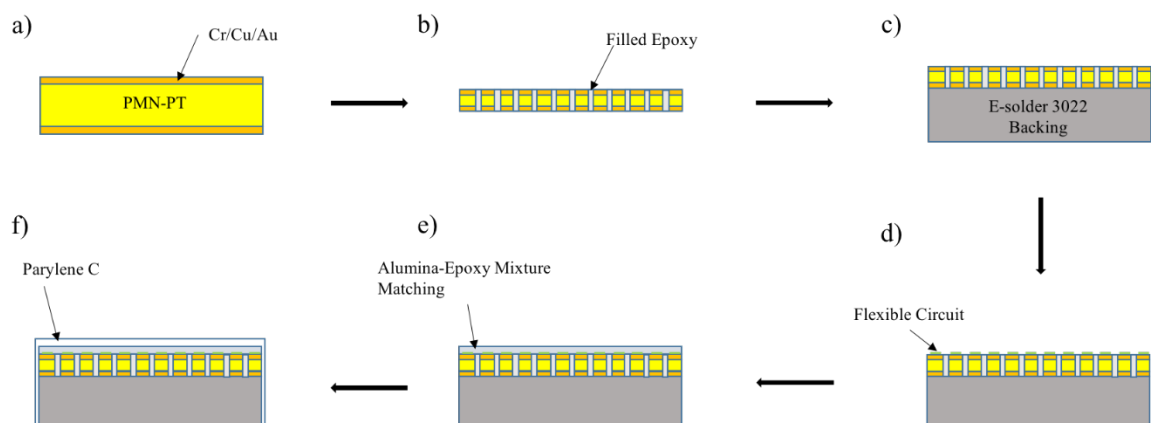


Figure 5.6 A schematic diagram of the fabrication procedure of the high frequency phased array transducer.

1. The PMN-0.28PT specimen plate with a size of $25 \times 13 \times 0.5 \text{ mm}^3$ ($L \times W \times H$) was coated with a Chromium/copper/gold (Cr/Cu/Au, thickness: 22 nm/ 250 nm/

70 nm) trilayer-composited electrode by magnetron sputtering on both sides (shown in Figure 5.6 (a)).

2. A polarization hysteresis loop was determined and shown in Figure 5.7. The coercive field illustrated in the loop is around 0.5 kV/mm. For E-field larger than 1.0 kV/mm the polarization starts to saturate. Thus, for gaining the high polarization of PMN-0.28PT a 1.0 kV/mm polling E-field is selected.
3. The poled specimen was waxed on a glass and further diced by a mechanical dicing saw (model DAD 321, DISCO Co. Ltd., Omori-Kita, Japan) with a ZHZZ-AZ blade. The cutting index was set as 60 μm (0.8 λ pitch). The cutting depth was 150 μm and the dicing speed was 0.4 mm/s. The cutting kerf was around 13 μm which has been shown in Figure 5.8.

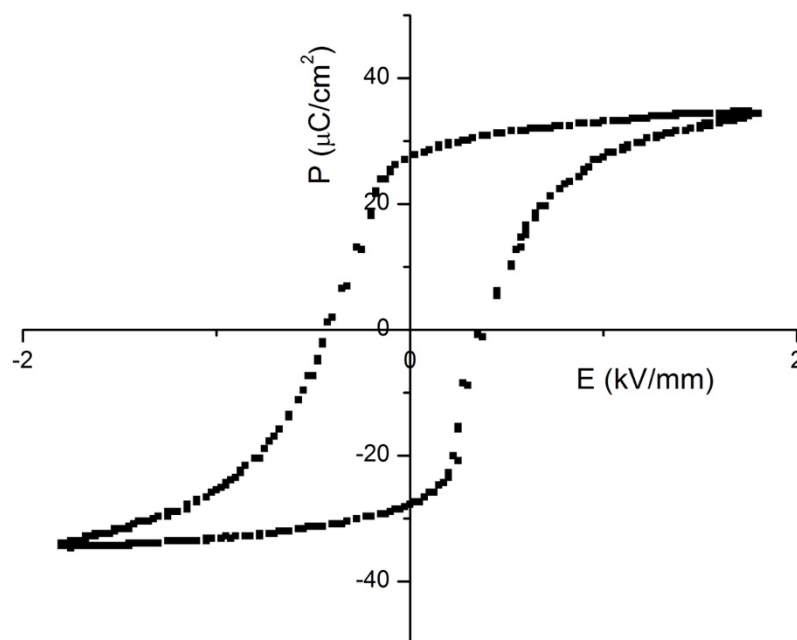


Figure 5.7 Polarization hysteresis loop of PMN-0.28PT.

4. An epoxy (EPO-TEK 301-1) was filled in kerfs by the capillary action. This epoxy was chosen due to its low viscosity which is between 80-100 cPs at room

temperature. The low viscosity can produce a faster capillary action and the air bubbles trapped inside the kerf can be removed more easily.

5. The epoxy was filled over the surface of the specimen and degassed in a vacuum chamber to produce a comprehensive connection between the kerfs and the elements.
6. The epoxy was cured under atmosphere for 24 hours at room temperature.
7. A surface lapping for removing the exceeded epoxy was done. A 4000 grits alumina polishing powder was used to polish the surface to produce a flat surface of the acoustic stack.

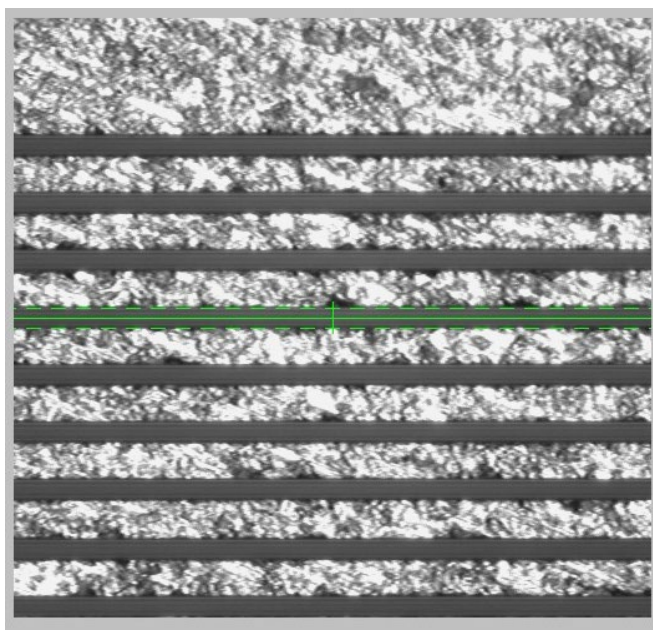


Figure 5.8 The profile of kerfs diced by the mechanical dicing saw.

8. A Cr/Cu/Au tri-layered electrode was deposited on the acoustic stack using an electromagnetic sputtering. The thickness of Cr, Cu and Au are 25 nm, 250 nm and 70 nm, respectively.
9. A sub-dice is required to isolate the electrode on the elements for producing an

array pattern shown in Figure 5.6(b).

10. The array was flipped over and lapped to the required 90 μm thickness. A final polishing same as step 5 was also applied on this side.
11. Step 6 was repeated to sputter an electrode on this side.
12. The E-solder 3022 backing was mixed and filled on the back side. The epoxy was cured under atmosphere for 24 hours at room temperature (shown in Figure 5.6(c)).
13. The array with the backing was lapped to a thickness 2.5 mm. The array was diced into a 5.0 x 8.3 x 2.5 mm^3 cuboid by the mechanical dicing saw.
14. Two custom designed flexible circuits with the trace separation doubled of the array pitch were connected on both edges of the array front surface by M-bond 610 (Micro-Measurements, Raleigh, U.S.A)(shown in Figure 5.6(d)). This is because the narrowest separation of the flexible circuit provided by the manufacturer is wider than the pitch of the array. Otherwise, the electrode traces of the flexible circuit would be shorted internally. The M-bond 610 was cured under a compression by an aluminum fixture in an oven at 65 $^{\circ}\text{C}$ for 3 hours.
15. The first matching layer with the required thickness 42 μm was casted on the front surface of the array with M-Bond 610(shown in in Figure 5.6(e)). Then, a 28 μm thick Parylene C was deposited on the array as the second matching layer by the parylene deposition system (SCS PDS2010E LABCOTER, Specialty Coating System, Inc., USA)(shown in in Figure 5.6(f)).
16. The transducer then was connected to a costumed PCB board. The PCB board was wired to the Verasonics terminal connector by 128 individual 0.5 m length coaxial cables. This modulated design is convenience for replacing the

transducer which is not only useful for research field but also in manufacturing product.

17. An aluminum foil was enfolded on the transducer and mounted inside a plastic shell covering all the wire and component. The assembled transducer is shown in Figure 5.16.

5.2.5 Characterization of acoustic and electrical response of the transducer

All 128-elements' acoustic and electrical responses of the transducer were tested. The acoustic testing including two-way impulse response, insertion loss, crosstalk between the elements. The electrical responses of all elements, including the electrical impedance and capacitance, crosstalk are also characterized in this chapter.

The crosstalk is one kind of noise generated in 1-D or 2-D array transducer. Crosstalk can be divided into two types i.e. mechanical and electrical. In mechanical type, a lateral direction vibration propagating through the transducer is generated when the element is excited by an electrical or acoustic signal. Due to the array structure, this vibration will transfer to the elements located next to the excited elements. A lateral deformation causes a longitudinal deformation, consequently acoustic signal and electrical signal from the adjacent element are generated. These signals will affect the beam forming during the acoustic signal emission and the generated electrical signal when receiving the reflected acoustic signal. The second crosstalk is caused only by the electrical signal. An electromagnetic (E-M) signal will be generated when an AC electrical signal transferring through the circuit. This kind of crosstalk mostly can be eliminated when using the coaxial cable and shielding, but some electrical circuit such as electrodes in flexible circuit and

PCB board is unprotected. Thus, crosstalk may still be exhibited in the transducer.

In the crosstalk measurement, the representative element is connected to a function generator in a water tank, and a high acoustic absorption material is placed in the bottom of the water tank, while the transducer is located more than 100 wavelength away from the bottom for preventing the reflection of acoustic signal. A dual channel oscilloscope is connected to the function generator and an adjacent element of the representative element respectively. A sinusoidal electrical signal with $5 V_{p-p}$ amplitude at a specific frequency generated by the function generator excites the representative element, then a relative electrical signal can be received from the adjacent element. The input V_i and received V_o signal are displayed on the oscilloscope. The crosstalk is calculated using equation (19). The frequency-dependent crosstalk curve afterward can be determined by swapping the frequency of the electrical signal.

5.2.6 Biomedical imaging demonstration

After measuring the acoustic performance of the phased array transducer, an image acquisition needs to be implemented to show its imaging ability. The imaging ability measurement includes resolution determination and biomedical tissues imaging. The resolution determination can be trailed through the wire phantom imaging. In the measurement, a high acoustic reflective material wire such as tungsten are arranged in a periodical separation in axial and lateral direction. Due to the high reflectivity of the object, multiple bright spots are acquired in the image to show the resolving powder at different depth level of the transducer. Additionally, by analyzing the intensity of the bright spots, the image resolution along axial and lateral directions at different depth can also been determined. In the wire phantom measurement, the transducer was connected

to the Verasonics system (Vantage128™ Advantage, Verasonics, Inc., Kirkland, WA) through a UTA 156-U connector. The system uses 128 Tx/ 128 Rx channels transferring RF signal between the transducer and the host. The maximum frame rate is up to 100,000 frames/s depending on the acoustic signal travelling distance and beamforming method. The system using a 14-bit analog-to-digital convertor to convert the obtained electrical pulse signal, therefore, the processed image has 16384 grayscale levels per pixel. The host system's sampling rate is set as 62.5MHz. The ultrasound beam steering and data collection are controlled by a customized MATLAB program. Figure 5.7 illustrates the wire holder which contained a series of tungsten wires with 20 μm diameters. Those tungsten wires are attached on the holder with 0.8 mm and 0.5 mm of axial and lateral separation respectively. The whole setup and the phased array transducer were immersed in the water during the measurement. The phased array transducer was located upon the first wire with a distance of 4 mm.



Figure 5.9 Picture of the tungsten wires holder.

In the biomedical imaging demonstration, a biological object is chosen. Depending on the object, the imaging can be stated as *in-suit* and *in-vivo* imaging. However, mostly of the demonstration is replacing the biological object by an artificial phantom. However, the dynamic object imaging ability cannot be stated while using the artificial phantom.



Figure 5.10 The setup of the rat cardiac ultrasound imaging.

In the biomedical imaging demonstration, the performance of not only the transducer but also the imaging system platform can be shown simultaneously. In this thesis, both of the *in-suit* and *in-vivo* imaging demonstration is implemented to show the static and dynamic imaging ability of the developed transducer. According to the small scaled imaging purpose, a 10 mm diameter eye of a ctenopharyngodon idella was chosen to demonstrate the static imaging. The transducer connected on the Verasonics platform was mounted by a fixture and contacted with the fisheye. An acoustic gel was filled between the eye and the transducer.

On the other hand, in *in-vivo* imaging demonstration, a laboratory rat cardiac imaging was acquired to show the phased array transducer high frame dynamic imaging ability. The *in-vivo* demonstration setup is similar to the *in-situ*, a rat in coma with its chest hair removed was hold in a table and the transducer was placed on the left chest. The setup is shown in Figure 5.8. The lateral direction of the phased array transducer was parallel to the rat's head direction. Acoustic gel was also filled in the gap between the transducer and the chest.

5.3 RESULTS

5.3.1 *Simulation Results*

Based on the requirements of the proposed research, the center frequency of the phased array transducer was 20 MHz and the acoustic impedance of the front-loading medium was assumed to be 1.5 MRayl because the loading medium was water. For the soft biomedical tissue, the acoustic impedance is around 1.5 MRayl to 2.0 MRayl. Thus, water was chosen as a medium for evaluating the performance of ultrasound transducer for medical imaging application. Actually, water can also be selected for the back loading medium in some cases. Nevertheless, in this project, the acoustic impedance of backing layer was selected to be the back loading medium. The ideal backing layer should have an extremely high attenuation and relatively thick thickness to absorb nearly all the back-side reflection. In such case, no reflection occurs from the back side, so the thickness of the back side medium is considered to be infinity. After selecting the frequency range and the loading conditions, the required parameters of all layers were input in the software. The measurement of piezoelectric parameters of material is illustrated in section 5.2.1. The required thickness of the piezoelectric material was theoretically calculated by equation (7) and experimentally measured by the thickness gauge (Model C112XB, Mitutoyo Corp., Japan). The thicknesses of the double matching layer were estimated using the quarter wavelength theory. The aperture size was set as the size of single active element based on the design. After inputting all the parameters, the PiezoCAD will display the two-way acoustic response and the electrical response of the designed transducer. By fine tuning the thickness of various layers and aperture size, the optimized result can be estimated.

The simulated acoustic and electrical results by PiezoCAD are shown in Figure 5.11 and

Figure 5.12, respectively. All the specification of the designed phased array are shown in Table 5.2 and Table 5.3, respectively.

TABLE 5.2 PROPERTIES OF DIFFERENT ACOUSTIC LAYERS.

Matching layer number	1	2	Backing layer
Material	2-3 μm Al_2O_3 powder + Epoxy 502	Parylene C	E-solder
Weight ratio	2:1	N/A	N/A
Acoustic impedance ($M\text{Rayls}$)	8.54	2.6	5.9
Velocity (ms^{-1})	3552	2350	1850
Density (kgm^{-3})	2405	1100	3200
Thickness (μm)	42	28	2000

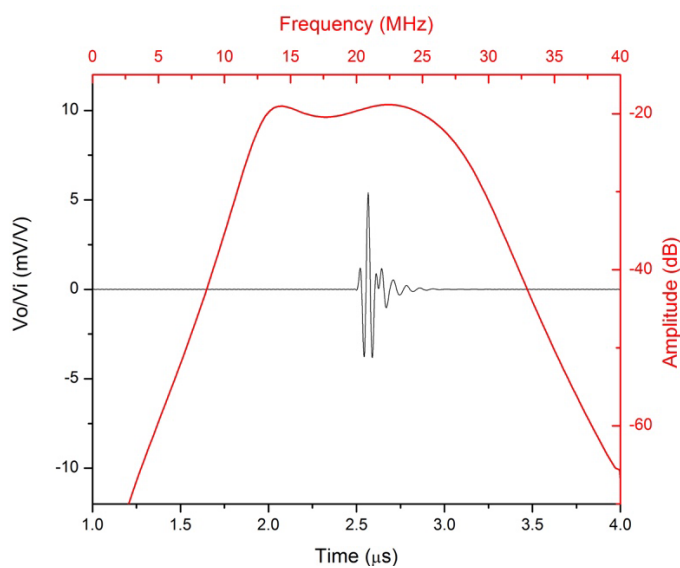


Figure 5.11 Simulated pulse-echo (black) and frequency (red) spectra.

A predicted 15.9 MHz -6 dB bandwidth, which is 80.5% in percentage, is analyzed from the simulation result. This result is higher than other published phased array and linear array in high frequency range^{56,72,111,112}. The -6 dB center frequency is 19.9 MHz and

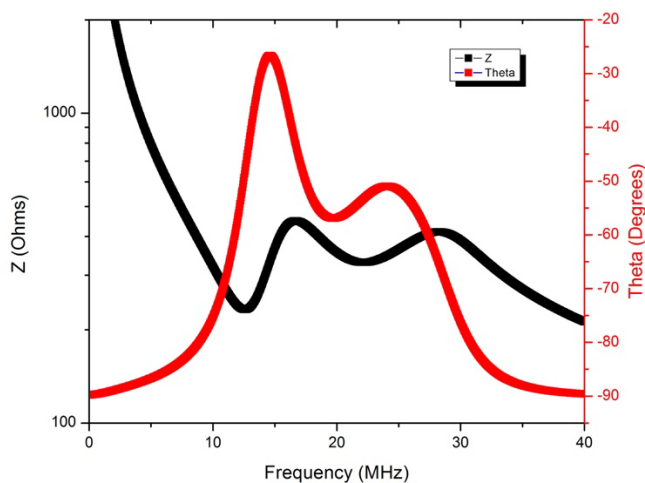


Figure 5.12 Simulated electrical impedance (black) and phase angle (red) spectra.

TABLE 5.3 LIST OF THE DESIGNED PHASED ARRAY'S SPECIFICATIONS.

Designed center frequency	20 MHz
Number of elements	128
Pitch	60 μm (0.8 λ)
Elements width	45 μm
Elements length	5 mm
Elevation dimension	2.16 mm
Azimuthal dimension	7.68 mm
Kerf width	15 μm
PMN-0.28PT thickness	90 μm
First matching layer thickness	42 μm
Second matching layer thickness	28 μm
Backing layer thickness	2 mm

the predicted electrical impedance is 367 Ω at 20 MHz. The calculated axial and lateral resolutions using the pulse length and beam width are around 46.5 μm and 54.4 μm , respectively. Figure 5.13(a) shows a part of the input 2-D model of the phased array transducer. All the layer parameters and dimensions are based on the simulated results of the PiezCAD. Figure 5.13(b) shows the pressure field result of the model in water. The water medium in the simulation is 7.71 mm lateral width and 8 mm depth on the front

side of the UT. In the pressure field result, the focus point has been set at 4 mm and the acoustic pressure along lateral and axial direction of it has been illustrated in Figure 5.14(a) and (b). The maximum pressure at 4 mm is around 221.7 kPa. According to the lateral beam shape showing in Figure 5.14(a), the -6 dB lateral beam width can be stated as 136 μm , thus the resolution can be stated as 68 μm . The -6 dB axial beam depth can also be seen in the Figure 5.14(b). This -6 dB depth is not representing the axial resolution of the transducer since the axial resolution of the transducer depends on the pulse length. This depth representing the depth of field of the transducer at 4 mm focal distance

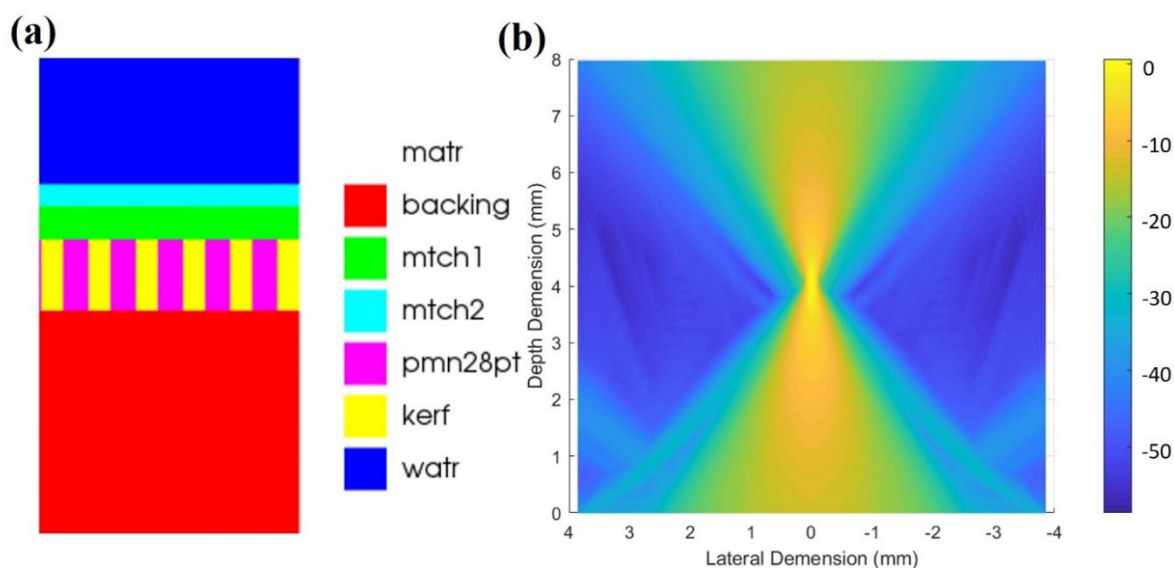


Figure 5.13 (a) The 2-D model inputted to the FEM software PZFlex and (b) the simulated 2-D acoustic pressure field of the 2-D phased array ultrasound transducer in water.

which is around 1.04 mm. The estimated axial resolution of the pulse can be found from the acoustic profile along the time domain which has been shown in Figure 5.15(a). The -6 dB pulse length in the graph is 80 ns. The simulated two-way frequency spectrum has been calculated using the fast furious transform function. The result is shown in Figure 5.15(b). The frequencies at -6 dB amplitude are 10.02 MHz and 26.35 MHz, indicating a 16.33 MHz bandwidth. Thus, the simulated axial resolution is 45.3 μm by assuming the acoustic velocity of water as 1480 ms^{-1} .

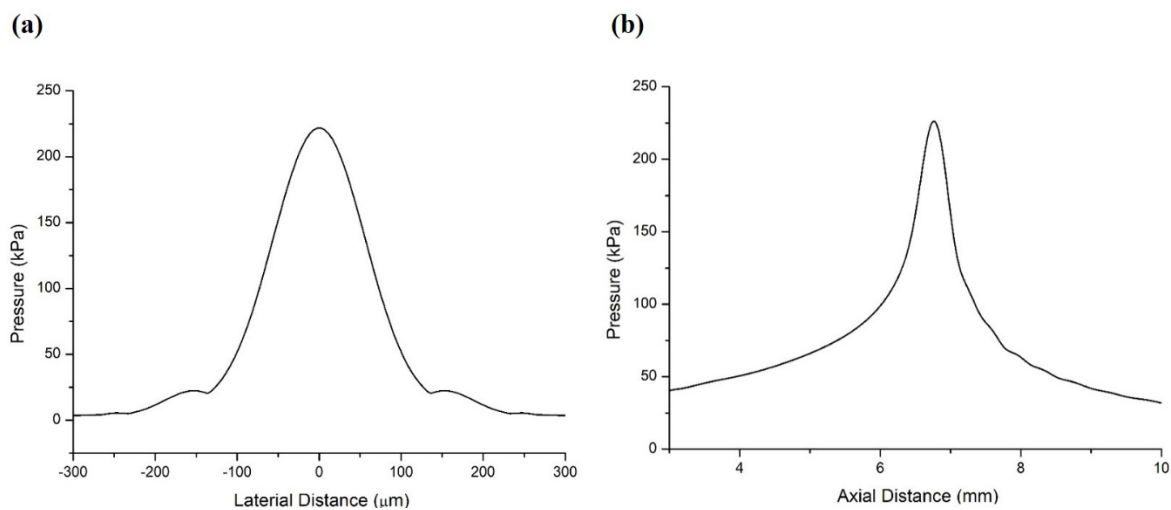


Figure 5.14 The pressure field along (a) lateral direction and (b) axial direction.

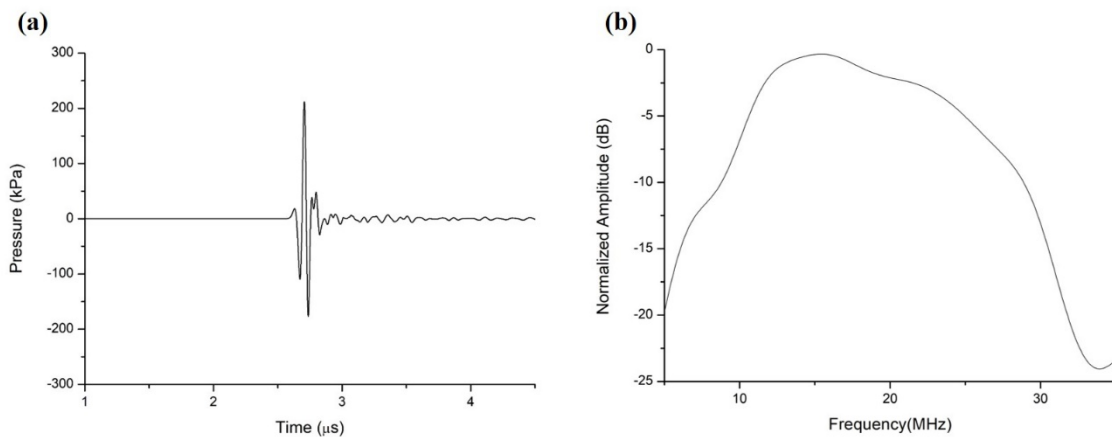


Figure 5.15 (a)The simulated acoustic pressure at 4 mm focal distance across time and (b) the simulated two-way frequency spectrum of designed phased array transducer.

In summary, the simulated center frequency of the phased array UT is around 19.05 MHz averaged by both of the simulation software. Besides, the resolution of axial and lateral based on voltage or pressure response are estimated as 45.3 μm and 68 μm , respectively. The estimated center frequency and axial resolution in both simulation methods only show a slightly difference. Lateral resolution calculated by equation (8) is based on intensity response which should be 54.4 μm when it is a pressure response. The difference between the PZFlex and calculated is obverse which is around 20%. Lateral resolution

estimated by PZFlex is more reliable due to the PZFlex simulation considers the excitation voltage variant applied on each element which coherences to the excitation electrical signal in the wire phantom, *in situ* and *in vivo* imaging measurements. Therefore, the designed transducer should have a center frequency within 18 MHz to 20 MHz, and the axial and lateral resolution should be around 45.3 μm and 68 μm , respectively. This estimated image resolution should be enough to resolving the detail of small animal's organs or tissues.

5.3.2 Acoustic and Electrical Response

The developed phased array transducer is shown in Figure 5.16. The measured insertion loss of all 128 elements have been investigated and shown in Figure 5.17. In the insertion loss graph, 6 of 128 elements (elements #1, 3, 5, 51, 104 and 128) has a much higher insertion loss than the average value. These elements may have a disconnection feature caused by the separation of flexible circuit. The separation of flexible is also appeared in other elements such as elements #6, 8, 10, 12 and 14. These 5 elements shows a higher insertion loss than average values but not the same value as the open-circuited elements, meaning that those elements has noncomprehensive connection to the flexible circuit. On the other hand, 8 of 128 elements (elements #59, 60, 66, 67, 112, 113, 114 and 115) show their insertion loss value are 6 dB more than the average. At the same time, those elements are all adjacent elements, suggesting that short circuit of these elements. As illustrated above, 109 out of 128 elements have the same value of insertion loss which can be stated as successful elements. According to the calculation, the yield rate of the developed array is around 85%.

The electrical response of the array has also been measured. Figure 5.18 and Figure 5.19

show the results of electrical impedance-phase angle and capacitance-loss of all functional elements, respectively. The results show a high uniformity of the insertion loss. A 401Ω electrical impedance is found at 20 MHz frequency in Figure 5.18. The value is slightly higher than the simulated result of PiezoCAD. The relatively higher impedance was possibly caused by the electrical influence of the backing layer and the matching layer attachment. The peak value of the phase angle change is located at 17.2 MHz roughly inducting the center frequency of the transducer. Unfortunately, this value is

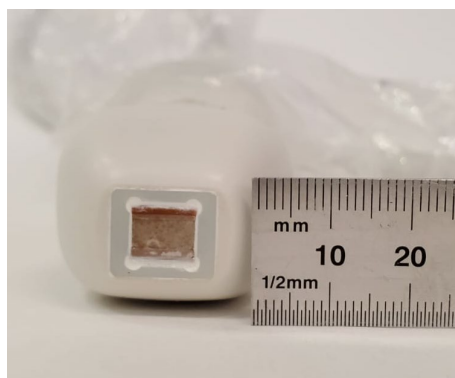


Figure 5.16 Top view of fabricated phased array transducer.

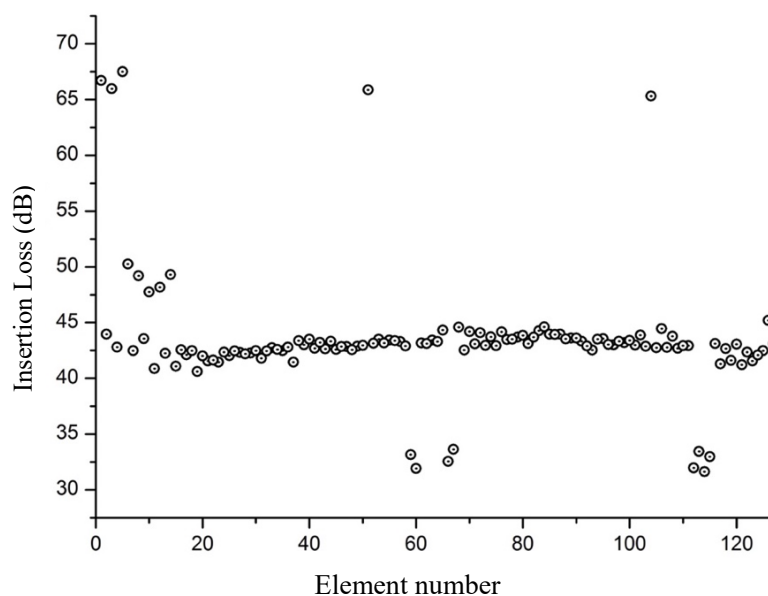


Figure 5.17 Insertion loss of all 128 elements.

slightly lower than the simulation result. Same phenomenon can also be found in the Figure 5.19. The peak of the electrical loss is located at 17.3 MHz which is similar to the phase angle result. The average capacitance of the developed array at 20 MHz is

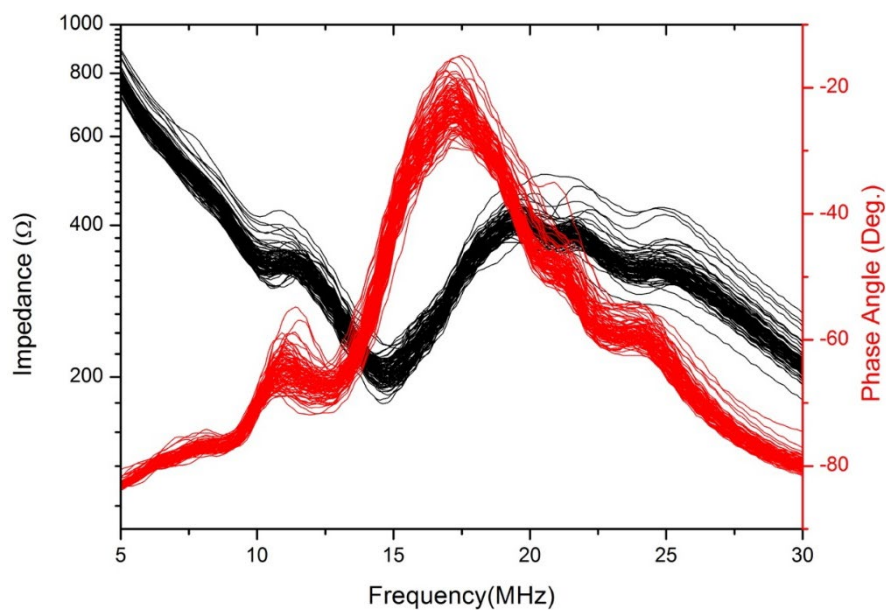


Figure 5.18 Electrical impedance (black) and phased angle (red) of all functional elements.

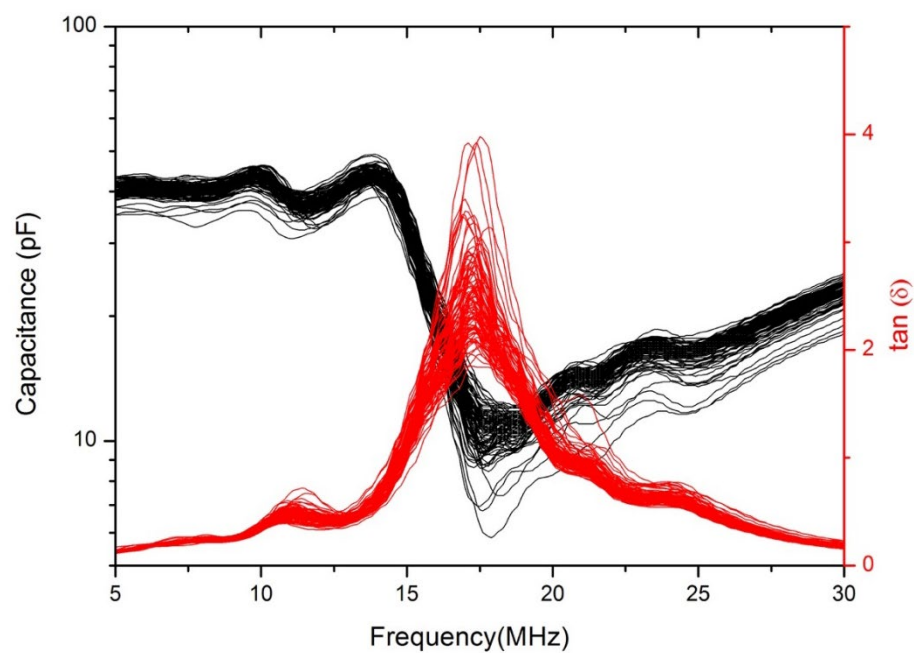


Figure 5.19 Capacitance (black) and loss (red) of all functional elements.

13.22 pF. This value matches the expected capacitance calculated using the clamped dielectric constant and the aperture of the element. All the important data of the electrical responses have been summarized in Table 5.4.

TABLE 5.4 MEASURED ELECTRICAL IMPEDANCE AND PHASE ANGLE PROPERTIES OF A REPRESENTATIVE ELEMENT.

Peak of phased angle f_p (MHz)	17.3
Impedance (Ω)	401@20 MHz
Resonance frequency f_r (MHz)	14.71
Anti-resonance frequency f_a (MHz)	19.57
Effective coupling coefficient k_{eff}	0.70

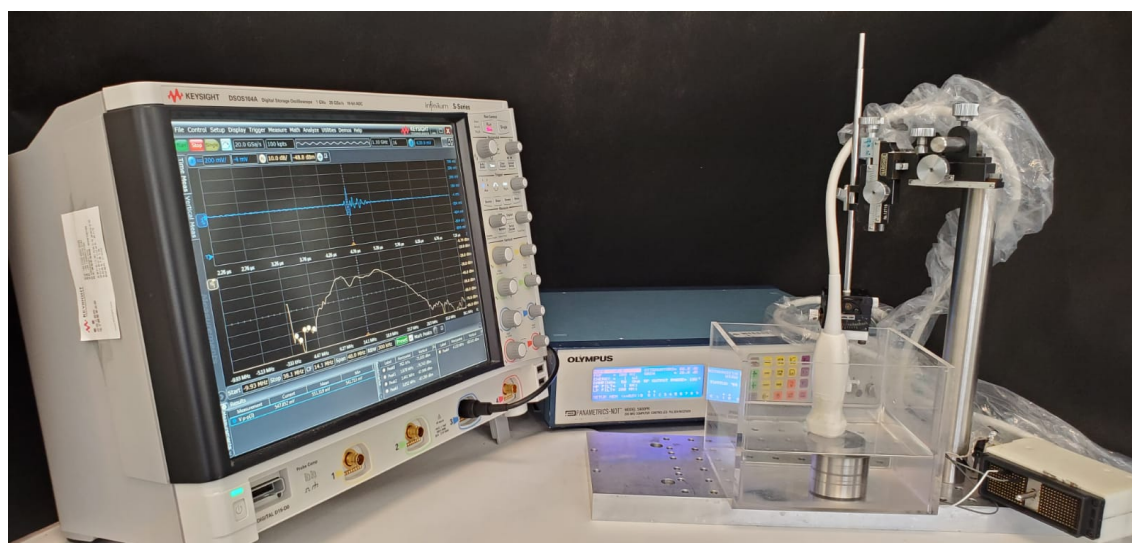


Figure 5.20 The setup of the two-way impulse measurement.

The setup of the pulse-echo measurement is shown in Figure 5.20, and Figure 5.21 shows the pulse-echo response of the phased array as a superposition and waterfall format. The averaged peak to peak amplitude of the obtained acoustic signal of the two-way pulse echo is $1.23 V_{p-p}$ gained 26 dB by the pulser receiver. The waterfall graph shows that the signal of the successful elements has an extremely high uniformity at the mainly pulse.

The pulse-echo waveform shows a slight ring-down after the first period, which remains in the following two periods with a continuous amplitude reduction. This ring-down is believed to be due to the insufficient absorption to the acoustic energy by the backing

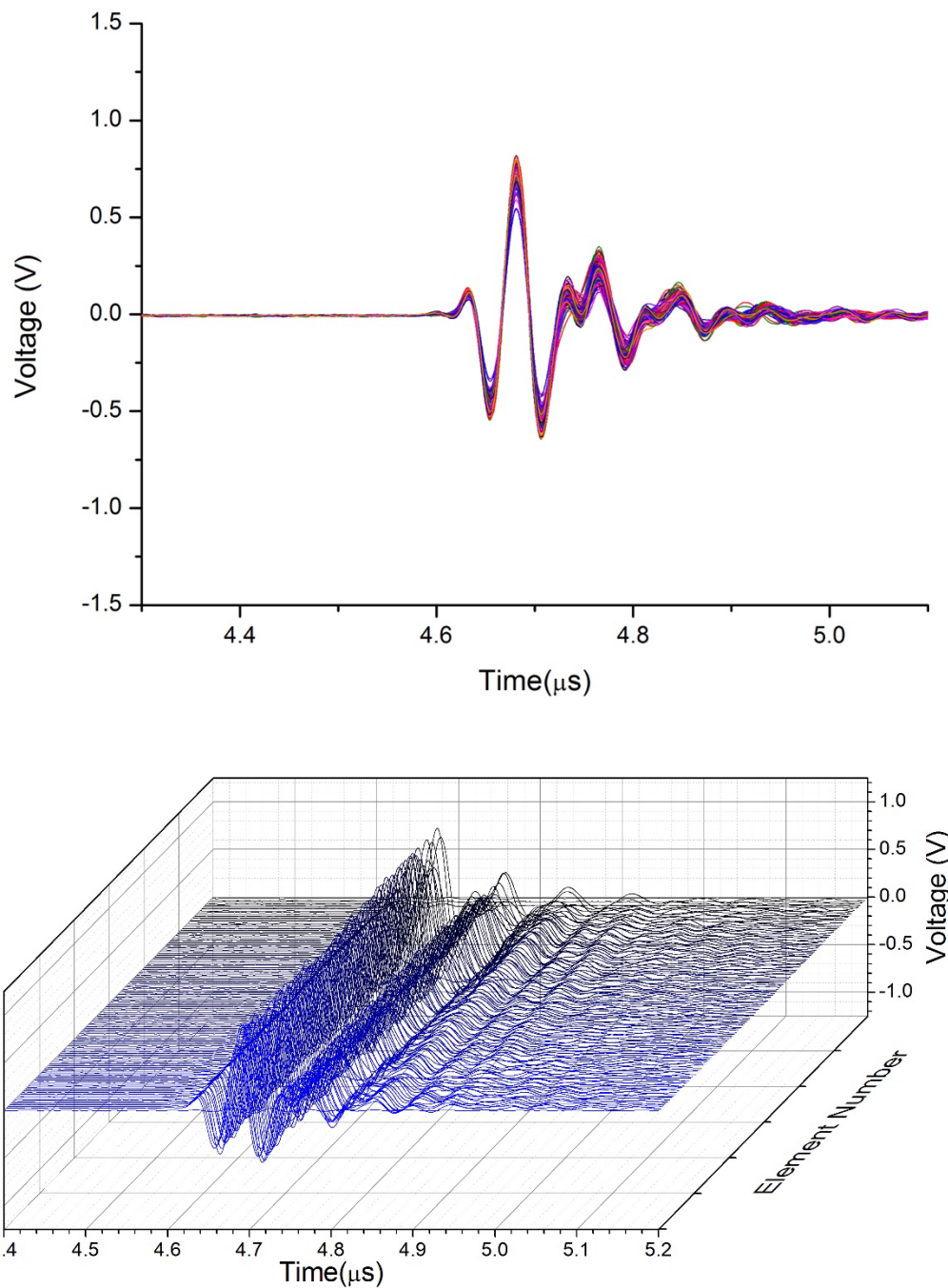


Figure 5.21 Pulse-echo waveforms of all functional elements displayed in superposition (Top) and in waterfall (Bottom).

layer^{30,32 86}. The amplitude of ring-down is lower than -6 dB so this ring-down does not affect the bandwidth of the phased array transducer theoretically. This is supported by the spectrum result showing in Figure 5.22. The measured -6 dB points in the spectrum results

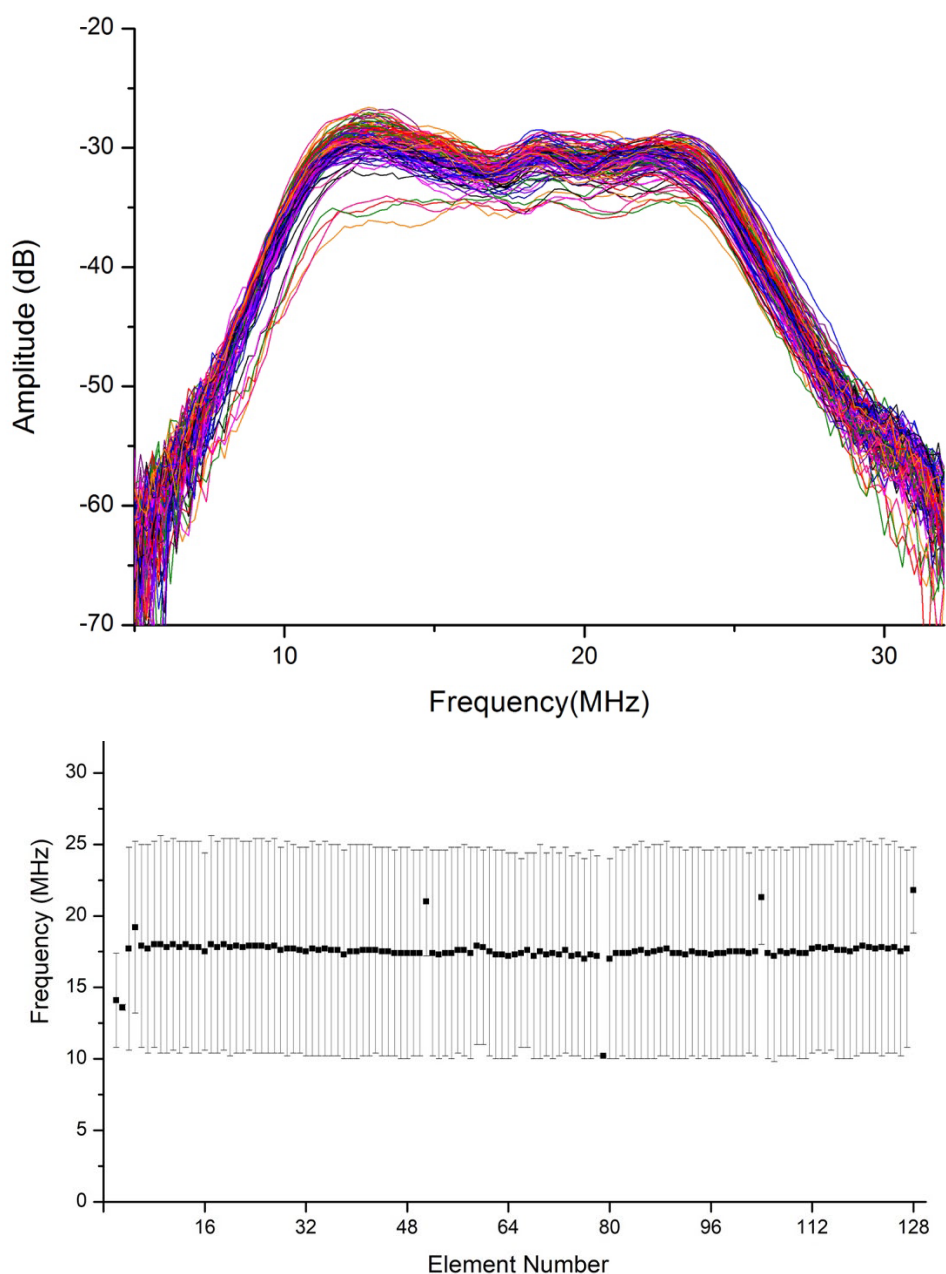


Figure 5.22 Frequency response spectra of all functional elements displayed in superpositioned (Top). The center frequency and -6 dB bandwidth of all 128 elements (Bottom). The center frequency is represented by the square dot. Upper and lower -6 dB frequencies are represented by the error bar.

are 10.0 MHz and 24.7 MHz which means the bandwidth is 14.7 MHz. According the Figure 5.22 and calculation, the average -6 dB center frequency of this acoustic response is 17.4 MHz. Thus, the bandwidth in percentage is 84%. Similar to the time domain response, the uniformity of the frequency spectrum is high as shown in Figure 5.22 (bottom). The shape of the measured signal in time domain matches the simulated result from PZFlex but the amplitude of the main pulse is slightly lower which makes the ring-down larger than the expectation.

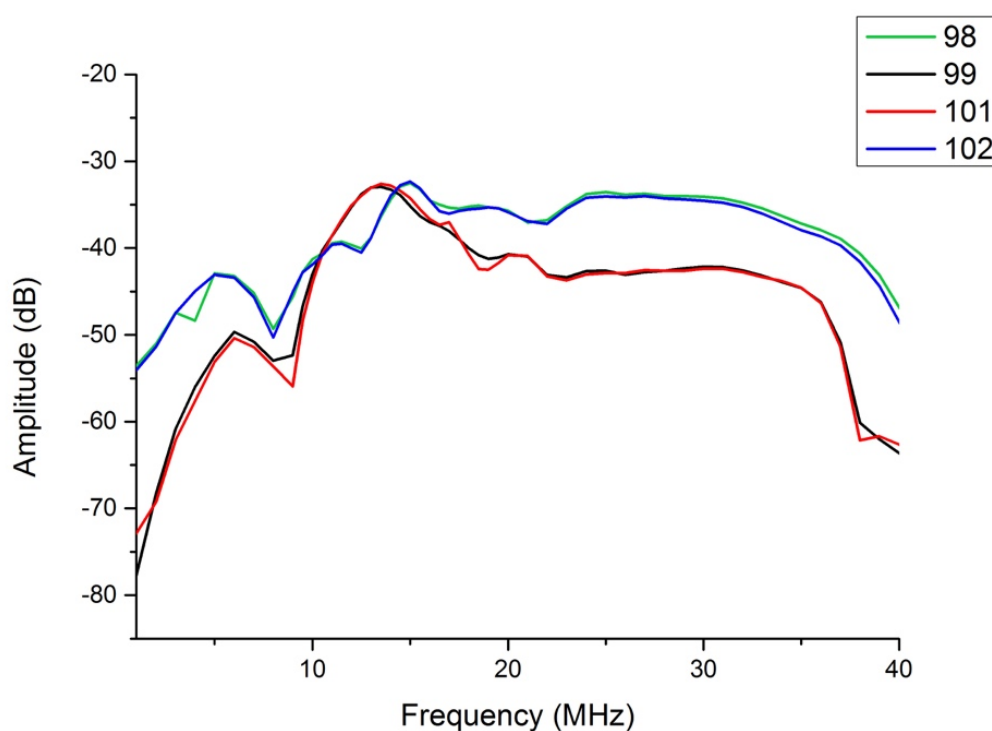


Figure 5.23 Crosstalk of adjacent elements (left and right sides) and one more next to the adjacent elements (left and right) of element #100.

A representative element is chosen for testing the crosstalk phenomena of the developed UT. Due to the high uniformity, the element was randomly pick without concerning any of the signal amplitude. The corsstalks between the representative element #100 and its adjacent elements (both left and right sides, #99 and #101) and one more element next to

the adjacent elements (#98 and #102) are showing in the Figure 5.23. The adjacent elements on both sides of the representative showing a coherent crosstalk within the frequency range from 0 to 40 MHz. This coherent also appears in the crosstalks of one next to the adjacent element. According to the adjacent crosstalk curve, a relatively higher crosstalks value is illustrated within 10 to around 37 MHz which matches the operation frequency range of the array UT. Therefore, for frequencies out of the operation frequency range, the crosstalks show a shape value decrease down to minimum -75 dB. Within operation frequency range the adjacent elements show an average -45 dB crosstalk and a -32 dB maximum crosstalk located at around 11.5 MHz.

5.3.3 Medical Imaging Measurement

5.3.3.1 Wire phantom measurement

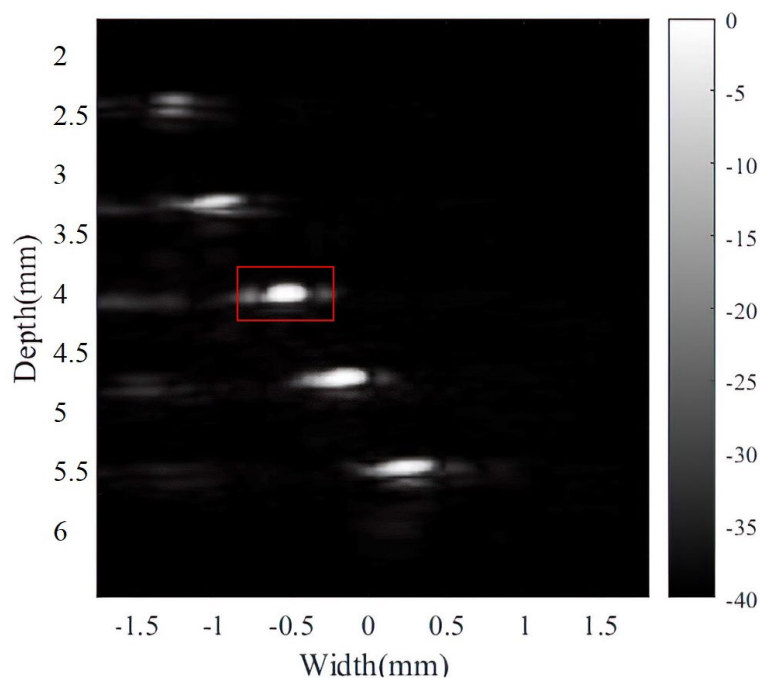


Figure 5.24 Wire phantom image of 20 μm tungsten wires.

A phantom wire measurement was carried out to determine the resolutions of the developed phased-array transducer. Figure 5.24 shows the measured image of five 20 μm -diameter wires with 0.8 mm and 0.5 mm of axial and lateral separation respectively. The vertical and horizontal dimensions of the image represent the axial and lateral

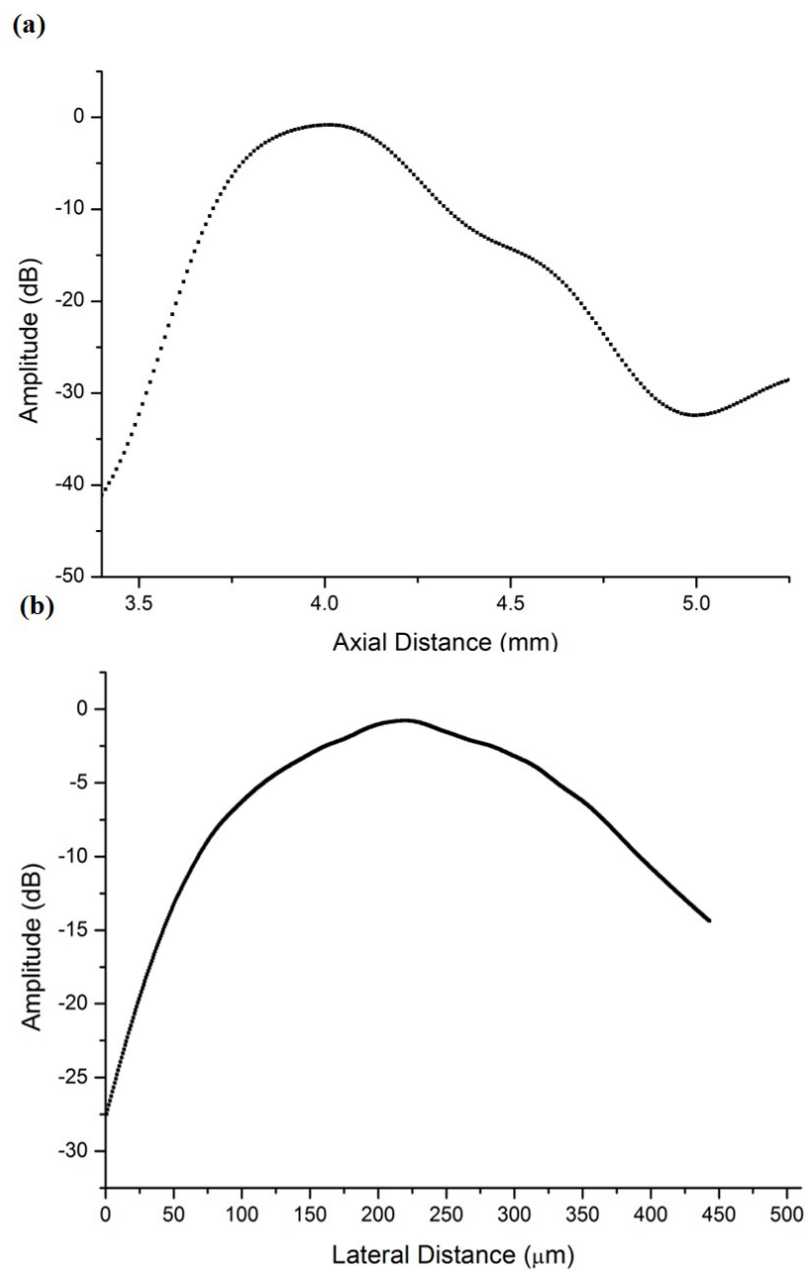


Figure 5.25 Brightness intensity of the representing spot in the wire phantom image (Figure 5.24) along the (a) axial and (b) lateral directions.

responses of the transducer, respectively. The axial and lateral signal intensities of the central spot are illustrated in Figure 5.25. The 40.5 μm axial and 121.5 μm lateral -6 dB resolutions were obtained from the 20 μm tungsten wire corresponding to measured dimension distance between the -6 dB (half of the maximum value) amplitudes. By comparing with the simulated results presenting in Figure 5.14, Figure 5.15 and Figure 5.25, the measured -6 dB lateral resolutions are lower than the simulated results which is 68 μm .

5.3.3.2 Biomedical imaging acquisition

A tissue imaging measurement has been accomplished in this thesis for examining the resolving power of the developed phased-array transducer. A 10 mm diameter eye of a ctenopharyngodon idella was chosen to be the target of this imaging demonstration. The *in-situ* captured imaging and the corresponding structures of the eye which is labeled based on the eye sketch reported by Walls *et al.* and Fernald *et al* are showing in Figure 5.26^{113,114}. In the obtained image, the cornea, including autochthonous layer, scleral layer and dermal layer, lens and retractor lentis were captured and indicated. Retina is also captured by the imaging process but the fine structure of it was not illustrated clearly due to the attenuation is proportional increased along the axial direction. According to the captured image, the signal to noise ratio is high so that the outline of the image seems a bit blur and unclear. Some factors such as, the electrical impedance coupling, noise generated along the cable or side-beam effect may consequence low signal to noise ratio. The electrical impedance of the array elements are 6 times higher than the operation system which cause a high electrical energy loss between the array and the system. Thus, the signal to noise ratio is lower than single element transducer with same center frequency.

To demonstrate the dynamic imaging ability of the developed transducer, an *in-vivo* imaging was also performed with a rat in coma. The image cropped from the real-time video of a 15 mm length rat heart is shown in Figure 5.27. From the image, the outline of the pulmonary artery and the right atrium is presented, and the shapes of the superior and interior vena cava are also illustrated. Besides, the movement of the right ventricle and

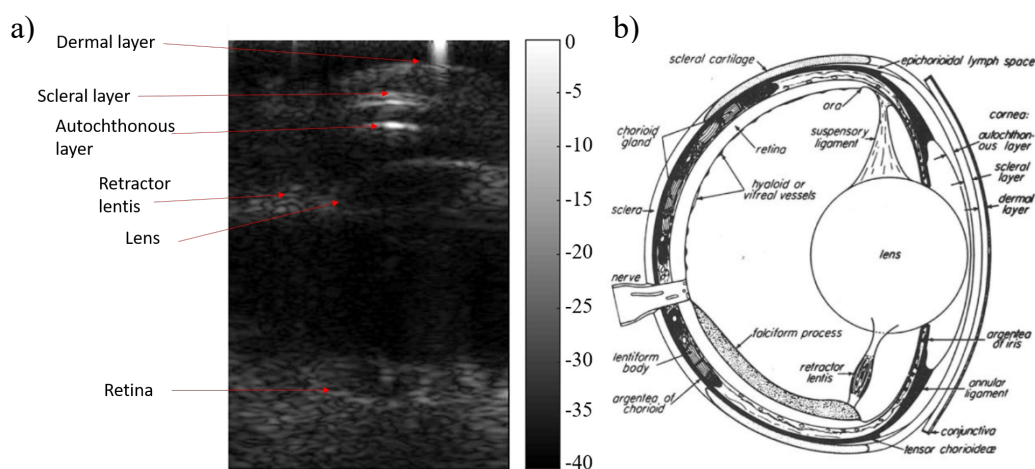
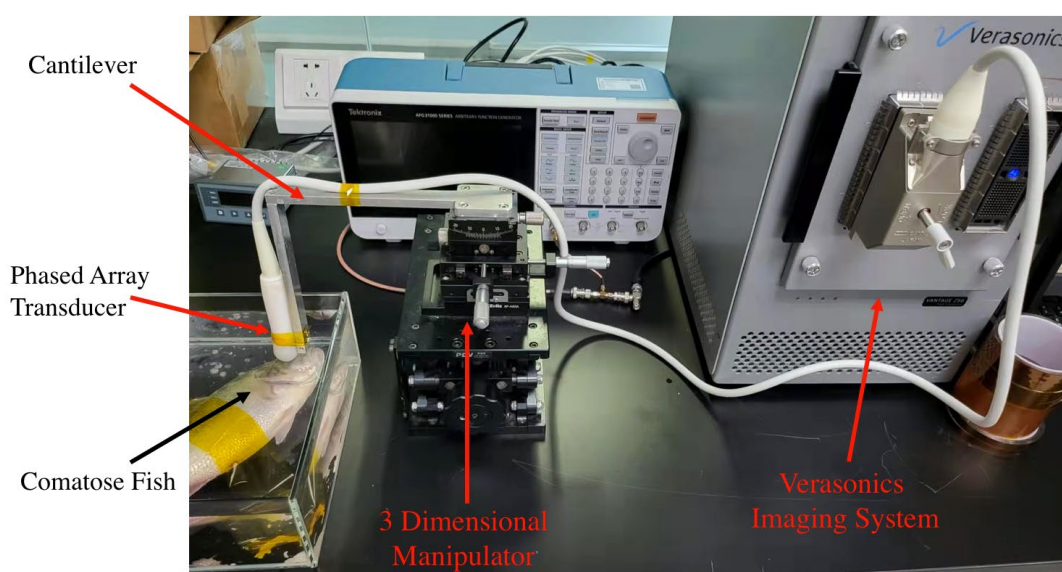


Figure 5.26 The *in-situ* imaging setup (Top). (a) The *in-situ* captured image by the phases-array ultrasound transducer and the structure image of fish eye^{113,114}.

the right atrioventricular can also be observed from the *in-vivo* recorded video. However, the *in-vivo* imaging is not as clear as the image produced by VisualSonics⁷². It is possible that the signal amplitude has been reduced by the ribs' interruption since the lateral dimension of the developed transducer is larger than the rib bones' separation. Concurrently, many

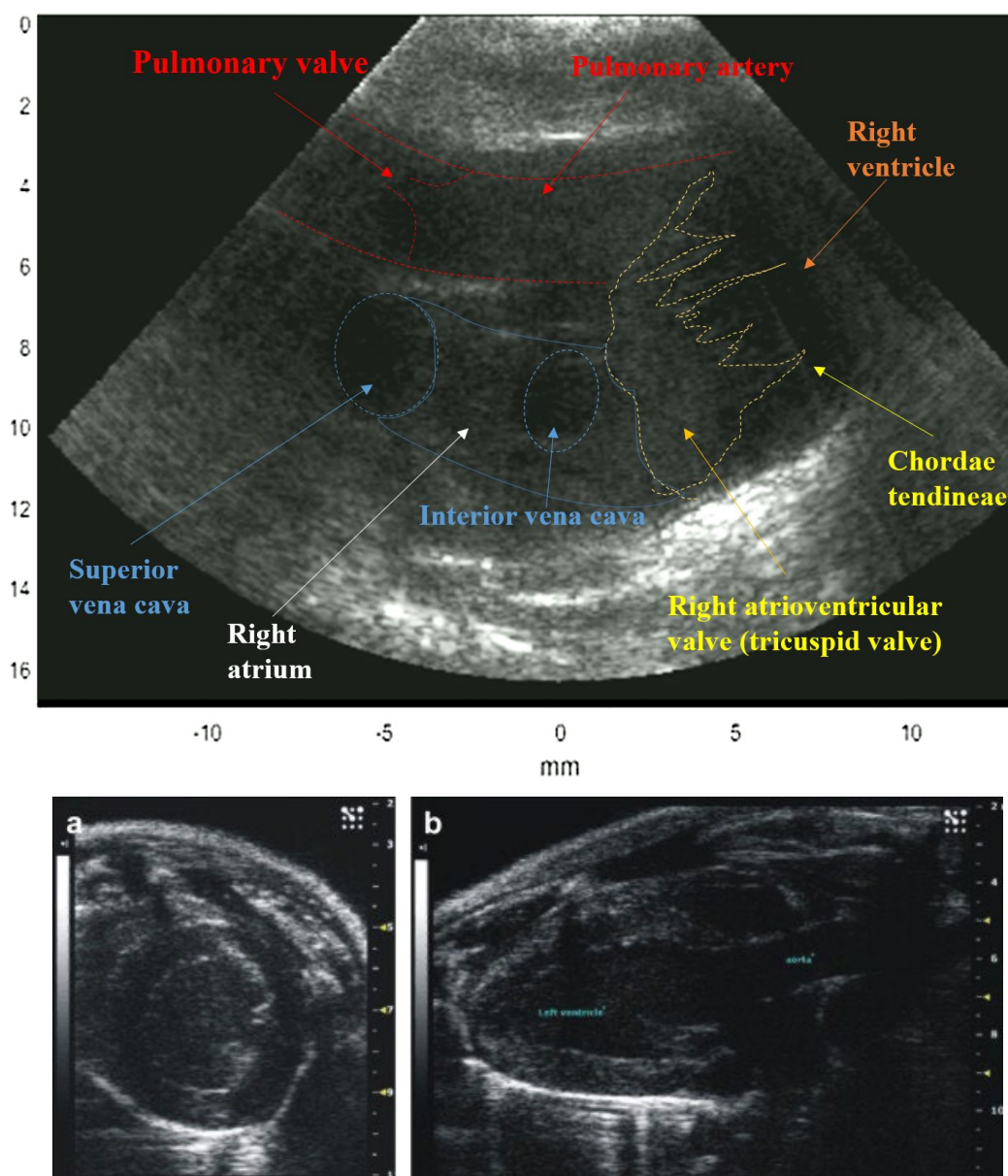


Figure 5.27 A cropped brightness image of the *in-vivo* imaging of a rat's heart captured by the developed phased array ultrasound transducer (Top), and the rat cardiac image captured by VisualSonics's high frequency ultrasound imaging system (bottom).

factors, such as the electrical impedance coupling, noise generated along the cable, etc., may affect the signal-to-noise ratio of the images. Due to the narrow pitch of the elements, the electrical impedance of the array elements are six times higher than that of the operation system, resulting in electrical energy loss in the transfer between the array and the system. Besides, the side lobe and grating lobe generate an unwanted echo scattered by objects located at the side lobe region. This echo produces a pseudo image along the lateral direction resulting in a lower lateral resolution like image¹¹⁵⁻¹¹⁷. Therefore, it is apparent that the image outline along the axial direction is much sharper and clearer when compared to the lateral direction. This artifact can be reduced by apodization but through tradeoff with the beam width increment^{7,116,118}. Further algorithm optimization is required to improve the image quality. Nonetheless, the results demonstrate that our developed phased-array transducer could be used for small animal imaging.

5.4 DISCUSSION

TABLE 5.5 MEASURED RESULTS IN THE PULSE-ECHO WAVEFORM AND FREQUENCY RESPONSE SPECTRUM OF A REPRESENTATIVE ELEMENT.

	Measured	Simulated (PZFlex)
Center frequency f_c (MHz)	17.35	18.19
Peak to peak amplitude	1.38(V)	387.15(kPa)
f_L (MHz)	10.11	10.02
f_H (MHz)	24.98	26.35
-6dB Bandwidth (%)	84.8	89.9

Table 5.5 lists the main data of the acoustic response. The 17.35 MHz center frequency matches the estimated center frequency depending on the electrical response data which is 17.35 MHz. However, the frequency is slightly lower than the simulated 19.9 MHz by

PiezoCAD and 18.19 MHz from PZFlex. PZFlex has illustrated a closer result to the measured value which means its result of pulse profile is more reliable than the PiezoCAD. However, PiezoCAD is still a main pre-simulation program for estimating the specification of the transducer which is an indispensable process for fabricating a UT.

The discrepancy between the simulation and evaluation result is possibly attributed to physical geometry difference of the developed array¹¹⁹, medium parameter difference and the algorithm uncertainty. In geometry of the developed phased array, the existence of an ultra-thin extra adhesive layer exists between the first matching layer and the array surface may be considered a reason causing the frequency incoherence. However, A finding by Shen *et al.* in 2021 has shown a coherence improvement between the simulated and evaluated results based on algorithm correction although the adhesive layer exists in the interface between matching layer and piezoelectric layer¹²⁰. Therefore, the adhesive layer with thickness tremendously narrower than those main layers should have a negligible perturbation on the acoustic response. The thickness variant of all main layers has a higher distribution to the center frequency shifting. On the other hand, both simulations and the experimental measurement are using the same medium and condition. The attenuation and diffraction of water in experiment consists to the input parameter in the simulation software. The variation attributed to the medium parameter mismatch is also negligible. In summary, the frequency discrepancy between simulation and experimental result is mainly caused by the thickness variant in multiple layers and the uncertainty of simulation algorithm. But the 0.84 MHz shifting, which is only -4.84% errors, is still acceptable at such frequency range.

The ring-down of the pulse-echo response can be further improve if the backing layer has a higher acoustic impedance or attenuation. However, using a heavy metal powder mixed

with epoxy is possibly the only way to fabricate a conductive backing layer. The acoustic impedance and attenuation of developed backing using this method can be controlled through the powder material nature, powder size and the ratio of particle to epoxy. The relationship between the acoustic impedance and weight ratio are illustrated in above section 3.3.2. The particle size is controlling the scattering of acoustic wave at specific frequency. For particle size larger a lot than the acoustic wavelength, the acoustic wave will be reflected rather than backing and getting attenuated. For particle size is slightly smaller than the wavelength of the ultrasound signal, a directional scattering acquires that the strength of the ultrasound can be scattered inside the backing and passing with a long path causing a high attenuation. According to this, customized mixture backing layer has higher flexibility or more targeting absorption of specific frequency. Therefore, a more effective back reflective acoustic wave absorption maybe illustrates. The only uncertainly of this method is that the conductivity of customized mixture normally is incomparable to E-solder 3022 which may cause a higher electrical impedance that lower the signal response.

As showing in Figure 5.22, the amplitude at 11 MHz is outstanding comparing with others frequency. For using the customized backing, this frequency can be targeted and reduced to further widen the bandwidth. Even though the developed transducer exhibits a relatively long ring-down, the -6 dB bandwidth is around 85% which is higher than the reported 80 % of the PZT linear array for biological medical imaging developed by Foster *et al.*^{72,111}. Besides, the developed phased-array transducer has a higher uniformity and average -6 dB bandwidth than others PMN-0.28PT based array transducer, such as the 35 MHz PC-MUT 1-3 composited PMN-0.28PT array reported by Jiang *et al.*, which has a 67% average bandwidth⁶⁰.

According to the simulated pulse echo and beam profile results, the phased array transducer shows a relatively high expected acoustic performance which is matching to the evaluated pulse echo result of the transducer. However, according to the transducer imaging characterization results shown in Figure 5.24(b) and (d), the experimentally determined lateral resolutions is relatively lower than the simulated results, 121.5 μm against 68 μm . One of the reasons is that the simulated result presents an ideal case, while in reality, the non-100% yield rate of functional elements may alter the beam forming and result in poorer lateral resolution. The axial resolution which is mainly determined by bandwidth matches better to the modeling result (40.5 μm against 45.3 μm). By considering the geometry imperfection induced in the fabrication process and nonuniformity of the PMN-PT single crystal, such deviation is reasonable. In fact, PMN-PT relaxor single crystals with high piezoelectric properties are produced by using Bridgman melt growth method which is hard to maintain structure and composition homogeneity in a large volume compared to polycrystalline PZT. Thus, the piezoelectric properties of the buck PMN-PT are varied due to the properties are highly crystallinity dependence. Summing up with the geometrical difference created by dicing process and lapping process, the individual geometry imperfection of each element resulting in an arbitrary signal variation. Therefore, the algorithm may miscalculate the time delay between each individual element resulting in enlarged focal point during the beamforming process.

In addition, the crosstalk further reduces the signal-to-noise ratio and the dynamic range of the transducer, leading to lower resolution of the imaging, especially the lateral resolution. Those miscalculation of the transducer can be corrected by using the uniformity correction that adjusts the signal amplitude and time delay individually.

However, the correction algorithm has not been drifted and programmed in the beamforming actuating command. Therefore, the output image is a raw image which should have a lower performance than the ideal simulated result.

The crosstalks of element next to the adjacent elements illustrates a similar trend as the crosstalks of adjacent elements but with a lower average value. The maximum value is same as the adjacent elements' value. Normally, adjacent elements should have higher crosstalk than the one next to the adjacent element. This phenomenon has been seen in the investigation of Guess *et al.* who reported the crosstalk feature of a 3-MHz array transducer in which the crosstalk of the next to the adjacent element had a -45 dB amplitude which was 24 dB lower than that of the adjacent elements¹²¹. The measured crosstalk trend in this study is opposite to the result reported by Guess *et al.*, which is possibly due to the different electrical connection approach of elements. In this work, the even number of elements were connected to the same flexible circuit such that higher crosstalk would be generated through the electrodes of the flexible circuit. This phenomenon has also been observed from the 35-MHz PZT linear array developed by Cannata *et al.*⁷¹ at 2006. The crosstalk was stable and kept below -33 dB in the frequency range from 10 to 37 MHz that included the full operation frequency range used for the aforementioned calculations. According to the flexible connection design, odd or even number elements are located on the same flexible circuit. Thus, the electrical signal interference can only happen between #100, #98 and #102.

There are some suggestions to further improve the high-frequency phase array transducer's resolution. First, a separation of elements in a phased array should be designed to achieve 0.5λ to eliminate the grating lobe effect. The small size of element reduces the dimension of phased array, which is one of the merits allowing cardiac

imaging through the narrow gaps of small animal's ribs. However, beyond 20 MHz center frequency, the 0.5λ pitch should be smaller than $35 \mu\text{m}$ which is almost impossible to fabricate by a mechanical approach. Alternatively, as reported by Piredda *et al.*, laser cutting was used to construct PMN-PT phased array where a $15 \mu\text{m}$ cutting kerf width has been obtained using a 380 fs pulse laser¹⁰⁹. Foster *et al.* has also developed a PZT-based linear array using laser cutting to reach $8 \mu\text{m}$ kerfs⁷². Nevertheless, even using laser cutting, the cutting aspect ratio may still not appropriate for producing a 0.5λ pitch for transducers beyond 20 MHz. Meanwhile, the above reports also illustrated that the kerf produced by laser cutting shows a "V" shape and the cutting depth is hard to be accurately controlled. Our previous investigation also revealed that the macro-domain near the laser cutting kerf was distorted causing an absence of piezoresponse⁸⁷. By using the 0.8λ pitch dimension, the grating lobe is calculated locating outside the scanning field within $\pm 45^\circ$ angle of view. However, the advantage of the grating lobe elimination cannot be illustrated due to the small target size of this demonstration.

The maximum possible power is delivered to the transducer when the electrical impedance of the transducer equal to the complex conjugate of the impedance of the input source. Most of the power source and signal obtain device has a 50Ω electrical impedance¹²². The electrical impedance mismatch in our case causes an $\sim 40\%$ power loss for a complete pulse echo transmission line. The power loss may cause a reduction of sensitivity lower the SNR and the axial depth of view of the image. Besides, it also lower than the frequency bandwidth of the transducer due to the electrical impedance of the load (transducer) is frequency dependence. For achieving the ideal impedance value of 50Ω , the elevation direction is the only dimension that can be enlarged for increasing the surface area. By setting the elevation length to 5 mm in our transducer, the electrical

impedance is around 400Ω which is already the lowest in this circumstance. Practically, it is very hard to achieve 50Ω electrical impedance for phased array transducers. Alternatively, the electrical impedance can be compensated by the electrical impedance matching (EIM) network. The network can be designed depends on the KLM model, Butterworth-Van Dyke model and network model. In the EIM network, the admittance of the transducer is evaluated at the beginning. The component in values of the equivalent circuit for the EI unmatched transducer is determined afterward. Using the smith chart, multiple chooses of EIM network are designed based on the two-port complex electrical impedance matching method. The concept of Smith chart is to move the impedance value point of the unmatched transducer in the Smith chart to the center 50Ω value by adding capacitors or/and inductors in series or in parallel. In result, the complex impedance of the designed EIM network with the unmatched transducer at the load should be complex conjugated to the source impedance.

5.5 SUMMARY

An 85% wide bandwidth 20MHz PMN-0.28PT base phased-array ultrasound transducer has achieved in this investigation. Moreover, the phased array transducer illustrated a high uniformity that was suitable for medical imaging. The phased array transducer further showed a $40.5 \mu\text{m}$ and $121.5 \mu\text{m}$ axial and lateral resolution, respectively, in the wire phantom measurement. Although the lateral resolution was unexpectedly lower than the calculation value, the *in-situ* images of the fisheye and *in-vivo* image of rat heart have been collected respectively. The image of fisheye shows that the component's outline that can be distinguishable, but the detail of the component is missing due to the low signal to noise ratio arrowed by lack of electrical coupling between the phased array transducer

and operation system and side beam effect. Future improvement, such as narrowing the array pitch and designing an electrical impedance coupling, will be approached in attempting to increase the image resolution by increasing the signal to noise ratio. Correction of distance accuracy, linearity and uniformity for transducer are required to further improve the image quality. Imaging processing algorithm is required to reduce the image artifact, such as grating lobe artifact, in the future.

CHAPTER 6

DESIGN AND DEVELOPING AN ULTRASOUND TRANSDUCER FOR TRANSCRANIAL DIAGNOSIS AND THERAPY

6.1 BACKGROUND

Human's brain is the most complex organ controlling all physical and mental response of human's body, and its mechanism is still an unknown biological mystery. This complexity and uncertainty cause the difficulty and importance of human brain's diagnosis that attracts massive physician and researchers, such as physiologist and pathologist to improve the diagnostic technique of brain. Nowadays, the usual brain diagnostic tools are computed tomography (CT) and magnetic resonance imaging (MRI) due to their high penetration ability, for example, the brain image taken by MRI is shown in Figure 6.1(a). However, the harmfulness of the radiation of CT and MRI to brain is the biggest concern of patient which is still under investigation. Besides, ultrasound imaging is the best alternative which can be used on examining infants brain due to its harmlessness¹²³. Figure 6.2 shows the operation process of infant and adult cranial ultrasound imaging^{124,125}. Traditional cranial ultrasound is limited at infant brain imaging because the fontanelle allows high frequency ultrasound pulse penetration. By contrast, the adult cranial is too thick and its acoustic impedance causes a massive reflection of high frequency ultrasound pulse, so it has been replaced by intra-operative ultrasound imaging in adults.

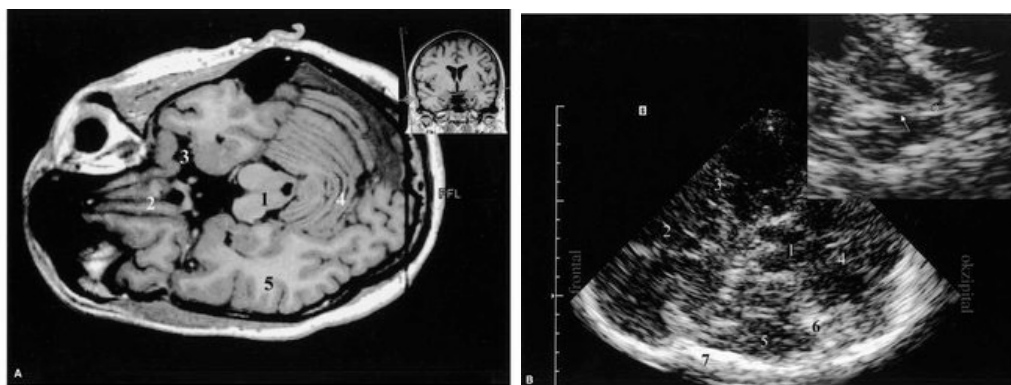


Figure 6.1 (a) Axial MRI at the level of the mesencephalon equivalent to the TCS image of the mesencephalon. (b) TCS image of the mesencephalic brainstem. 1: hypoechogenic mesencephalic brainstem surrounded by the hyperechogenic basal cisterns; 2: frontoorbital cortex and falx; 3: sulcus lateralis with the middle cerebral artery; 4: cerebellum; 5: temporal lobe; 6: tentorium; 7: contralateral skull¹²⁵.



Figure 6.2 Infant and adult cranial ultrasound imaging^{124,125}.

In human skull, temple is a juncture located at the side of the head behind the eye between the forehead and the ear. This area only has a 3 mm thickness and covered by temporal muscle that functions on mastication. This allows ultrasound pulse propagation with a high transmission ratio because, according to equation (18), its thin thickness causes a relatively lower attenuation for high-frequency ultrasound pulse when compared to other skull bones. Unfortunately, clinical transcranial imaging normally uses the linear array probe designed for cardiac imaging. The manufactured linear array typically has a large

surface area so the formed beam cannot fully pass through the thin temple, and as such most of the acoustic pulses emitted at the border elements which pass through the thick skull bones caused a blurry image in transcranial imaging. A less element number linear array transducer plus a mechanical scan could be a solution for temple imaging, however, movement of the transducer is limited due to the shape of the temple. There are also products in the market using Doppler ultrasound to brain blood flow evaluation and also ultrasound therapy using thermal effect of ultrasound for stroke patients.

Three-dimensional (3D) imaging is desired to obtain a larger spatial image. However, most of the regular 3D imaging transducers use a large aperture size to increase the spatial size of the image. Concurrently, the complexity of development of 2-D array transducer limited the size of the elements also increase the transducer's aperture. Thus, a lot of the elements of 2-D array is out of the temple region without any contribution during the image acquisition process.

According to this, a research gap for investigating a spectacular transducer for transcranial imaging is illustrated. Therefore, in this chapter, a 2D annular array for through-temple brain imaging consisted of therapeutic ultrasound function is designed and developed. By using the Fresnel lens pattern, the transducer has a natural focus point while excites all the elements simultaneously for producing a significantly high-pressure focusing ultrasound pulse aiming on transcranial therapy. Besides, a new assumption of controlling the excitation sequence to manipulate the steering and focal length of the ultrasound beam of this design for transcranial imaging is suggested. The schematic design of this transducer is elaborated as follows.

The convectional annular array contents multiple piezoelectric rings with vary ring widths along the radius direction following the Fresnel half-wave-band sources pattern. The

Fresnel pattern causes the emitted acoustic wave focusing at a point by constructive interference. The focused acoustic wave has a high energy strength and small aperture size that has been employed as a fluid ejector, a tumor terminator and importantly biomedical imaging, respectively^{81,126-128}. As reported by Kowk *et al.*, an annular array constructed by a piezoelectric material with a piezoelectric constant $d_{33}=230\text{pC/N}$ and electromechanical coupling coefficient $k_t=0.56$ was developed in 2011¹²⁷. The developed annular array has an extraordinary strength at 4.2-MHz center frequency that excited a 2.5 mm droplet of glycerin which has a high viscosity (1400 mPa s). This is evidence to show that the annular array transducer using Fresnel pattern can produce a tremendous pressure. This mode can also be employed to provide Doppler blood flow evaluation as a single element transducer. Another great advantage is that, this transducer may be used for image guided ultrasound therapy by providing mechanical energy instead of heat energy to reduce stroke or tumor burning etc. with a changeable focusing length.

Besides, with this convectional structure, a B-mode image can only be obtained through two-dimensional mechanical scanning. Similar to the previous motioned problem, according to the temple size which is the entrance of the high frequency acoustic pulse, movement is not allowed during the image acquisition. Thus, a phase array beam forming method controlled by electrical scanning is the only way to implement a large angle of view 2D ultrasound image without the mechanical movement. Combining these two ideas, a double sector shaped linear array is suggested to produce a phase array mechanism. To further elaborate this idea, the double sector design is repeated in the rotational direction which can combine multiple 2D image along the radial direction into a 3D spatial image in a conical shape. The schematic profile of the designed 2-D annular array structure is shown in Figure 6.3.

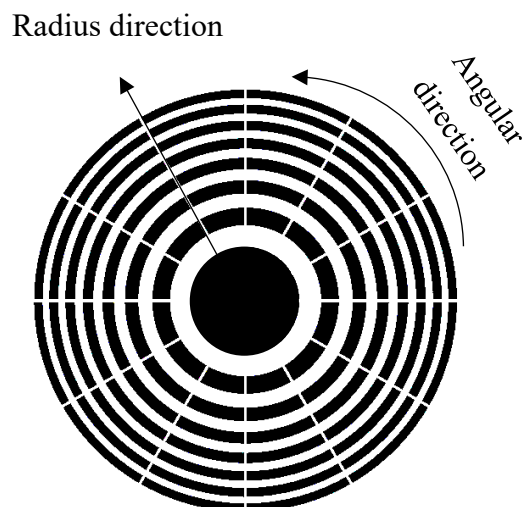


Figure 6.3 The schematic structure of the 2D annular array transducer.

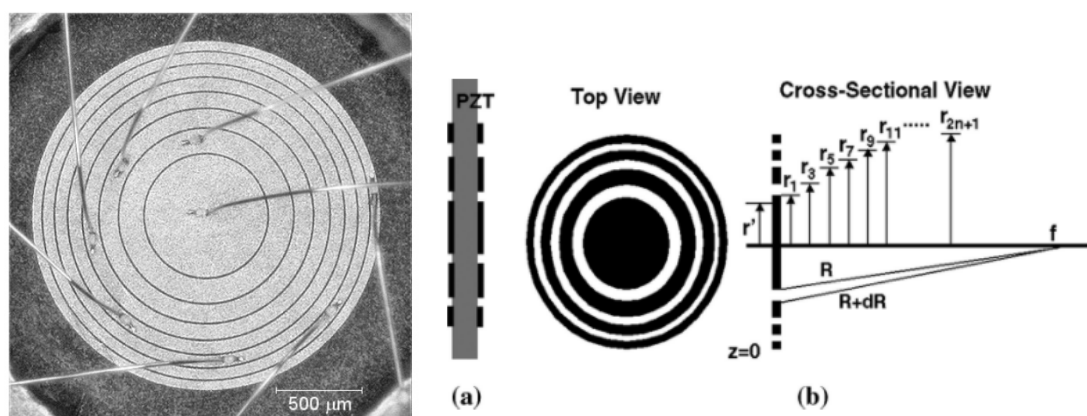


Figure 6.4 Traditional annular array with Fresnel structure⁸¹.

Comparing Figure 6.3 and the Fresnel annular array shown in Figure 6.4⁸¹, the main difference between the two arrays is that the ring shape elements in annular array have been separated along the radius angle direction. By electrical connecting the elements individually, steering freedom along both the radius and angular directions (the direction is shown in Figure 6.3) can be achieved in this new design. Therefore, a real-time 3D image of brain can be obtained by this 2D annular array through a limited entrance. In this imaging mode, the electrical controlled steering angle compensate the movement limitation of the brain imaging through temple.

In this chapter, the new structure of the 2D annular array is developed. As mentioned before, this new designed annular 2D array transducer can be excited in multiple mode for different purpose. A simultaneous excitation mode can produce an extraordinarily high acoustic pressure performing a transcranial therapy. A phase delay excitation mode can perform a beam steering for obtaining a transcranial image. Enterally, an image guided ultrasound transcranial therapy should be accomplished by combining both modes. In the first prototype, the imaging ability is focused and investigated to verify the feasibility of this idea. For obtaining a usable image, the resolution and sensitivity will be maximized by using PZT material which has a high piezoelectric property. The center frequency is set as 20-MHz and the element number is 48. Due to the structure difference between the 2D annular array and normal 2D phased array, a new beam forming phase delay and data collecting method will be investigated for achieving an acoustic beam steering and image processing.

6.2 EXPERIMENTAL DETAILS

6.2.1 Design of the 2D annular array transducer

Laser cutting is a more suitable way to patterning this new designed 2D annular array transducer. According to the previous investigation in chapter 4.1.1, the piezoelectricity of PMN-0.28PT may be affected by the laser cutting, therefore, a higher Curie temperature PZT is chosen to suppress the properties reduction. The kerf shape problem of the laser cutting is negligible due to the kerf and elements' width in this design are significantly larger than the phased array requirement. The influence of the laser cutting is minimized. The piezoelectric properties of a bulk PZT ceramic based ferroelectric plate (PIC151, PI Ceramic, Germany) will be employed as the active layer. By following the

similar method of Chapter 5, the properties of the PZT are first characterized and the performance of transducer is simulated by the PZFlex. Section 3.2.2 and section 5.2.1 have stated the detail of the piezoelectric layer characterization. For obtaining a higher resolution brain image, the center frequency of the transducer has been set as 20 MHz and the normal focal length has been set as 50 mm depending of the human head diameter. By determining these factor, the Fresnel pattern of the annular array can be further calculated by using the following equation (26) and Figure 6.5¹²⁹.

$$r_n = \sqrt{n\lambda f_0 + \left(\frac{n\lambda}{2}\right)^2} \quad (26)$$

Where n is an integer of the radius number, f_0 is the normal focusing length without the electrical steering and λ is the acoustic wavelength. According to the fabrication limitation and the bulk PZT size, the prototype has 12 sectors and 4 rings. Therefore, the prototype totally has 49 elements.

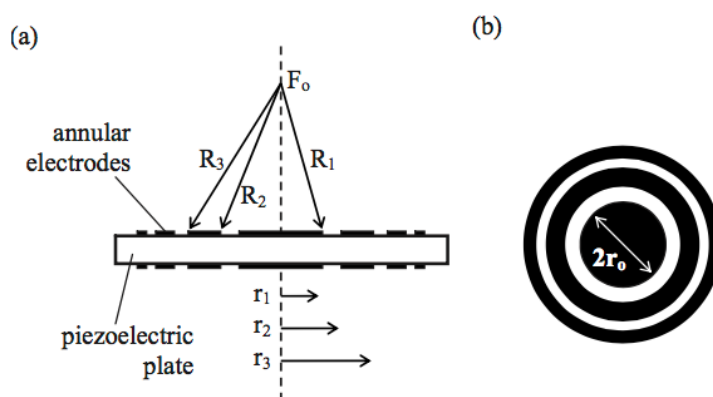


Figure 6.5 Schematics of (a)cross-section view and (b) top view of a piezoelectric layer of Fresnel annular array transducer¹²⁹.

For transducer targeting at medical imaging, matching layer is a required component. According to section 3.2.2, the acoustic impedance can be calculated. The investigated alumina epoxy composite will be employed as the first matching layer due to its tunable acoustic impedance property. The second matching layer use a pure epoxy EPO-TEK 301

which has an acoustic impedance around 3 MRayl. A tungsten, alumina and epoxy composited non-conductive backing layer with high acoustic impedance is used to produce a better acoustic impedance coupling between the backing and piezoelectric material. The data of the backing is shown in Table 6.3.

6.2.2 Modelling of 2D annular array

According to the irregular shape of the elements, the vibration mode of the piezoelectric is unknown. This irregular shape is not supported in the PizeoCAD thus a precise simulation result cannot be estimated by this software. Therefore, the thickness of the matching layers was set as the theoretical quarter wavelength value. A 3D model depending on those characterized and calculated value were created in the PZFlex. Then the steered beam profile controlled by an electrical system was simulated in the PZFlex to testify the assumption of beam forming method.

6.2.3 Fabrication of the 2D annular array transducer.

In this section, the procedure is listed by point form for more convenient reading. The procedure is shown as following:

1. The bulk material plane with a thickness of 0.5 mm was waxed on a glass and the front side was polished to remove the silver electrode. The silver electrode may reflect the laser pulse, thus reduces the cutting efficiency.
2. A ring-shaped cutting pattern was input into the laser cutting system allowing the laser cutting proceed automatically. The cutting depth is 0.5 mm and the diameter of laser was set as narrowest to produce a vertical wall at the edge of each ring. The patterned sample is shown in Figure 6.6.

3. An ultrasound cleaning was applied on the sample to remove the recrystallization of PZT at the edge of the elements.
4. Epoxy (EPO-TEK 301-1) was filled in the kerf of the sample, and degassing process was done to prevent any air bubble trapped inside the kerf.

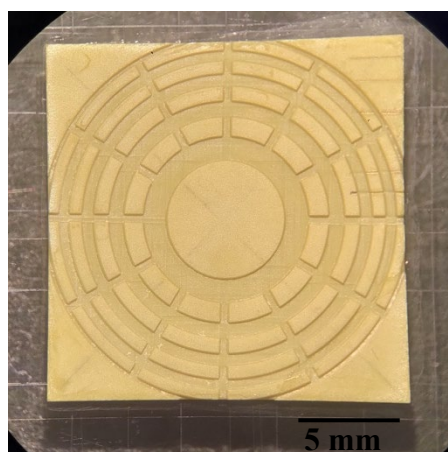


Figure 6.6 The profile of the patterned PZT.

5. A Cr/Cu/Au tri-layer electrode was deposited on the surface by using a magnetron sputtering method. The thicknesses of each layer are 24, 250 and 70 nm, respectively.
6. A photolithography was used to pattern the electrode on the surface into 48 elements. The photolithography mask is shown in Figure 6.7.

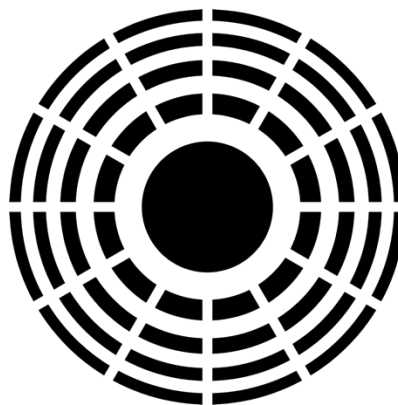


Figure 6.7 The photo mask used in photolithography.

7. The sample was then lapped to the designed 0.1 mm thickness.
8. A customized PCB board was placed at the outside of the annular array. All 48 elements were connected to the bonding pad using copper wire adhered with conductive epoxy E-Solder 3022. The connection diagram is showing in Figure 6.8.

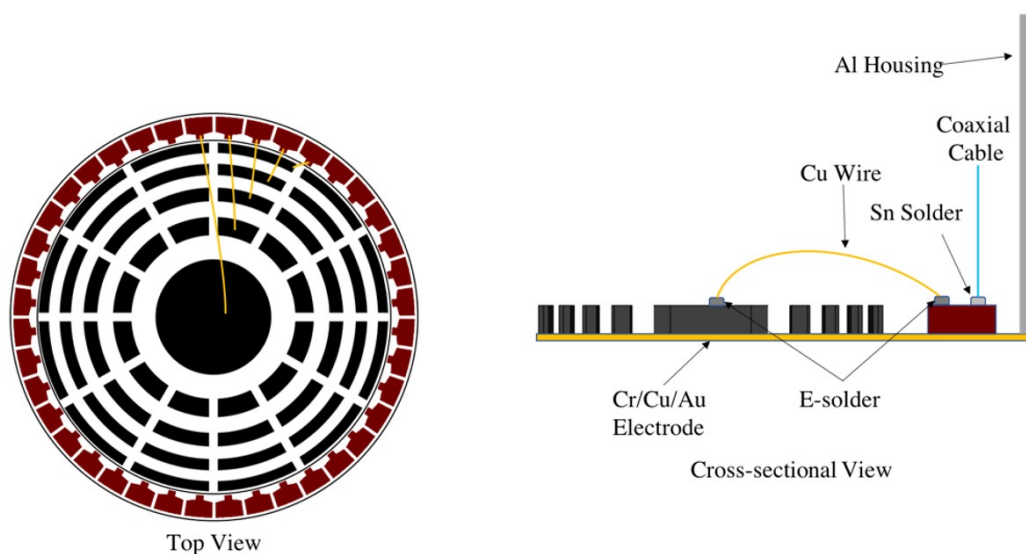


Figure 6.8 Top view and cross-sectional view of the schematic electrical connection diagram in annular 2D array transducer.

9. 48 coaxial cables were soldered on the PCB board (shown in Figure 6.8) and assembled into an aluminum housing.
10. Tungsten powder mixed with EPO-TEK 301 was filled in the aluminum housing to mount the array and represent the backing layer of the transducer. The ground of all 48 coaxial cables were connected to the housing for suppressing the E-M noise.
11. The tri-layer electrode same as step 6 was deposited on the front surface of the annular array for connecting the common ground to the housing.
12. The double matching layer was prepared individually. The double matching is cut into a circular shape by using the laser cutting. Then the matching was attached

on the surface of the annular array by using M-Bond 601. A slight press was applied on the matching during the curing for reducing the adhesive layer's thickness. All the acoustic parameters of the annular array are listed in section 6.3.1. The picture of the developed transducer is shown in Figure 6.9

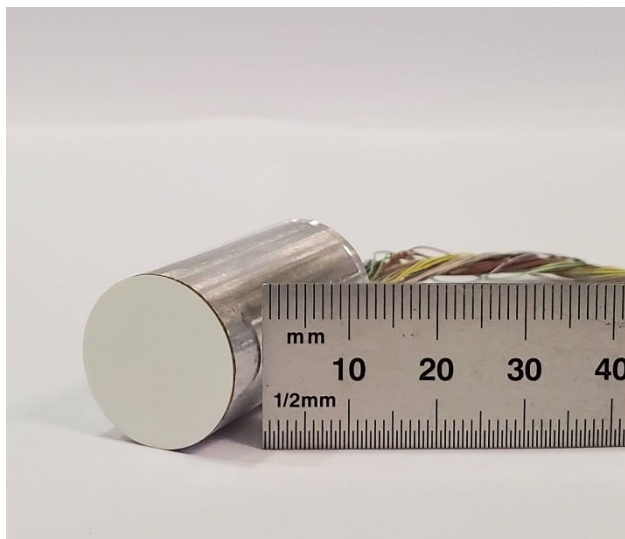


Figure 6.9 The prototype of the 2D annular array ultrasound transducer.

6.3 RESULTS AND DISCUSSION

6.3.1 *PZFlex simulation result*

To collaborate with Shanghai Institute of Ceramics, modelling the designed specification and beam formation of the annular array transducer was carried out by PZFlex simulation software. According to the transducer's structure, the 2D annular array is constructed by repeating one sector along the angular direction. Due to the computing power limitation, only one pair of the sectors have been selected to modelling the pressure field and beam forming structure in a two-dimensional space. The input PZT PIC151 piezoelectric properties and its dimension are listed in Table 6.1 and Table 6.2, respectively. The parameters of all the components are listed in Table 6.3. The 2D spatial structure and the

3D model are shown in Figure 6.10. The front medium is water with a 60 mm length along the axial direction and 18 mm width along the lateral direction. Backing layer thickness is 2 mm thick. The simulated pressure field result of one pair of sectors is shown in Figure 6.11.

TABLE 6.1 MEASURED PIEZOELECTRIC PROPERTIES OF PZT BULK MATERIAL.

Material	PZT PIC151
Longitudinal velocity v_z (ms^{-1})	4967
Density ρ (kgm^{-3})	7816
Clamped dielectric constant ϵ_{33}^s	2153
Piezoelectric constant d_{33} (pC/N)	526
Electromechanical coupling coefficient k_t	0.57
Acoustic impedance Z (MRayl)	38.82
Thickness (μm)	500

TABLE 6.2 THE DIMENSION OF EACH RING IN THE 2D ANNULAR ARRAY ULTRASOUND TRANSDUCER.

Ring Number	Ring Radius (mm)	Ring diameter (mm)
1	2.653	5.307
2	3.755	7.509
3	4.601	9.203
4	5.317	10.633
5	5.948	11.896
6	6.520	13.039
7	7.046	14.092
8	7.537	15.075
9	8.000	15.999

This simulation was performed in a focusing mode with no steering control. The simulation water tank has a dimension of 36 mm \times 48 mm. All the elements in these two sectors were excited simultaneously. The simulated result shows a strong focus at the

TABLE 6.3 PROPERTIES OF DIFFERENT ACOUSTIC LAYERS.

Matching layer number	Piezoelectric Layer	1	2	Backing layer
Material	PZT	2 – 3 μm Al ₂ O ₃ powder + Epoxy 502	EPO-TEK 301	Al ₂ O ₃ (200~300 mesh) + Epo-Tek301 +W(25 μm) powder
Weight ratio	N/A	2:1	N/A	1:1:4
Acoustic impedance (MRayl)	38.82	8.54	3.0	9.10
Velocity (ms ⁻¹)	4967	3654	2650	1900
Density (kgm ⁻³)	7816	2337	1132	4790
Thickness (mm)	0.125	0.046	0.033	2

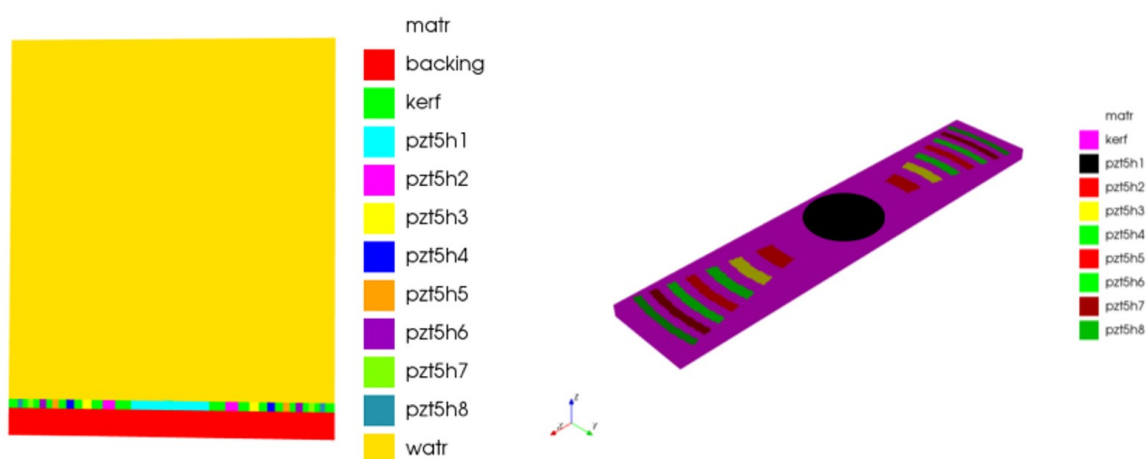


Figure 6.10 The 2D spatial structure of the simulation (Left) and the inputted 3D model (Right).

center of the lateral direction and around 34 mm away from the transducer's surface. The maximum pressure at the focal point is 20 kPa and the focal depth is around 12 mm. The realistic maximum pressure at this focal point should be higher than this simulated result, because the model only contains one pair of the sectors. The estimated focal point from the pressure field result is around 15 mm closer than the designed result. The missing sectors of the transducer in the simulation may cause an incomplete interference that not only reduces the maximum pressure output but also the focal point location. Besides, the

small element number along the angular direction may also affect the accuracy of focal length. The remarkably long focal depth along the axial direction in the pressure field simulation may be evidence proofing this assumption.

According to the circumference of the outer ring, the solder pad on a PCB board around the annular array transducer only has 50 mm length. Each solder pad only has around 1 mm length size for soldering one coaxial cable and one copper wire connecting

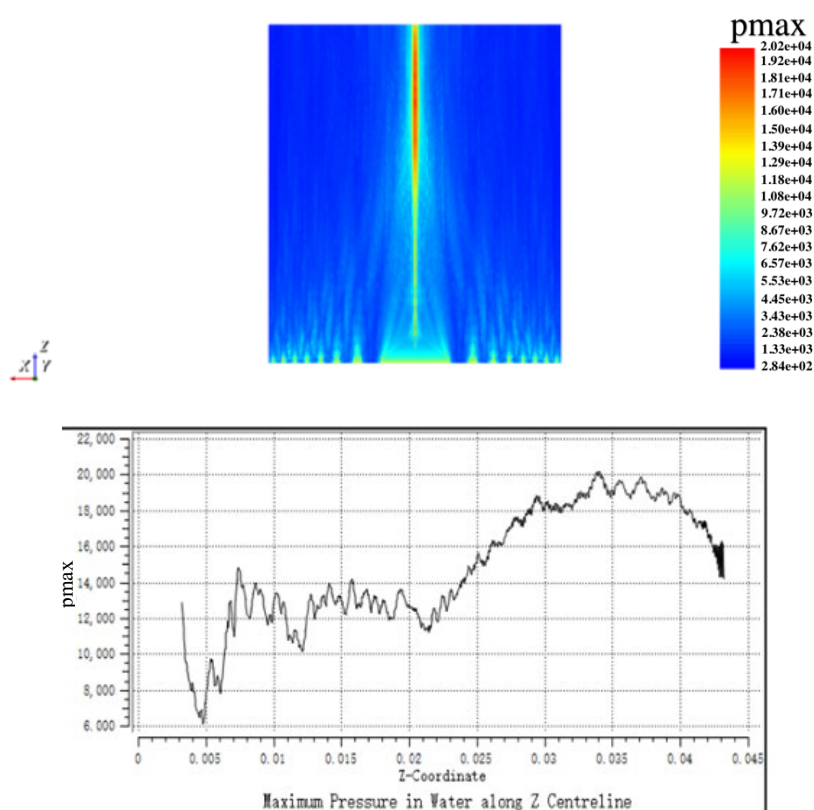


Figure 6.11 Simulated pressure field of one pair of sectors of the 2D annular array(top) and the pressure change along the axial direction at $x=0$.

the element. Adding one ring number increases 12 elements number in total. Referring to equation (26), the circumference enlargement doesn't supply enough space for the growth of solder pad, therefore, the soldering difficulty will be dramatically increased if the ring number increase. The connection technique requires an improvement to reduce the

connection difficult, therefore, allows the transducer comprising more ring elements.

6.3.2 Acoustic response of the 2D annular array ultrasound transducer

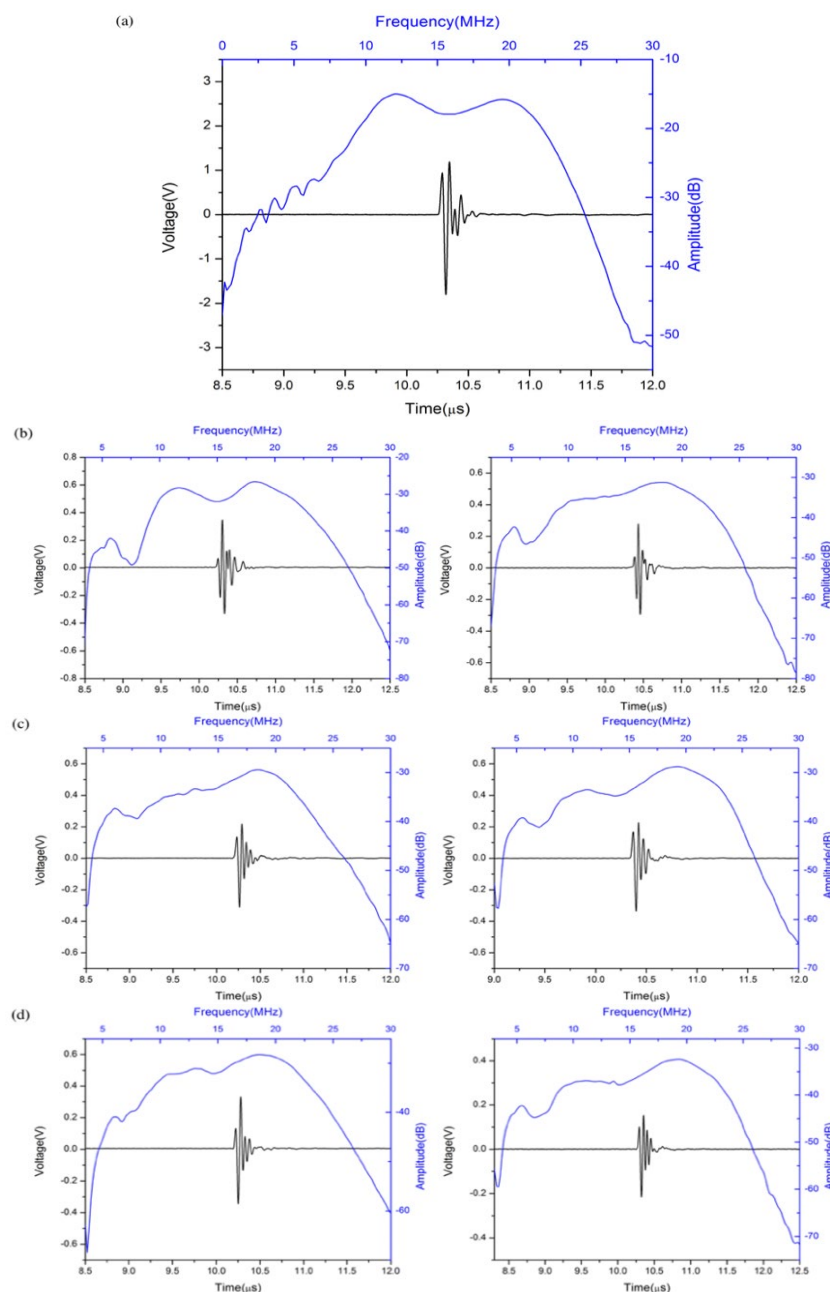


Figure 6.12 The two-way impulse response of (a) center element, (b) first ring, (c) second ring and (d) third ring, along time domain (Black) and frequency domain (Blue).

Due to the shape difference of each ring, the acoustic performance should vary depending on the ring's shape. The elements in a pair of sectors are tested individually. The two-way

impulse response of center element, two first ring elements, two second ring elements and two third ring elements are shown in Figure 6.12 (a), (b), (c) and (d) respectively. Those measured values are summarized in Table 6.4. The distance between the thick stainless steel reflector block and the transducer is 34 mm distance which is the same as the simulated focal point. The excitation frequency boundary is from 1 kHz to 50 MHz. According to the result, the center element illustrates a highest 2.99 V peak-to-peak pulse echo amplitude. The rest of the rings have an average amplitude 0.60 V. Only one of the third ring's elements has a relatively lower amplitude 0.37 V which is incoherent to its paired ring element's performance. The area of the center element is around 22.11 mm² calculated by the radius supported in Table 6.2. On the other hand, the area of rings

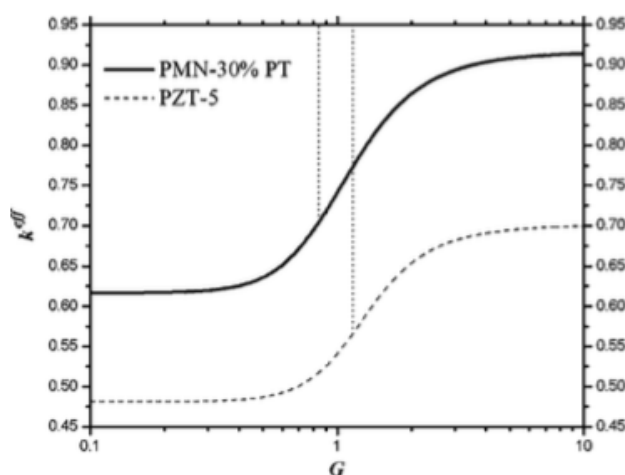


Figure 6.13 Effective electromechanical coupling coefficient of PMN0.3PT and PZT-5 as a function of element's thickness to width ratio¹³⁰.

located at different radius are 2.61 mm², 2.67 mm² and 2.70 mm², respectively. In contrast, the area of the center element is tremendously larger than the ring elements. The calculated electrical impedance at 16 MHz center frequency depending on the area of center and the area of rings are around 3 to 24 Ω, respectively. According to this, the

electrical loss of the center element due to the electrical impedance mismatch should be higher than those ring elements which is contrary to the evaluated results. On the other hand, the elements' dimension controls the vibration mode and the value of electromechanical coupling coefficient. Figure 6.13 shows the effective electromechanical coupling coefficient along the thickness direction of PMN-0.3PT varying with the element's thickness to width ratio. As shown in the figure, the effective electromechanical coupling coefficient changes from 0.62 to 0.9, which are respectively same as the k_{31} and k_{33} , while the thickness to width ratio (G) change from 0.1 to 10.

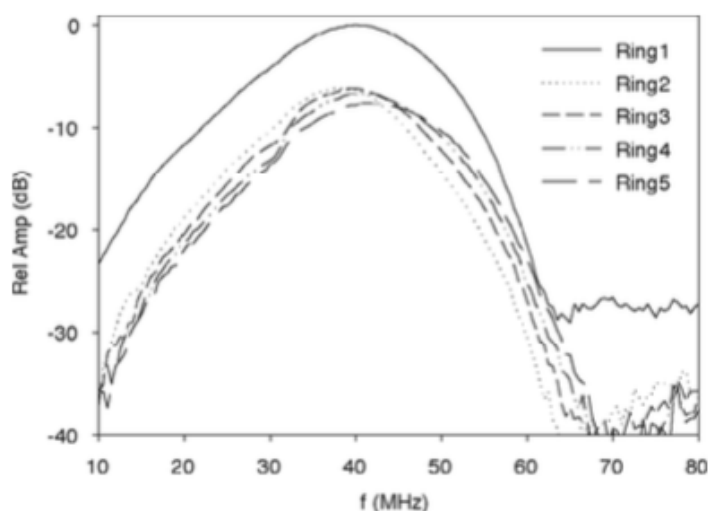


Figure 6.14 Pulse echo frequency spectrum for all five rings of the 40 Hz annular array¹³¹.

This phenomenon proves that thickness extension mode effectiveness contributing along thickness direction increases comparing with other vibration mode, for example transverse length mode (radial mode for circular shape), while G increases. In regarding to the dimension of the center element and ring elements, the center element vibrates at radial mode which has a significantly lower effective electromechanical coupling

coefficient value than the ring elements vibrated at thickness extension mode. Hypothetically, higher electromechanical coupling coefficient resulting in lower electrical to mechanical transfer loss, therefore, higher signal should be obtained with ring elements. This sensitivity variant between center ring and outer ring behavior has also been reported by Jeffrey *et al.* in 2005. The developed 40 MHz PVDF annular array transducer shows a -6 dB (50%) sensitivity reduction comparing to the center ring at 40 MHz although the elements of the transducer was designed to have the same area. The measured signal of all the rings according to the article is shown in Figure 6.14. However, the signal reduction ratio of the developed 2D annular in this thesis is much larger than the one in Jeffrey *et al.*'s article. The reason of this difference is that the outer ring of the 2D annular array is a separated ring instead of a completed ring shape referring to Jeffrey's single element annular transducer. The area of the outer ring of 2D annular array transducer has only 1/8 of the center ring. Therefore, the amplitude ratio in our case is quantitatively different to Jeffrey *et al.*'s finding. According to Jeffrey *et al.*'s reported results, the amplitude different still remained while the slight electrical impedance mismatch of each element has been modified by adding an electrical impedance matching network (EIMN). Eventually, the explanation of this mystery is left behind to the reader. A dissatisfaction connect may appear causing the lowest amplitude illustrated in one of the third ring. The average center frequency is 16.10 MHz varying from 15.95 MHz to 16.56 MHz. A large bandwidth can be found in all the elements within a range from 77.5% to 87.6%. Therefore, the lowest and highest resolution estimated axial resolution are 60.7 μm to 54.7 μm , respectively. A slight difference is found from the symmetric elements of the prototype which may affect the beam forming performance. This problem needs to be further investigated.

TABLE 6.4 THE TWO-WAY ACOUSTIC RESPONSE OF THE INNER FIRST ELEMENTS ALONG TIME DOMAIN (BLACK) AND FREQUENCY DOMAIN (BLUE).

	Center	1 st Ring	2 nd Ring	3 rd Ring			
Center Frequency (MHz)	15.95	15.95	15.95	16.10	16.56	16.18	16.02
Bandwidth (%)	85.1	77.5	79.5	74.9	83.9	81.2	87.6
V _{p-p} (V)	2.99	0.68	0.57	0.53	0.56	0.68	0.37

6.4 SUMMARY

The idea of the 2D annular array has been proved by the simulation result and the transducer has been successfully fabricated. The simulated result shows an on-axis focal point at 34 mm with maximum 20 kPa pressure. The focal spot size is 12 mm length along axial direction and 0.045 mm width along lateral direction. The developed PZT 2D annular array transducer contains total 48 elements distributed in 8 sectors is also measured. The represented elements along the sector show a 16.10 MHz average center frequency and a -6 dB bandwidth around 80%, which can theoretically produce a 60 μ m axial resolution.

CHAPTER 7

CONCLUSION AND FUTURE WORK

In this thesis work, advanced acoustic material, advanced transducer fabrication process, and advanced high-frequency phased array transducers as well as new-structured transducer are investigated. Detailed achievements are summarized as follows:

1. A new matching layer material with much higher acoustic impedance and ultralow attenuation has been achieved by an innovative method, i.e. a method usually used for ceramic plate synthesis but also applied in alumina power/epoxy composite. The maximum longitudinal velocity and acoustic impedance can be achieved as high as 3961 ms^{-1} and 9.52 MRayl , respectively, with a 4:1 alumina power to epoxy ratio and prepared under 62.4 MPa pressure. This method created an alumina/epoxy composite matching layer which exhibited the highest impedance value when compared to previous reported results using the same material. The matching material also shows a great uniformity and homogeneity in macro and microscopic scale. A demonstration using this matching material has been shown in a 53 MHz PZT single element transducer to achieve 91% bandwidth at -6 dB .
2. Laser cutting technology has been studied for array transducer fabrication to compare with fine mechanical cutting. The correlation of laser power and cutting feature has been well documented. An ultrasound cleaning method is suggested and evaluated for removing the recrystallization and residues in the kerf while controlling the laser beam at its minimum power. A polish treatment before dicing a fragile single crystal piezoelectric material is suggested and the experimental result shows a 99% yield rate. These results are certainly encouraging and can be

a good reference for further development of more complicated ultrasound transducers.

3. A 20 MHz phased array transducer targeting at high-resolution biomedical imaging has been successfully developed relying on replacing the active layer with a single crystal ferroelectric material PMN-0.28PT exhibiting high piezoelectric properties. By adopting our developed matching material, the fabricated transducer has achieved 85% yield rate and presented an excellent acoustic performance such as 85% -6 dB bandwidth and -45 dB crosstalk. However, the sensitivity of the transducer has been a trade-off for maximizing the bandwidth, thus the sensitivity is -42 dB. This value is still comparable to linear array type transducer but not considered as significantly outstanding. The transducer shows 40.5 μm and 121.5 μm axial and lateral resolutions, respectively. The in-situ imaging of a fisheye and in-vivo rat cardiac imaging have been demonstrated in which the outline of organ structures can be distinguished. This study shows that the 20 MHz PMN-0.28PT single crystal phased-array ultrasound transducer could fulfil the requirements for small animal imaging, which can be further applied on high-resolution clinical imaging.
4. A new structure of transducer has been invented to target application in human brain's diagnosis through the temple of the fontanelle. In addition to its application of brain imaging, the transducer has a Fresnel structure that can be excited in a focusing mode generating a high pressure for therapy such and blood flow measurement and stimulation. The idea of the focusing mode of 2D annular array has been proved by the simulation result processed by the PZFlex. The simulated result shows an on-axis 12 mm x 0.045 mm (LxH) focal spot at 34 mm distance

with maximum 20 kPa pressure while all the elements in the transducer are excited simultaneously in focusing mode without any electrical steering. Meanwhile, the experimental results show a maximum 2.99 V_{p-p} amplitude and a wide 80% average bandwidth at around 16 MHz center frequency. A theoretical 60 μm axial resolution is predicted on this developed 2D annular array.

The relationship between powder size and acoustic properties of matching developed by compression method will be further analyzed in the near future. With the increase of surface area to volume ratio, the attenuation, as well as the velocity, may be possibly changed. The compression method can be applied on other materials or components to complete the database. Hopefully a more comprehensive knowledge of developing acoustic matching can be established. Besides, other techniques in development, such as DIRE, ICP and FIB, will be examined and improved for developing new ultrasound transducer that requires a higher aspect or special shape.

The phased array shows an impressive imaging ability but has rooms for improvement to perform a comparable result to the performance of commercial ultrasound imaging system. The grating lobe is illustrated in the measurements affecting the resolution of the image, which can be reduced by further narrowing down the element pitch of the phased array transducer. Techniques to produce a narrower pitch can be explored in the near future. Besides, electrical impedance of the element can be increased by reducing the transducer pitch. An electrical impedance coupling is an attractive method to maintain or increase the sensitivity, along with the signal to noise ratio, of the transducer to optimize the image quality. More importantly, other than structural improvement, the correction of distance accuracy, linearity and uniformity for transducer will be designed and performed to improve the uniformity of the transducer algorithmically. Imaging processing

algorithm will also be programmed in the future to reduce other image artifacts.

The design and fabrication technique of the 2D annular array transducer needs to be improved to include more elements to accomplish brain imaging through the temple of the fontanelle. As a new type of transducer, new imaging mechanism needs to be developed by programming to control the beam steering. A steering simulation is in progress to prove the hypothesis of the beam steering method, and the processing of imaging hereafter.

Moreover, the electrode connection strategy for high-frequency array transducers remains an issue to be addressed in order to achieve 100% yield rate. A flexible circuit can be designed for replacing soldering method. Concurrently, the elements number can be massively increased to around 256 which is a more suitable value to implement the brain imaging. Afterward, wire phantom imaging for resolution determination can be further explored.

REFERENCE

1. *Ultrasound Devices Market Estimates & Trend Analysis From 2014 to 2026*. 1–68 (2019).
2. *Magnetic Resonance Imaging Market Report, 2021-2028*. (2020).
3. Shung, K. K. *Diagnostic Ultrasound*. (CRC Press, 2015). doi:10.1201/b18323
4. Turnbull, D. H. In Utero Ultrasound Backscatter Microscopy of Early Stage Mouse Embryos. *Computerized Medical Imaging and Graphics* **23**, 25–31 (1999).
5. Lockwood, G. R., Turnbull, D. H., Christopher, D. A. & Foster, F. S. Beyond 30 MHz [Applications of High-Frequency Ultrasound Imaging]. *Engineering in Medicine and Biology Magazine, IEEE* **15**, 60–71 (1996).
6. Foster, F. S., Lockwood, G. R., Ryan, L. K., Harasiewicz, K. A. & Berube, L. Principles and Applications of Ultrasound Backscatter Microscopy. *IEEE Trans. Ultrason., Ferroelect., Freq. Contr.* **40**, 608–617 (1993).
7. Hoskins, P., Martin, K. & Thrush, A. *Diagnostic Ultrasound*. 1–276 (2010).
8. Passmann, C. & Ermert, H. A 100-MHz Ultrasound Imaging System for Dermatologic and Ophthalmologic Diagnostics. *IEEE Trans. Ultrason., Ferroelect., Freq. Contr.* **43**, 545–552 (1996).
9. Vscan Air Portable, Handheld Ultrasound. <https://vscan-air.gehealthcare.com/> (2021)
10. EPIQ 5 Ultrasound System for Radiology. <https://www.philips.co.uk/healthcare/product/HC795204R/epiq-5-ultrasound-system> (2021)
11. Sherar, M. D. & Foster, F. S. The Design and Fabrication of High Frequency Poly (Vinylidene Fluoride) Transducers. *Ultrasonic Imaging* **11**, 75–94 (1989).
12. Pavlin, C. J., Harasiewicz, K. & Foster, F. S. Ultrasound Biomicroscopy of Anterior Segment Structures in Normal and Glaucomatous Eyes. *Elsevier* doi:10.1016/S0002-9394(14)76159-8
13. Pavlin, C. J., McWhae, J. A., McGowan, H. D. & Foster, F. S. Ultrasound Biomicroscopy of Anterior Segment Tumors. *Ophthalmology* **99**, 1220–1228 (1992).
14. Advances in ultrasound biomicroscopy. *Ultrasound in Medicine & Biology* **26**, 1–27 (2000).
15. Turnbull, D. H., Ramsay, J. A. & Shivji, G. S. Ultrasound Backscatter Microscope Analysis of Mouse Melanoma Progression. *Elsevier* doi:10.1016/0301-5629(96)00107-X
16. Passmann, C., Ermert, H. & Auer, T. In Vivo Ultrasound Biomicroscopy. *ieeexplore.ieee.org*
17. Stiller, M. J. *et al.* Three-Dimensional Imaging for Diagnostic Ultrasound in Dermatology. *Journal of the American Academy of Dermatology* **29**, 171–175 (1993).
18. Rasmussen, M. F. 3D Ultrasound Imaging Performance of a Row-Column Addressed 2D Array Transducer: A Simulation Study. doi:10.1117/12.2007083

19. Diarra, B., Liebgott, H., Tortoli, P. Sparse Array Techniques for 2D Array Ultrasound Imaging. *The Acoustics 2012 Nantes Conference*
20. Diarra, B., Liebgott, H., Robini, M. C., Tortoli, P. & Cachard, C. Optimized 2D Array Design for Ultrasound Imaging. *EUSIPCO* (2012).
21. Bureau, J. M. & Steichen, W. A Two-Dimensional Transducer Array for Real-Time 3D Medical Ultrasound Imaging. *IEEE Ultrasound Symposium* (1998).
22. Zhang, L. *et al.* A High-Frequency, High Frame Rate Duplex Ultrasound Linear Array Imaging System for Small Animal Imaging. *IEEE Trans. Ultrason., Ferroelect., Freq. Contr.* **57**, 1548–1557 (2010).
23. Chen, R. *et al.* PMN-PT Single-Crystal High-Frequency Kerfless Phased Array. *IEEE Trans. Ultrason., Ferroelect., Freq. Contr.* **61**, 1033–1041 (2014).
24. Chen, Y. *et al.* High-Frequency PIN–PMN–PT Single Crystal Ultrasonic Transducer for Imaging Applications. *Appl. Phys. A* **108**, 987–991 (2012).
25. Li, H. Fabrication of Single Crystal Based Phased Array Medical Imaging Ultrasonic Transducers. (2008).
26. Li, H. *et al.* Application of PMNPT Single Crystal in a 3.2 MHz Phased-Array Ultrasonic Medical Imaging Transducer. *IEEE*, 572–574 (2007). doi:10.1109/isaf.2007.4393332
27. Lau, S. T. *et al.* Multiple Matching Scheme for Broadband 0.72Pb(Mg_{1/3}Nb_{2/3})O₃-0.28PbTiO₃ Single Crystal Phased-Array Transducer. *J. Appl. Phys.* **105**, 4908 (2009).
28. Chen, Y. *et al.* Endoscopic Ultrasound Radial Array Transducers Fabricated with PZT Tube by a Rotate-and-Dice Method. *Sensors & Actuators: A. Physical* **201**, 357–362 (2013).
29. Kim, D. W. *et al.* Magnetically Enhanced Inductively Coupled Plasma Etching of 6H-SiC. *IEEE Trans. Plasma Sci.* **32**, 1362–1366 (2004).
30. Wang, H., Ritter, T., Cao, W. & Shung, K. K. High Frequency Properties of Passive Materials for Ultrasonic Transducers. *IEEE Trans. Ultrason., Ferroelect., Freq. Contr.* **48**, 78–84 (2001).
31. Dawson, A., Gouws, G., Harris, P. & Young, R. Acoustic Impedance Matching with Porous Aluminium. *IEEE* 49–52 (2009). doi:10.1109/ICSENS.2009.5398122
32. Qifa Zhou *et al.* Alumina/Epoxy Nanocomposite Matching Layers for High-Frequency Ultrasound Transducer Application. *IEEE Trans. Ultrason., Ferroelect., Freq. Contr.* **56**, 213–219 (2008).
33. Fang, H. J. *et al.* Anodic Aluminum Oxide-Epoxy Composite Acoustic Matching Layers for Ultrasonic Transducer Application. *Ultrasonics* **70**, 29–33 (2016).
34. Manh, T., Jensen, G. U., Johansen, T. F. & Hoff, L. Modeling and Characterization of a Silicon-Epoxy 2-2 Composite Material. *IEEE*, 2234–2237 (2012). doi:10.1109/ULTSYM.2012.0558

35. Manh, T., Jensen, G. U., Johansen, T. F. & Hoff, L. Microfabricated 1–3 Composite Acoustic Matching Layers for 15MHz Transducers. *Ultrasonics* **53**, 1141–1149 (2013).
36. Rathod, V. T. A Review of Acoustic Impedance Matching Techniques for Piezoelectric Sensors and Transducers. *Sensors* **20**, 4051–64 (2020).
37. Clevert, D. A. White Paper: Lung Ultrasound in Patients with Coronavirus COVID-19 Disease. (2020).
38. Antúnez-Montes, O. Y., intensiva, D. B. M.2020. Routine Use of Point-of-Care Lung Ultrasound During the COVID-19 Pandemic. *ncbi.nlm.nih.gov*
39. Wong, C.-M. *et al.* Development of a 20-MHz Wide-Bandwidth PMN-PT Single Crystal Phased-Array Ultrasound Transducer. *Ultrasonics* **73**, 181–186 (2017).
40. Scampini, J. Overview of Ultrasound Imaging Systems and the Electrical Components Required for Main Subfunctions. *maximintegrated.com*. <https://www.maximintegrated.com/en/design/technical-documents/tutorials/4/4696.html> (2021)
41. Omer Oralkan, A. S. E. J. A. J. U. D. K. K. T. H. L. A. B. T. K.-Y. Capacitive Micromachined Ultrasonic Transducers: Next-Generation Arrays for Acoustic Imaging? 1–15 (2002).
42. Manbachi, A. & Cobbold, R. S. C. Development and Application of Piezoelectric Materials for Ultrasound Generation and Detection. *Ultrasound* **19**, 187–196 (2011).
43. Zab, D. Pyroelectric Structures and Devices for Thermal Energy Harvesting. (2016). doi:10.13140/RG.2.2.27890.56009
44. Skoog, D. A., Crouch, S. R. & Holler, F. J. *Principles of Instrumental Analysis*. (Cengage Learning Editores, 2008).
45. Gao, J., Xue, D., Liu, W., Zhou, C. & Ren, X. Recent Progress on BaTiO₃-Based Piezoelectric Ceramics for Actuator Applications. *Actuators* **6**, 24–20 (2017).
46. Damjanovic, D. Ferroelectric, Dielectric and Piezoelectric Properties of Ferroelectric Thin Films and Ceramics. *Reports on Progress in Physics* **61**, 1267–1324 (1998).
47. Sriratana, W., Murayama, R. & Tanachaikhan, L. Synthesis and Analysis of PZT Using Impedance Method of Reactance Estimation. *AMPC* **03**, 62–70 (2013).
48. Eddy, M. Resonators Fuel High- Performance RF Filters for 5G. 1–6 (2020). Available at: (Accessed: 6 January 2021)
49. Alvarez-Arenas, T. E. G. Acoustic Impedance Matching of Piezoelectric Transducers to the Air. *IEEE Trans. Ultrason., Ferroelect., Freq. Contr.* **51**, 624–633 (2004).
50. Desilets, C. S., Fraser, J. D. & Kino, G. S. The Design of Efficient Broad-Band Piezoelectric Transducers. *IEEE Trans. Son. Ultrason.* **25**, 115–125 (1978).
51. Krimholtz, R., Leedom, D. A. & Matthaei, G. L. New Equivalent Circuits for Elementary Piezoelectric Transducers. *Electron. Lett.* **6**, 398 (1970).

52. Sherrit, S., Leary, S. P., Dolgin, B. P. & Bar-Cohen, Y. Comparison of the Mason and KLM Equivalent Circuits for Piezoelectric Resonators in the Thickness Mode. *ULTSYM-99* **2**, 921–926 (1999).
53. PERSSON, H. W. & HERTZ, C. H. Acoustic-Impedance Matching of Medical Ultrasound Transducers. *Ultrasonics* **23**, 83–89 (1985).
54. Fazlyyyakhmatov, M. Sensitivity and Directivity Measurement of Ultrasonic Transducer with Polymer-Powder Matching Layer. *Journal of Physics: Conference Series* **1038**, 012109 (2018).
55. Catherine, O. & Otto, M. *Textbook of Clinical Echocardiography*. (2000).
56. Bezanson, A., Adamson, R. & Brown, J. A. Fabrication and Performance of a Miniaturized 64-Element High-Frequency Endoscopic Phased Array. *IEEE transactions on ...* **61**, 33–43 (2014).
57. Ma, J. *et al.* High Frequency Transducer for Vessel Imaging Based on Lead-Free Mn-Doped ($K_{0.44}Na_{0.56}$)NbO₃ single Crystal. *Appl. Phys. Lett.* **111**, 092903–6 (2017).
58. Cummins, T., Eliahoo, P. & Shung, K. High Frequency Ultrasound Array Designed for Ultrasound Guided Breast Biopsy. *IEEE Trans. Ultrason., Ferroelect., Freq. Contr.* **6**, 817–827 (2016).
59. Lam, K. H. *et al.* Development of Lead-Free Single-Element Ultrahigh Frequency (170–320 MHz) Ultrasonic Transducers. *Ultrasonics* **53**, 1033–1038 (2013).
60. Jiang, X., Snook, K., Liu, R., Geng, X. & Hackenberger, W. S. Fabrication and Characterization of High Frequency Phased Arrays for NDE Imaging. *Proceedings of the SPIE* **7649**, (2010).
61. Bantignies, C. *et al.* Lead-Free High-Frequency Linear-Array Transducer (30 MHz) for in Vivo Skin Imaging. *IEEE*, 785–788 (2013). doi:10.1109/ULTSYM.2013.0202
62. Liu, C. G., Djuth, F. T., Zhou, Q. F. & Shung, K. K. Micromachining Techniques in Developing High Frequency Piezoelectric Composite Ultrasound Array Transducers. *IEEE*, 1747–1750 (2011). doi:10.1109/ULTSYM.2011.0436
63. Changgeng Liu, Qifa Zhou, Djuth, F. T. & Shung, K. K. High-Frequency (>50 MHz) Medical Ultrasound Linear Arrays Fabricated From Micromachined Bulk PZT Materials. *IEEE Trans. Ultrason., Ferroelect., Freq. Contr.* **59**, 315–318 (2012).
64. Chen, Y. *et al.* High Frequency PMN-PT Single Crystal Focusing Transducer Fabricated by a Mechanical Dimpling Technique. *Ultrasonics* **53**, 345–349 (2013).
65. Feng, G.-H. & Liu, W.-F. A Spherically-Shaped PZT Thin Film Ultrasonic Transducer with an Acoustic Impedance Gradient Matching Layer Based on a Micromachined Periodically Structured Flexible Substrate. *Sensors* **13**, 13543–13559 (2013).

66. Ritter, T. A., Shrout, T. R., Tutwiler, R. & Shung, K. K. A 30-MHz Piezo-Composite Ultrasound Array for Medical Imaging Applications. *IEEE Trans. Ultrason., Ferroelect., Freq. Contr.* **49**, 217–230 (2002).
67. Wong, C.-M. *et al.* An Ultrawide Bandwidth High Frequency Phased-Array Ultrasound Transducer Fabricated Using the PMN-0.3PT Single Crystal. *IEEE* 1–4 (2016). doi:10.1109/ultsym.2016.7728580
68. Qiu, W. *et al.* A Novel Dual-Frequency Imaging Method for Intravascular Ultrasound Applications. *Ultrasonics* **57**, 31–35 (2015).
69. Zhang, J., Ren, W., Jing, X., Shi, P. & Wu, X. Deep Reactive Ion Etching of PZT Ceramics and PMN-PT Single Crystals for High Frequency Ultrasound Transducers. *Ceramics International* (2015). doi:10.1016/j.ceramint.2015.03.258
70. Jie Chen & Panda, R. Review: Commercialization of Piezoelectric Single Crystals for Medical Imaging Applications. *IEEE*, 235–240 (2005).
71. Cannata, J. M., Williams, J. A., Zhou, Q. F., Ritter, T. A. & Shung, K. K. Development of a 35-MHz Piezo-Composite Ultrasound Array for Medical Imaging. *IEEE Trans. Ultrason., Ferroelect., Freq. Contr.* **53**, 224–236 (2006).
72. Foster, F. S. *et al.* A New 15-50 MHz Array-Based Micro-Ultrasound Scanner for Preclinical Imaging. *Ultrasound in Medicine & Biology* **35**, 1700–1708 (2009).
73. Cannata, M., Zhou, Q. F. & Shung, K. K. Development of a High Frequency (35 MHz) Linear Ultrasonic Array Using 2-2 Composite Elements [Biomedical Applications]. *IEEE 1992 Ultrasonics Symposium Proceedings* **2**, 894–897 Vol.2 (2004).
74. Hayward, G., Bennett, J. & Hamilton, R. A Theoretical Study on the Influence of Some Constituent Material Properties on the Behavior of 1-3 Connectivity Composite Transducers. *The Journal of the Acoustical Society of America* **98**, 2187–2196 (1995).
75. Yuan, J., Sorah Rhee & Jiang, X. N. 60 MHz PMN-PT Based 1-3 Composite Transducer for IVUS Imaging. *IEEE*, 682–685 (2008). doi:10.1109/ULTSYM.2008.0164
76. Chiu, C. T. *et al.* Fabrication and Characterization of a 20 MHz Microlinear Phased Array Transducer for Intervention Guidance. *IEEE*, 2121–2124 (2014). doi:10.1109/ultsym.2014.0528
77. Cannata, J. M., Ritter, T. A. & Shung, K. K. A 35 MHz Linear Array for Medical Imaging. *IEEE*, 1157–1160 (2001).
78. Tsai, J. Z. *et al.* A new PZT piezoelectric sensor for gravimetric applications using the resonance-frequency detection. *Sensors and Actuators B: Chemical* **139**, 259–264 (2009).
79. Park, C. Y., Kwon, D. S., Sung, J. H. & Jeong, J. S. Dual-Frequency Ultrasound Transducer Using Inversion Layer Technique for Therapeutic Ultrasound Surgery. *IEEE Sensors J.* **17**, 6859–6866 (2017).

80. Wang, Z. *et al.* A Flexible Ultrasound Transducer Array with Micro-Machined Bulk PZT. *Sensors* **15**, 2538–2547 (2015).
81. Brown, J. A., Demore, C. & Lockwood, G. R. Design and Fabrication of Annular Arrays for High-Frequency Ultrasound. *IEEE Trans. Ultrason., Ferroelect., Freq. Contr.* **51**, 1010–1017 (2004).
82. Manh, T., Nguyen, A., Johansen, T. F. & Hoff, L. Microfabrication Of Stacks Of Acoustic Matching Layers For 15 MHz Ultrasonic Transducers. *Elsevier* (2014).
83. Qian, Y. & Harris, N. R. Modelling of a Novel High-Impedance Matching Layer for High Frequency (>30MHz) Ultrasonic Transducers. *Ultrasonics* **54**, 586–591 (2014).
84. Rhee, S., Ritter, T. A., Shung, K. K., Wang, H. & Cao, W. Materials For Acoustic Matching In Ultrasound Transducers. *2001 IEEE Ultrasonics Symposium. Proceedings. An International Symposium (Cat. No.01CH37263)* doi:10.1109/ultsym.2001.991900
85. Zhou, D. *et al.* Characterization of complete electromechanical constants of rhombohedral $0.72\text{Pb}(\text{Mg}_{1/3}\text{Nb}_{2/3})-0.28\text{PbTiO}_3$ single crystals. *J. Phys. D: Appl. Phys.* **41**, 185402 (2008).
86. Qifa Zhou *et al.* Alumina/Epoxy Nanocomposite Matching Layers for High-Frequency Ultrasound Transducer Application. *IEEE Trans. Ultrason., Ferroelect., Freq. Contr.* **56**, 213–219 (2008).
87. Lam, K. H. *et al.* Kerf Profile and Piezoresponse Study of the Laser Micro-Machined PMN-PT Single Crystal Using 355nm Nd:YAG. *Materials Research Bulletin* **48**, 3420–3423 (2013).
88. Kagadis, G. C., Loudos, G., Katsanos, K., Langer, S. G. & Nikiforidis, G. C. In Vivo Small Animal Imaging: Current Status and Future Prospects. *Medical Physics* **37**, 6421–6442 (2010).
89. Lewis, J. S., Achilefu, S., Garbow, J. R., of, R. L. E. J.2002. Small Animal Imaging: Current Technology and Perspectives for Oncological Imaging. *Elsevier* doi:10.1016/S0959-8049(02)00394-5
90. Jaiswal, R. S., Singh, J. & Adams, G. P. High-Resolution Ultrasound Biomicroscopy for Monitoring Ovarian Structures in Mice. *Reprod Biol Endocrinol* **7**, 1–7 (2009).
91. Dietz, D. R. *et al.* Laparoscopic Ultrasound for Minimally Invasive Surgery. *IEEE*, 1575–1583 (1995).
92. Pilecki, Z. *et al.* Podstawowe Techniki Preparacyjne W Sonochirurgii. *Journal of Ultrasonography* **14**, 171–178 (2014).
93. Minnard, E. A. *et al.* Laparoscopic Ultrasound Enhances Standard Laparoscopy in the Staging of Pancreatic Cancer. *Annals of Surgery* **228**, 182–187 (1998).
94. Relaxor Ferroelectrics. *Ferroelectrics* **76**, 241–267 (1987).
95. Bokov, A. A. & Ye, Z. G. Recent Progress in Relaxor Ferroelectrics with Perovskite Structure. *J Mater Sci* **41**, 31–52 (2006).

96. Kleemann, W. Relaxor Ferroelectrics: Cluster Glass Ground State via Random Fields and Random Bonds. *physica status solidi (b)* **251**, 1993–2002 (2014).
97. Li, F. *et al.* The Origin of Ultrahigh Piezoelectricity in Relaxor-Ferroelectric Solid Solution Crystals. *Nature Communications* **7**, 1–9 (2016).
98. Westphal, V., Kleemann, W. & Glinchuk, M. D. Diffuse Phase Transitions and Random-Field-Induced Domain States of the ‘Relaxor’ Ferroelectric $\text{PbMg}_{1/3}\text{Nb}_{2/3}\text{O}_3$. *Phys. Rev. Lett.* **68**, 847–850 (1992).
99. Park, S.-E. & Shrout, T. R. Ultrahigh Strain and Piezoelectric Behavior in Relaxor Based Ferroelectric Single Crystals. *J. Appl. Phys.* **82**, 1804–1811 (1997).
100. Oakley, C. G. & Zipparo, M. J. Single Crystal Piezoelectrics: a Revolutionary Development for Transducers. *IEEE*, 1157–1167 (2000).
101. Zhang, R., Jiang, B. & Cao, W. Elastic, Piezoelectric, and Dielectric Properties of Multidomain $0.67\text{Pb}(\text{Mg}_{1/3}\text{Nb}_{2/3})\text{O}_3$ - 0.33PbTiO_3 Single Crystals. *J. Appl. Phys.* **90**, 3471–3475 (2001).
102. Park, S.-E. & Shrout, T. R. Characteristics of Relaxor-Based Piezoelectric Single Crystals for Ultrasonic Transducers. *IEEE Trans. Ultrason., Ferroelect., Freq. Contr.* **44**, 1140–1147 (1997).
103. Su, Q. *et al.* Self-Separated PZT Thick Films with Bulk-Like Piezoelectric and Electromechanical Properties. *Journal of Materials Research* **26**, 1431–1435 (2011).
104. Jaffe, H. & Berlincourt, D. A. Piezoelectric Transducer Materials. *Proceedings of the IEEE* **53**, 1372–1386 (1965).
105. Saitoh, S., Takeuchi, T. & Kobayashi, T. A 3.7 MHz Phased Array Probe Using $0.91\text{Pb}(\text{Zn}_{1/3}\text{Nb}_{2/3})\text{O}_3$ - 0.09PbTiO_3 . *IEEE transactions on ...* **46**, 414–421 (1998).
106. Ming Lu, X. & Proulx, T. L. Single Crystals vs. PZT Ceramics for Medical Ultrasound Applications. *IEEE*, 227–230 (2005).
107. Zhang, S. & Li, F. High Performance Ferroelectric Relaxor- PbTiO_3 Single Crystals: Status and Perspective. *J. Appl. Phys.* **111**, 031301 (2012).
108. Ultrasound Therapy 2.0. <http://www.equultrasound.com/general-info-about-therapeutic-ultrasound/> (2016)
109. Piredda, G. Micro-machining of PMN-PT Crystals with Ultrashort Laser Pulses. *Appl. Phys. A* **125**, 1–11 (2019).
110. Desilets, C. S. Transducer Arrays Suitable for Acoustic Imaging. (Ph.D. Thesis Stanford Univ., 1978).
111. Lukacs, M. *et al.* Performance and Characterization of New Micromachined High-Frequency Linear Arrays. *IEEE Trans. Ultrason., Ferroelect., Freq. Contr.* **53**, 1719–1729 (2006).

112. Nguyen-Dinh, A. *et al.* High Frequency Piezo-Composite Transducer Array Designed for Ultrasound Scanning Applications. *IEEE*, 943–947 (1996).
113. Walls, G. L. The Vertebrate Eye and Its Adaptive Radiation. *The Journal of Nervous and Mental Disease* **100**, 332 (1944).
114. Fernald, R. D. *Sensory Biology of Aquatic Animals* 435–466 (Springer New York, 1988). doi:10.1007/978-1-4612-3714-3_18
115. Reusz, G., Sarkany, P., Gal, J. & Csomos, A. Needle-Related Ultrasound Artifacts and Their Importance in Anaesthetic Practice. *British Journal of Anaesthesia* **112**, 794–802 (2014).
116. Barthez, P. Y., Leveille, R. & Scrivani, P. V. Side Lobes and Grating Lobes Artifacts in Ultrasound Imaging. *Veterinary Radiology & Ultrasound* **38**, 387–393 (1997).
117. Jeong, M. K. & Kwon, S. J. Side Lobe Free Medical Ultrasonic Imaging with Application to Assessing Side Lobe Suppression Filter. *Biomedical Engineering Letters* **8**, 355–364 (2018).
118. Szabo, T. L. *Diagnostic Ultrasound Imaging: Inside Out*. (Academic Press, 2013). doi:10.1016/B978-0-12-396487-8.00006-9
119. Fei, C. *et al.* Design of Matching Layers for High-Frequency Ultrasonic Transducers. *Appl. Phys. Lett.* **107**, 123505 (2015).
120. Shen, Z. *et al.* An Improved Equivalent Circuit Simulation of High Frequency Ultrasound Transducer. *frontiersin.org* (2021).
121. Guess, J. F., Oakley, C. G., Douglas, S. J. & Morgan, R. D. Cross-Talk Paths in Array Transducers. *IEEE*, 1279–1282 (1995).
122. Huang, H., Paramo, D. & Deshmukh, S. Unpowered Wireless Transmission of Ultrasound Signals. *Smart Mater. Struct.* **20**, 015017 (2010).
123. Haataja, L., Mercuri, E., Cowan, F. & Dubowitz, L. Cranial Ultrasound Abnormalities in Full Term Infants in a Postnatal Ward: Outcome at 12 and 18 Months. *Archives of Disease in Childhood - Fetal and Neonatal Edition* **82**, 128–133 (2000).
124. Cranial or Head Ultrasound.
125. Becker, G. & Berg, D. Neuroimaging in Basal Ganglia Disorders: Perspectives for Transcranial Ultrasound. *Movement Disorders* **16**, 23–32 (2001).
126. Forbes, T. P., Degertekin, F. L. & Fedorov, A. G. Multiplexed operation of a micromachined ultrasonic droplet ejector array. *Rev. Sci. Instrum.* **78**, 4101 (2007).
127. Kwok, K. W., Hon, S. F. & Lin, D. Lead-Free Self-Focused Piezoelectric Transducers for Viscous Liquid Ejection. *Sensors & Actuators: A. Physical* **168**, 168–171 (2011).
128. Huang, D. & Kim, E. S. Micromachined Acoustic-Wave Liquid Ejector. *Journal of Microelectromechanical Systems* **10**, 442–449 (2001).
129. Hon, S. F., Kwok, K. W., Li, H. L. & Ng, H. Y. Self-Focused Acoustic Ejectors for Viscous Liquids. *Rev. Sci. Instrum.* **81**, 5102 (2010).

130. Kim, M., Kim, J. & Cao, W. Electromechanical coupling coefficient of an ultrasonic array element. *J. Appl. Phys.* **99**, 074102–6 (2006).
131. Ketterling, J. A., Aristizabal, O., Turnbull, D. H. & Lizzi, F. L. Design and Fabrication of a 40-MHz Annular Array Transducer. *IEEE Trans. Ultrason., Ferroelect., Freq. Contr.* **52**, 672–681 (2005).

APPENDIX

APPENDIX 1. ACOUSTIC ATTENUATION IN MULTIPLE MEDIUMS

MATERIAL	ATTENUATION α $\left(\frac{dB}{MHz \cdot cm}\right)$
Air, at 20 °C	1.64
Blood	0.2
Bone, cortical	6.9
Bone, trabecular	9.94
Brain	0.6
Breast	0.75
Cardiac	0.52
Connective tissue	1.57
Dentin	80
Enamel	120
Fat	0.48
Liver	0.5
Marrow	0.5
Muscle	1.09
Tendon	4.7
Soft tissue (average)	0.54
Water	0.0022

APPENDIX 2 ACOUSTIC IMPEDANCE OF HUMAN ORGANS AND TISSUES.

Body Tissue	Acoustic Impedance (MRayl)
Air	0.0004
Lung	0.18
Fat	1.34
Liver	1.65
Blood	1.65
Kidney	1.63
Muscle	1.71
Bone	7.80

APPENDIX 3 PIEZOELECTRIC PROPERTIES OF PMN-0.28PT BULK MATERIAL

Material	PMN-0.28PT
Longitudinal velocity v_z (ms^{-1})	4038
Density ρ (kgm^{-3})	7920
Clamped dielectric constant ϵ_{33}^s	621.6
Piezoelectric constant d_{33} (pC/N)	1400
Electromechanical coupling coefficient k_t	0.58
Acoustic impedance Z (MRayl)	32
Thickness (μm)	500

APPENDIX 4 PIEZOELECTRIC PROPERTIES OF PZT BULK MATERIAL

Material	PZT PIC151
Longitudinal velocity v_z (ms^{-1})	4967
Density ρ (kgm^{-3})	7816
Clamped dielectric constant ϵ_{33}^s	2153
Piezoelectric constant d_{33} (pC/N)	526
Electromechanical coupling coefficient k_t	0.57
Acoustic impedance Z (MRayl)	38.82
Thickness (μm)	500

APPENDIX 5. THE PARAMETERS AND PROPERTIES OF THE INVESTIGATED MATCHING LAYERS

Centrifuge method

<i>Component</i>	<i>Ratio</i>	<i>Rotational Speed (rpm)</i>	<i>Time (min)</i>	<i>Acoustic velocity (m/s)</i>	<i>Density (g/cm³)</i>	<i>Impedance (MRayl)</i>
<i>Epoxy 502</i>	N/A	N/A	N/A	2679.60	1180.00	3.16
<i>Ag powder + Epoxy 502</i>	2.4/1	3000	15	1823.60	3386.18	6.18
<i>Ag powder + Epoxy 502</i>	2.4/1	3000	15	1875.38	3316.51	6.22
<i>Ag powder + Epoxy 502</i>	2.8/1	3000	15	1792.16	3721.32	6.67
<i>Ag powder + Epoxy 502</i>	3.0/1	3000	15	1859.07	3540.79	6.58
<i>Al₂O₃(1-2μm) powder+ Epoxy 502</i>	1.5/1	3000	10	2989.55	2003.83	5.99
<i>Al₂O₃(1-2μm) powder+ Epoxy 502</i>	1.3/1	3000	10	3085.74	2002.21	6.18

Compression method

<i>Component</i>	<i>Ratio</i>	<i>Compression Pressure (MPa)</i>	<i>Acoustic velocity (m/s)</i>	<i>Density (g/cm³)</i>	<i>Impedance (MRayl)</i>
<i>α phase Al₂O₃ powder + Epoxy 502</i>	3.0/1	7.8	2728.32	2512.74	6.86
<i>Al₂O₃(1-2μm) powder + Epoxy 502</i>	2.0/1	31.2	3244.90	2274.15	7.38
<i>SiC powder + Epoxy 502</i>	10.0/1	85.8	2568.00	2199.00	5.65

APPENDIX 6 THE PARAMETER AND PROPERTIES OF THE INVESTIGATED BACKING LAYERS

<i>Component</i>	<i>Ratio</i>	<i>Rotational Speed (rpm)</i>	<i>Time (min)</i>	<i>Acoustic velocity (m/s)</i>	<i>Density (g/cm³)</i>	<i>Impedance (MRayl)</i>
<i>Al₂O₃(1-2μm) powder+ Epo-Tek301+W(100) powder+glass cell(C15 3M)</i>	1:1:1:0.1	N/A	N/A	2189.18	3218.25253	7.05
<i>Al₂O₃(1-2μm) powder+ Epo-Tek301+W(50) powder+ glass cell(C15 3M)</i>	1:1:1.5:0	N/A	N/A	2365.39	2800.56056	6.62
<i>Al₂O₃(1-2μm) powder+ Epo-Tek301+W(50) powder+ glass cell(C15 3M)</i>	1:1:2:0	N/A	N/A	2254.13	3035.30754	6.84
<i>Al₂O₃(1-2μm) powder+ Epo-Tek301+W(100) powder+glass cell(C15)</i>	0.5:0.7:1:0.1	N/A	N/A	2297.90	1691.18699	3.89
<i>Al₂O₃ (200~300 mesh) + Epo-Tek301 +W(25μm) powder</i>	1:1:4	500	3	2025.56	4424.2	8.96
<i>Al₂O₃ (200~300 mesh) + Epo-Tek301 +W(25μm) powder</i>	1:1:4	1500	3	1899.85	4790.22	9.10